CFD Simulation of a Large Floating Offshore Wind Turbine (FOWT)

Hydrodynamic and Aerodynamic Analysis of the IEA 15MW Wind Turbine Mounted on the VolturnUS-S Floating Platform using OpenFOAM

Master thesis SET

Mathis Miroux

Delft University of Technology

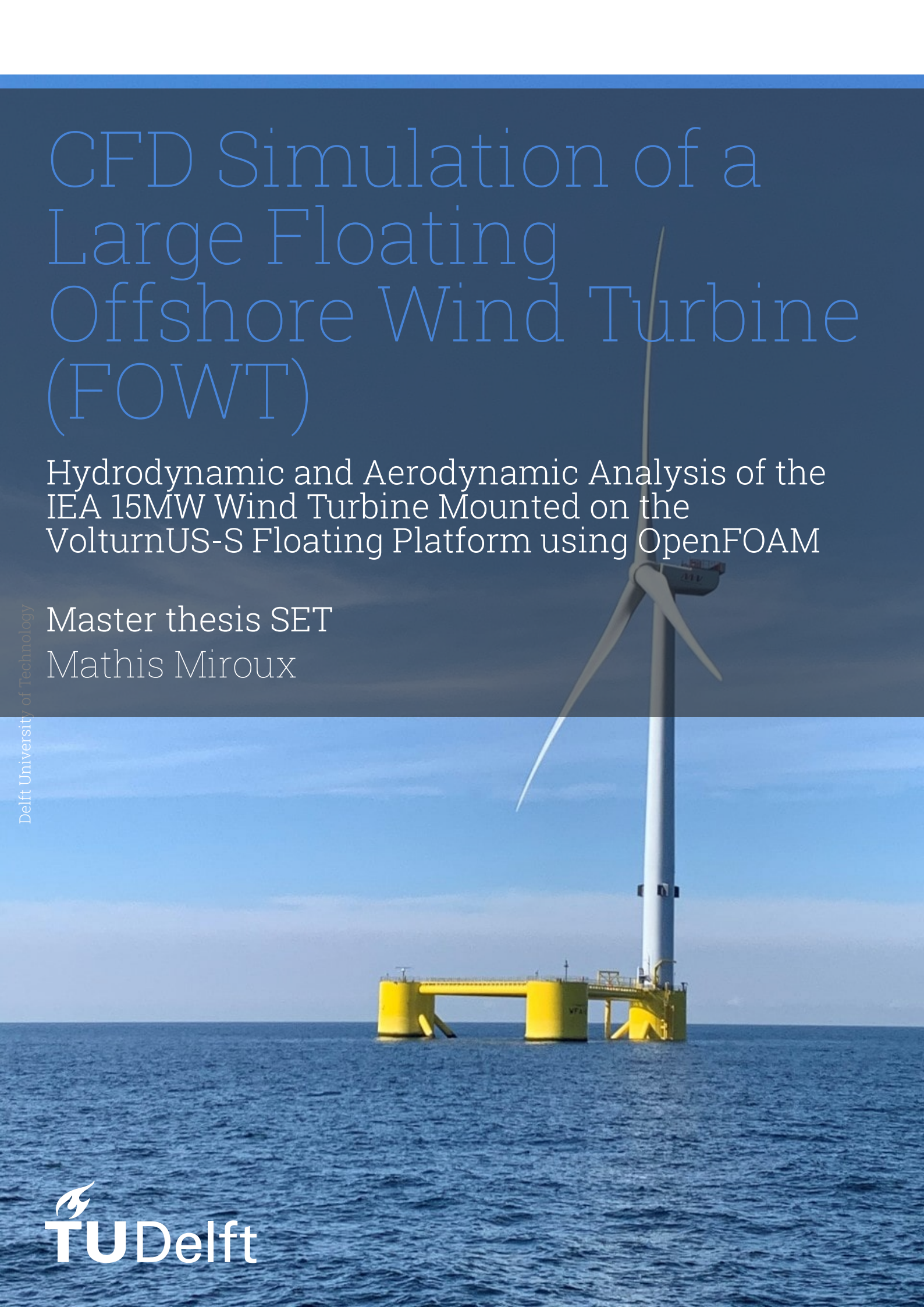

TU Delft

CFD Simulation of a Large Floating Offshore Wind Turbine (FOWT)

Hydrodynamic and Aerodynamic Analysis of the IEA 15MW Wind Turbine Mounted on the VolturnUS-S Floating Platform using OpenFOAM

by

Mathis Miroux

Student Name	Student Number
Mathis Miroux	5852110

Main co-supervisor:	Prof.dr.ir. A.C. Viré
Main co-supervisor:	Dr.ir. D.A.M. (Delphine) De Tavernier
External committee member:	Dr.ir. A.H. (Alexander) van Zuijlen
Project Duration:	01, 2024 - 10, 2024
Faculty:	Faculty of Aerospace Engineering, Delft

TU Delft

Acknowledgments

First and foremost, I want to sincerely thank my supervisors, Axelle Viré and Delphine De Tavernier, for their constant support, guidance, and feedback throughout this project. You were always there when I needed help, and I'm really grateful for the chance to learn from you.

I also want to thank the third member of my thesis committee, Alexander van Zuijlen, for taking the time to review my work.

A big thanks to the Wind Energy research group, especially Ricardo and Likhitha, who were a huge help in understanding and troubleshooting parts of my work. I'm also really thankful to the Flow Physics Department for letting me access the HPC and run countless simulations.

On a personal note, I'd like to thank my family and friends for all their support during this journey—from France to the Netherlands. To my family, thank you for your encouragement and advice and for always being there for me. To my friends, thank you for making my time in the Netherlands more fun than I imagined—hiking, playing volleyball, and enjoying life together really helped me find balance. Those countless fun evenings and study sessions on the 3rd floor made everything so much better.

Mathis Miroux
Delft, October 2024

Abstract

This thesis presents a comprehensive study on Floating Offshore Wind Turbine's (FOWT's) modeling and simulation, focusing on the IEA 15MW wind turbine coupled to the VolturnUS-S semi-submersible platform. The primary goal was to develop the building blocks of a high-fidelity Computational Fluid Dynamics (CFD) coupled model using OpenFOAM to simulate large-scale FOWT behavior, verify, and compare each component individually against the mid-fidelity tool OpenFAST. The project builds on the frameworks of previous studies by Pere Frontera Pericàs [81] and Scarlatti [98], expanding them to accommodate the complexities of a larger turbine and more intricate environmental conditions.

The model was implemented using OpenFOAM's `waves2Foam` and `Moody` libraries for wave and mooring modeling, respectively, while aerodynamic simulations employed the `turbinesFoam` package with an actuator line approach. A spatial convergence study optimized mesh parameters for computational efficiency and accuracy, ensuring reliable and stable simulation results for motions up to 24 meters in surge. Comparisons between OpenFOAM and OpenFAST using a P-Q analysis highlighted significant differences, particularly in modeling damping. OpenFAST was shown to underestimate both linear and quadratic hydrodynamic damping due to its simplified representation of fluid dynamics. Discrepancies in the equilibrium positions were found between the decay tests using CFD; their origin still needs more investigation.

In aerodynamic simulations, steady-state and prescribed motion tests revealed critical differences in thrust and power predictions between OpenFOAM and OpenFAST. OpenFAST overpredicted the reduction in axial wind speed, leading to a reduced power output for steady turbine simulations. The CFD model provided a more accurate representation of rotor wake effects and dynamic responses, particularly in high-frequency surge conditions, where OpenFAST overestimated power fluctuations. These findings underscore the importance of using high-fidelity models like OpenFOAM to improve the accuracy of performance predictions in floating wind turbines.

The study concludes by offering recommendations for future research, including model validation using experimental data and the implementation of overset mesh techniques to improve simulation stability for large motions. The work establishes a reliable CFD framework for simulating this large FOWT, offering insights into enhancing mid-fidelity models and guiding future developments in floating wind turbine design and analysis. It also builds a fully coupled CFD model in OpenFOAM to investigate its behavior.

Contents

Acknowledgments i

Abstract ii

1 Introduction 1
- 1.1 General context: Floating offshore wind energy in the sustainable transition . . . 1
  - 1.1.1 Why is the energy transition needed ? . . . 1
  - 1.1.2 Global numbers on wind energy . . . 4
- 1.2 Challenges of Floating Offshore Wind Turbines . . . 7
  - 1.2.1 General challenges . . . 7
  - 1.2.2 Design challenges: the need for Computational Fluid Dynamics (CFD) . . . 8
- 1.3 Research motivation . . . 9
- 1.4 Research objective and research questions . . . 10
- 1.5 Thesis outline . . . 10

2 Background theory 12
- 2.1 Analytical theory . . . 12
  - 2.1.1 Hydrodynamics of FOWT . . . 12
  - 2.1.2 Mooring dynamics for FOWT . . . 17
  - 2.1.3 Aerodynamics of FOWTs . . . 19
  - 2.1.4 Coupled CFD simulations . . . 22
- 2.2 Numerical theory: case of OpenFOAM . . . 24
  - 2.2.1 Basics of CFD . . . 24
  - 2.2.2 Finite volume method . . . 25
  - 2.2.3 Multiphase flow: the Volume of Fluid (VoF) method . . . 25
  - 2.2.4 Pressure-velocity coupling algorithms . . . 26
  - 2.2.5 Modelling of moving bodies in OpenFOAM: Dynamic mesh methods . . . 26
  - 2.2.6 Numerical wave tank : waves2Foam . . . 27
  - 2.2.7 Turbine dynamics: TurbinesFoam . . . 27
  - 2.2.8 Rigid body dynamics: the sixDoFrigidbody solver . . . 28

3 Hydrodynamic verification of the VolturnUS-S floater 30
- 3.1 Description of the VolturnUS-S floater . . . 30
  - 3.1.1 General characteristics of the floater and its hydrodynamic modeling . . . 30
  - 3.1.2 Mooring system properties . . . 32
- 3.2 Definition of a verification study and methodology . . . 32
  - 3.2.1 Definition of a verification study in the context of FOWTs . . . 33
  - 3.2.2 Description of the methodology . . . 33
- 3.3 Numerical setup . . . 36
  - 3.3.1 Characteristics of the simulation domain . . . 36
  - 3.3.2 Numerical mooring setup . . . 36
  - 3.3.3 Refinement around the floater . . . 37
  - 3.3.4 Use of the dynamic mesh morphing technique . . . 37
  - 3.3.5 Six-DoF rigid body . . . 38
  - 3.3.6 Choice of the numerical timestep . . . 39
- 3.4 Verification study: grid convergence . . . 39
  - 3.4.1 Part 0: Equilibrium position of the floater . . . 40
  - 3.4.2 Part 1: Refinement of the cylinders . . . 40
  - 3.4.3 Part 2: Size of the cylinders . . . 44
  - 3.4.4 Bonus Part: Time optimization running on HPC12 . . . 47

3.5 OpenFAST modelling . . . 49
3.6 Results: Comparison with OpenFAST . . . 50
3.6.1 Surge decay tests . . . 50
3.6.2 Heave decay tests . . . 55
3.6.3 Pitch decay tests . . . 58
3.7 Outlooks for further validation studies . . . 60
3.8 Key findings . . . 64

4 Aerodynamic verification of the 15MW wind turbine 65
4.1 Litterature review . . . 65
4.1.1 Differences between fixed wind turbines and FOWT . . . 65
4.1.2 Experimental campaigns and validation campaigns . . . 66
4.2 IEA 15MW reference wind turbine . . . 68
4.3 Numerical setup for steady conditions . . . 70
4.3.1 Assumptions . . . 70
4.3.2 Turbulence modelling . . . 71
4.3.3 Domain . . . 71
4.3.4 ALM modelling . . . 71
4.3.5 On the inclusion of hub and tip loss factors . . . 72
4.3.6 Temporal discretisation . . . 72
4.3.7 Boundary conditions . . . 72
4.3.8 Solver settings . . . 73
4.3.9 OpenFAST modelling . . . 73
4.4 Results . . . 74
4.4.1 Method of analysis . . . 74
4.4.2 Steady inflow . . . 74
4.4.3 Prescribed motions . . . 77
4.5 Conclusions and recommendations . . . 80

5 Conclusion 82
5.1 Thesis summary . . . 82
5.2 Answer to the research questions . . . 83
5.3 Recommendations for Future Work . . . 84

References 86

List of Figures

1.1 Total net anthropogenic GHG emissions, 1990–2022 [110] . . . 1
1.2 Global energy flows within the 2019 global energy system, taken from IPCC WG3 [49] . 2
1.3 Global energy consumption and electricity production [48] . . . 3
1.4 New offshore wind installations completed in 2023, showing a significant increase in global capacity expansion [36] . . . 5
1.5 Expected global new floating wind installations in MW according to Global Wind Energy Council (GWEC) [36] . . . 7

2.1 Force diagram of a generic floating wind turbine [81] . . . 13
2.2 Stability Triangle: The three corners of the triangle represent the three stabilization mechanisms utilized by floating wind turbine systems [64] (a); Resulting floating structure designs for FOWT [43] (b). . . . 14
2.3 Comparison of deepwater and shallow water waves for the linear wave theory [18] . . . 16
2.4 Changes in the wave profile with higher orders of Stokes wave theory [18] . . . 16
2.5 Breaking wave height and regions of validity of various gravity water wave theories [18], inline with DNV recommendations [24] . . . 17
2.6 Diagram of the coupling of the fluid and rigid body solvers, taken from Pere Frontera Pericàs [81] . . . 29

3.1 General arrangement of the VolturnUS-S floater developed by the University of Maine [1] 31
3.2 Heave position of the center of rotation of the VolturnUS-S floater with the mass of the IEA 15MW wind turbine on top, the center of rotation and the center of gravity coincide. 38
3.3 Heave position of the Center of Rotation of the VolturnUS-S floater without the mass of the IEA 15MW wind turbine on top . . . 38
3.4 Surge decay tests with varying acceleration relaxation parameter using a coarse mesh . 39
3.5 Surge decay tests for the first refinement study, where the grid is progressively refined . 41
3.6 Time dependent variables, for adaptative timesteps with maxDt = 0.05 and maxCo = 0.5 for a coarse (a), medium (b), fine (c) and extra fine mesh (d). . . . 42
3.7 Convergence of the linear damping coefficient, quadratic damping coefficient and equivalent damping ratio in surge with different grid refinements in a, b and c respectively. The dots are the CFD solutions computed for four different refinement ratios as detailed in Table 3.8. The estimated discretization uncertainties are depicted as symmetric uncertainty bands attached to the dots . . . 43
3.8 Comparison of 30m-surge decay tests for coarse and medium-coarse mesh in a and b respectively. Unstable results are found. . . . 45
3.9 Comparison of 30m-surge decay tests for medium and fine mesh as shown in a and b respectively. The results are stable. . . . 45
3.11 Difference in surge motions between the extra fine mesh and the fine/medium meshes in the second refinement study . . . 46
3.12 Courant numbers for the fine mesh, 15m Surge decay test . . . 46
3.10 Surge decay test for the second refinement study, where the size of the refinement zone of the floater is varied . . . 47
3.13 Sensitivity analysis of the mesh refinement zone around the floater for a surge decay test with a 24m offset . . . 48
3.14 Mean amplitudes vs. normalized amplitude decrease (P-Q analysis), for surge movements, over half cycles without optimization . . . 50
3.15 P-Q analysis on surge movements, over full cycles, without optimization . . . 52
3.16 P-Q analysis on surge movements, using linear optimization to get the equilibrium positions 53

3.17 Comparison of surge position during surge decay tests between OpenFAST and OpenFOAM . . . 55
3.18 Comparison of two P-Q analyses for heave decay tests: without optimization (a) and with linear optimization (b) . . . 56
3.19 Comparison of heave position during heave decay tests between OpenFAST and OpenFOAM . . . 56
3.20 P-Q analysis for pitch movements (a) and pitch amplitudes for the decay test (b) . . . 58
3.21 Froude-Reynolds scaling conflict as illustrated in [5], demonstrating the incompatibility of satisfying both Froude and Reynolds scaling simultaneously . . . 61

4.1 The four working states of floating wind turbines from [25] . . . 66
4.2 Convergence for a wind turbine operating at a steady wind speed of 10.59 m/s and 5% turbulence intensity in OpenFOAM, with a time averaging over 1 second (a) and 10 seconds (b) respectively . . . 75
4.3 Comparison of power and thrust coefficients of the IEA 15MW wind turbine in a steady state with a 10.59 m/s uniform wind in (b) (a) respectively in OpenFOAM and OpenFAST. 75
4.4 Comparison of turbine thrust in steady-state conditions with 10.59 m/s uniform wind between OpenFOAM and OpenFAST . . . 76
4.5 Comparison of the thrust (a) and tangential force (b) per unit length of a single blade in steady-state conditions with 10.59 m/s uniform wind between OpenFOAM and OpenFAST 76
4.6 Comparison of angle of attack and axial velocity for the same case study as above, in steady-state conditions with 10.59 m/s uniform wind between OpenFOAM and OpenFAST 77
4.7 Thrust comparisons during prescribed motion: (a) shows the average thrust over four cycles, while (b) presents a comparison of thrust values from simulations taken from [83]. 78
4.8 Comparison of Max/Min Values and Coefficients for Prescribed Motion with frequencies of 0.01419, 0.02441, 0.05676 Hz as shown in a,b, and c, respectively . . . 78
4.9 Comparison of the angle of attacks for a prescribed motion at a frequency of $0.0149Hz$. On the left, the amplitudes are compared to the phase of motion, and on the right, the min/max values of the angle of attack are shown. . . . 80
4.10 Comparison of the angle of attack for prescribed motion at a frequency of $0.02441Hz$. On the left, the amplitudes are compared to the phase of motion, and on the right, the min/max values of the angle of attack are shown. . . . 80
4.11 Comparison of the angle of attack for prescribed motion at a frequency of $0.05676Hz$. On the left, the amplitudes are compared to the phase of motion, and on the right, the min/max values of the angle of attack are shown. . . . 80

List of Tables

1.1 Tools used in engineering for FOWT modeling, taken from Otter et al. [76] 8

2.1 Distinction between deep and shallow water waves and their respective dispersion relations. 15
2.2 Summary of different dynamic models and their applications. 18

3.1 General System Properties of the IEA 15MW Turbine Mounted on the VolturnUS-S Platform 32
3.2 VolturnUS-S Semisubmersible Platform Properties 32
3.3 Mooring System Properties 32
3.4 Mooring Line Drag and Added Mass Coefficients 32
3.5 Boundary conditions for the volume fraction, modified pressure, and velocity. 37
3.6 Boundary conditions for dynamic meshes 37
3.7 Equilibrium position of the floater without the tower mass 40
3.8 Parameters for the first part of the mesh convergence study 40
3.9 Results of the P-Q analysis for the first refinement study 42
3.10 Results of the amplitude analysis for the first refinement study 43
3.11 Discretization uncertainty of key damping parameters 43
3.12 Equilibrium position of the floater with the tower mass and sway mistake 44
3.13 Dimensions for different refinement levels 45
3.14 Results of the P-Q analysis for the second refinement study, 15m surge decay test . . . 46
3.15 Results of the amplitude for the second refinement study, 15m surge decay test 46
3.16 P-Q analysis results for the sensitivity test on the 24m offset surge decay test 47
3.17 Amplitude analysis results for the sensitivity test on the 24m offset surge decay test . . 47
3.18 Comparison of configurations with type J and type M nodes 48
3.19 Sensitivity study on the number of nodes used to perform a 5m heave decay test 49
3.20 Equilibrium position of the floater for OpenFAST/OpenFOAM study 50
3.21 Results of the P-Q analysis by identifying varying surge equilibrium positions in OpenFOAM, using different optimization methods 51
3.22 Best fit comparison for surge decay tests performing a P-Q analysis, with equilibrium position based on the equilibrium simulations 52
3.23 Comparison of OpenFOAM and OpenFAST Simulation Results for surge movements observed during surge decay tests 54
3.24 Optimization of the offset position for the heave decay tests 56
3.25 Comparison of heave motion parameters between OpenFOAM and OpenFAST 57
3.26 Comparison of pitch motion parameters between OpenFOAM and OpenFAST 58

4.1 Key Parameters for the reference IEA Wind 15-MW Turbine with bottom fixed tower [1] 69
4.2 Blade Properties of the IEA 15MW wind turbine [1] 70
4.3 Summary of boundary conditions for each field. 72
4.4 Influence of turbulence modeling in OpenFOAM 74
4.5 Comparison between OpenFAST and OpenFOAM for steady and uniform wind simulations 77

1

Introduction

1.1. General context: Floating offshore wind energy in the sustainable transition

1.1.1. Why is the energy transition needed ?

Global warming, driven predominantly by human activities such as burning fossil fuels and deforestation, continues to pose an escalating threat to our planet's climate system. With greenhouse gas emissions reaching historic highs in 2023, as shown in Figure 1.1, the Earth's average temperature steadily rises, leading to far-reaching impacts. From more frequent and intense heatwaves, storms, and wildfires to rising sea levels, melting ice caps, and disrupted ecosystems, the consequences of global warming are increasingly evident worldwide as extensively described in the latest IPCC AR6 report [49].

The rise in global energy consumption has been closely linked to the increased usage of fossil fuels, primarily coal, oil, and natural gas. As populations grow, economies expand, and industrialization accelerates, the energy demand escalates correspondingly. Fossil fuels have historically been the cornerstone of meeting this demand due to their abundance, energy density, and established infrastructure. However, their combustion releases greenhouse gases such as carbon dioxide (CO2) into the atmosphere, contributing significantly to global warming and climate change as shown in Figure 1.1.

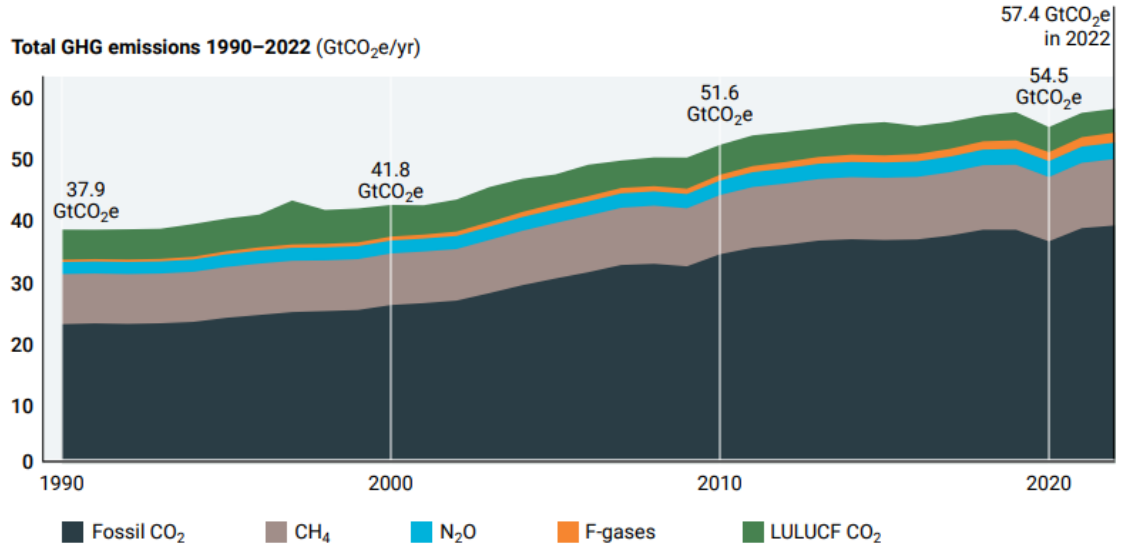

Figure 1.1: Total net anthropogenic GHG emissions, 1990–2022 [110]

Energy plays a particular role: it is the lifeblood of our economy, as shown in Figure 1.2. Every sector needs energy to function. To show that, we differentiate different types of energy. Primary energy refers to raw energy extracted from the environment, like crude oil from a well. This crude oil must be processed and refined into secondary energy, such as gasoline, which is then transported to gas stations for consumers, termed as final energy. The ultimate goal is useful energy, where gasoline is used to power a car, converting its chemical energy into mechanical energy for movement. However, this conversion involves significant losses, with real-world car engines operating at about 25% efficiency, meaning only a quarter of the final energy is converted into useful energy for propulsion.

Total final energy consumption (TFC) is 448 EJ today and is split between industry (162 EJ), buildings (120 EJ), transport (116 EJ), and other end-uses (45 EJ). Nowadays, 80 % of the total energy supply is covered by fossil fuels [48], which, as shown in Figure 1.1 are the main driver in rising CO_2 emissions, thus in accelerating climate change. One of the environmental transition challenges is switching from a fossil fuel-based industrial economy to a sustainable society that stays within planetary boundaries. Figure 1.2 shows which primary sources are used for which consumption sectors in 2019, showing how much energy is lost. Although the renewable energy share has improved in the final energy consumption since 2019, the trends are still similar, and the fossil primary energy supply and final energy consumption are still on the rise.

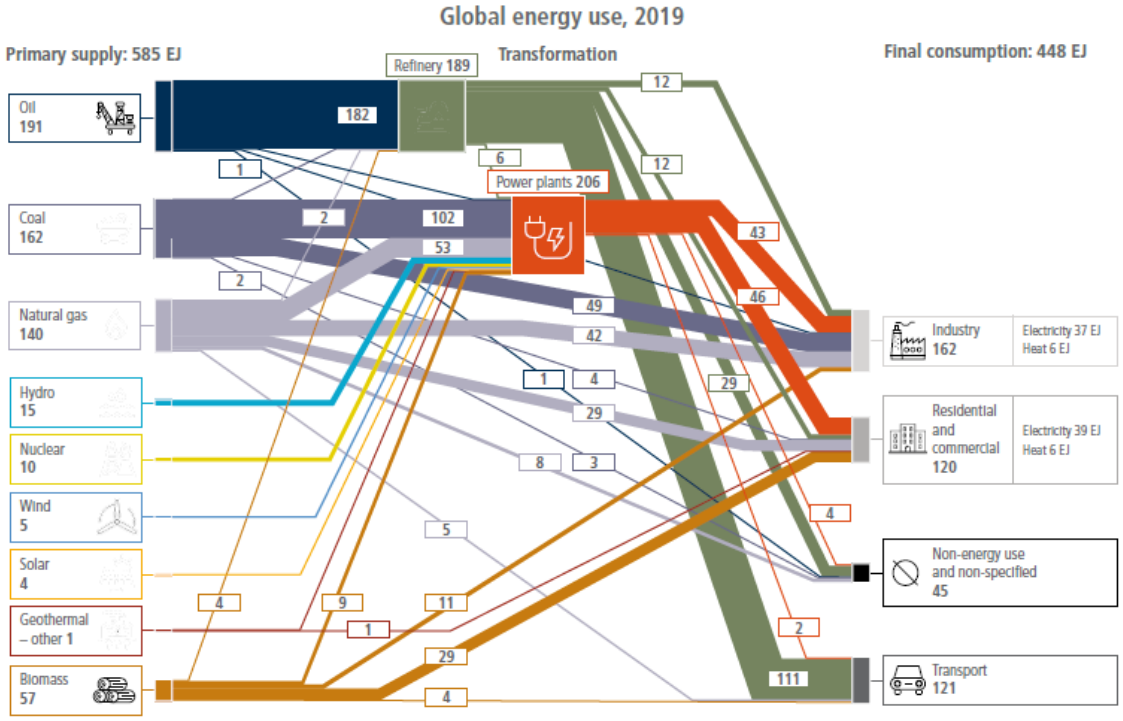

Figure 1.2: Global energy flows within the 2019 global energy system, taken from IPCC WG3 [49]

Energy should be sustainable, affordable, and resilient to changes: this is known as the energy trilemma, one framework that can be used to describe the energy transition challenge [65]. The energy trilemma encapsulates the challenge of balancing three crucial aspects in the global energy landscape: sustainability, energy equity, and security. Sustainability demands adopting renewable and clean energy sources to mitigate environmental degradation and combat climate change. Affordability emphasizes providing energy at reasonable costs, ensuring accessibility for all socioeconomic groups. Security underscores the need for reliable and resilient energy systems, safeguarding against disruptions and geopolitical tensions. Achieving equilibrium among these three dimensions is intricate, as actions taken to address one aspect often have repercussions on the others.

Renewable energy sources are considered one of the most critical solutions to solve this energy trilemma in the power sector, which then powers the transport, residential, and industrial sectors. For

example, in 2050, Figure 1.2 could differ by shifting the energy flow from the refinery to power the transportation sector to power plants powering the new electric mobility. Similarly, some industrial processes, such as the steel sector, rely on electricity instead of coal. For power systems, renewable energies are more sustainable than fossil fuel-based energies, more resilient to geopolitical changes when installed, and more competitive than some fossil fuel-based systems [48]. Electricity plays a central role in modern economies, representing approximately 20% of total final energy consumption at present and is expected to grow to 50% in the most ambitious scenario of the IEA [48], and renewables are expected to make out of more than 75% of the final electricity as shown in Figure 1.3a.

The latest annual review of global electricity data by Ember [118] suggests that there's a notable shift happening: fossil fuel electricity generation, along with its emissions, is expected to peak in 2024 as renewable energy sources continue to increase. In 2023, renewables supplied a record-breaking 30% of global electricity demand. However, emissions from the sector would have already peaked if not for a significant decrease in hydropower generation. The rise of wind and solar energy has played a crucial role in curbing the growth of fossil fuel power. Without these renewables, Ember estimates that fossil fuel generation would have been 22% higher in 2023, resulting in an additional 4 billion tonnes of carbon dioxide emissions annually [118]. Despite this progress, there's a pressing need to accelerate the growth of clean energy sources to meet the global objective of tripling renewables by 2030. Achieving this target could nearly halve power sector emissions by the decade's end, aligning with the 1.5°C climate target outlined in the Paris Agreement.

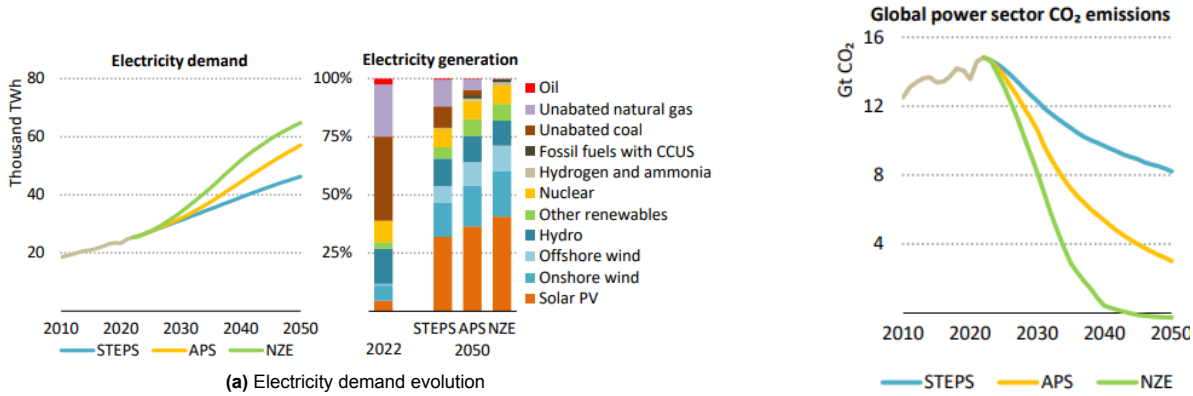

(a) Electricity demand evolution

(b) power sector emissions

Figure 1.3: Global energy consumption and electricity production [48]

While discussing this, it is crucial to recognize that achieving a one-to-one replacement of fossil fuels with renewable energy sources may not be the right approach. The expansion of renewable energy also brings environmental consequences, including land use and mineral resource consumption. Therefore, it's essential to be cautious during the development of renewable energy infrastructure to ensure it doesn't exacerbate overconsumption and only meets critical needs. Instead, the focus should be on ensuring that renewable energy projects are necessary and aligned with energy-sufficiency goals. This concept has been highlighted for the first time in the latest IPCC report [19].

Energy sufficiency rests on four pillars. These encompass public policies and everyday practices—the latter being influenced by the former—that preemptively reduce demand for natural resources, ensure the well-being of all, provide a decent life for everyone, and operate within the confines of planetary boundaries, not just carbon budgets. For instance, for mobility, energy-sufficiency-focused policies would prioritize public transportation to ensure physically and financially accessible mobility for all rather than constructing more highways that would lead to more resource use and pressure on land and water.

In conclusion, the pressing need for increased electricity supply and the imperative to reduce carbon emissions underscores the critical role of renewable energy sources in shaping our energy landscape. As detailed in the previous sections, global power sector emissions reached historic highs in 2023, highlighting the urgency to transition to cleaner energy sources. While fossil fuels have historically dominated energy production, the remarkable growth of renewables like wind and solar offers a promising

pathway to mitigate emissions and meet increasing electricity demand. Furthermore, integrating principles of energy sufficiency into our transition to renewable energy sources ensures that our efforts are environmentally sustainable, socially equitable, and economically viable. The subsequent section will delve into the specifics of wind power, illustrating its potential to contribute significantly to our renewable energy future.

1.1.2. Global numbers on wind energy

In 2023, a historic milestone was reached: 200 governments agreed at COP28 on triple renewable energy capacity annually globally and double energy efficiency improvements by 2030 to get on track for a pathway that limits global warming to 1.5°C. Wind energy was recognized as one of the critical technologies to mitigate climate change as it has become cost-effective and available. As seen in Figure 1.4, a record-breaking 115 GW of new wind power was installed globally in 2023, representing a 50% increase over the prior year, demonstrating the industry's resilience despite supply chain issues and macroeconomic challenges such as rising inflation and interest rates and geopolitical disruptions. However, some challenges have to be tackled for at least 320 GW annual installation of wind turbines by the end of the decade as reported by the Global Wind Energy Council (GWEC) [36] (Global Wind Energy consortium).

- Issues with permits slow down worldwide initiatives and raise their expenses
- Grids require immediate investment because they were built for a previous period. Grids are congested, and in the long term, they have to be reinforced
- Workforce and supply chain shortages will worsen if not planned enough ahead.
- As wind grows, social acceptance and land rights conflicts will get more intense.

To address these issues, common recommendations, among other things, are to have stable policy environments, build robust and resilient supply chains to derisk the industry from geopolitical disruptions, better collaboration between governments and industry to ensure supply chains, invest in grids to be able to accommodate to growing electricity demand, have more inclusive tenders to involve local communities and mitigate local headwind and foster support. It is also essential to fight against misinformation and disinformation, which leads to unpredictability at wind energy projects' policy and decision-making levels. One surprising example comes from the US. Despite the absence of scientific proof, some wind energy opponents have attributed a recent increase in whale deaths to exploratory tools that employ sonar to locate wind turbine locations [100].

About offshore wind energy

As shown in Figure 1.4, the cumulative annual growth rate (CAGR) is accelerating with the years, while the share of offshore capacity is rising. Moving farther offshore provides access to stronger wind resources, more available space, and improved public acceptance. Offshore wind plays a key role for several important reasons.

- **A crucial energy source to ensure the security of electricity supply and achieve carbon neutrality by 2050**: Transportation infrastructure imposes limits on the gigantism that onshore wind energy can achieve. The blade's size is limited due to onshore transportation constraints. Offshore wind infrastructures do not have these constraints: factories can be situated next to harbors, and wind turbine components can be directly loaded onto offshore vessels. Since the power extracted increases proportionally with the square of a wind turbine's radius, it is beneficial to build bigger turbines offshore. Since the winds are steadier offshore, offshore wind can be an important source of electricity and help meet the growing electricity needs.
- **A competitive energy source :** In economic terms, offshore wind power is one of the most competitive energy sources among new electricity production installations. Thanks to a learning and industrialization phase, fixed offshore wind costs have significantly decreased over the past decade. This trend is expected to persist for both fixed and floating offshore wind in the upcoming years, driven by ongoing technological innovations and the potential achievement of the announced volume targets.
- **An economic and industrial development opportunity:** Most European countries face slowing growth and importing clean technologies abroad. To tackle both issues, the EU has agreed on

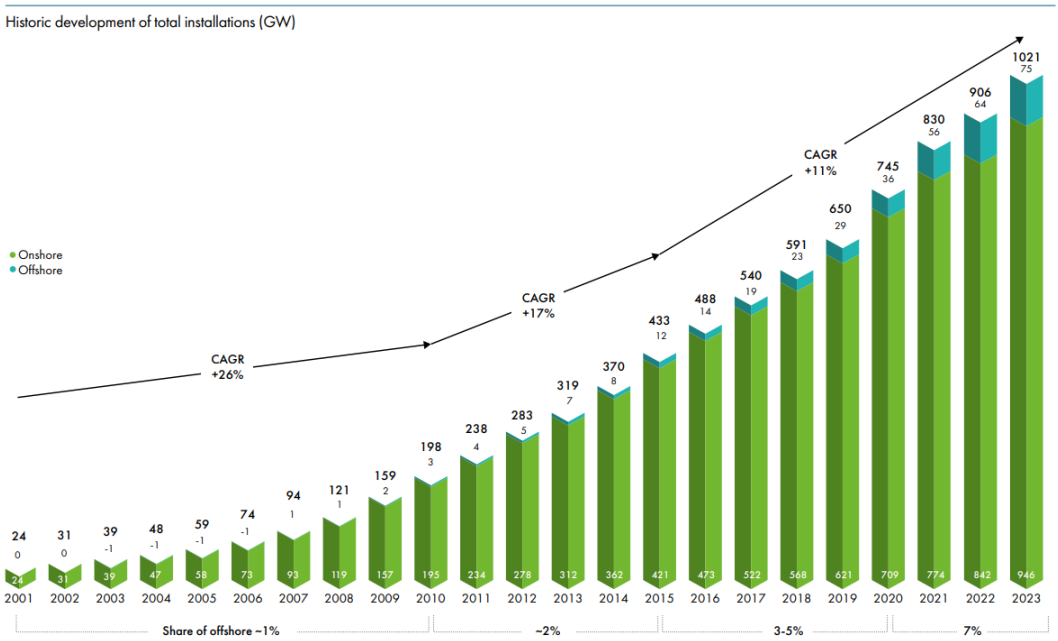

Figure 1.4: New offshore wind installations completed in 2023, showing a significant increase in global capacity expansion [36]

the Net-Zero Industry Act, which aims to scale up the manufacturing of clean technologies within the EU. Within the Green Deal industrial plan, this Act will attract investments and improve market access for cleantech in the EU, aiming to meet at least 40 % of annual net-zero technology needs by 2030. It will accelerate progress towards the EU's 2030 climate goals, advance the transition to climate neutrality by 2050, enhance industry competitiveness, create quality jobs, and support energy independence [106]. Similarly, the Inflation Reduction Act in the US has sparked a surge in new manufacturing projects of clean technologies by offering tax credits, where over $27Bn in clean energy deals have been struck [50]. In China, the 14th Five-Year Development Plan laid out an action plan to encourage the development of clean technologies and the extension of manufacturing jobs in the sector. Clean energy technologies were the top driver of China's economic growth [72]. New manufacturing companies must be built for substations, blades, nacelles, and installation vessels. Harbors have to be adapted as well to be able to handle floating wind infrastructure, for example.

- **Advancing environmental knowledge through offshore wind projects:** The implementation of these projects also enables an unprecedented acquisition of knowledge about the environment through studies that improve our understanding of the marine ecosystem and its species and anticipate the impacts of wind farms on the environment. Beyond the studies already conducted as part of the ongoing projects, broader programs are being implemented, such as the Ornit-Eof project, which aims to establish an observatory in the Mediterranean to monitor birdlife interactions with floating offshore wind farms in the Gulf of Lion[28]. Offshore wind farms also have the potential to positively impact marine environments by developing seabed habitats and restoring degraded ecosystems. In the North Sea, offshore wind farms can serve as artificial reef habitats and, for example, support the restoration of flat oyster beds [45]. Mitigation strategies can be implemented to reduce collisions with birds and bats, such as stopping the turbines during sensitive periods or making turbine blades more visible to birds. A few examples can be found in the latest report of the International Union for Conservation of Nature (IUCN) [6] or in the literature review done by France Energies Marines [62]. All actors agree that more research needs to be conducted to identify ideal mitigation methods to reduce the impact on biodiversity.
- **Co integration of offshore wind farms with other actors is possible**: France, for example, has strategically chosen to ensure the coexistence of offshore wind farms and fishing activities. This approach has involved extensive dialogue between the fishing industry and wind farm devel-

opers, leading to project adaptations such as aligning turbines with currents, widening corridors between turbines, and protecting or burying cables to facilitate fishing. Fishermen's input has been integral to project design, ensuring that their needs are addressed while developing offshore wind energy[28]. Closer to Delft, the North Sea Farm 1, launching this autumn at the Hollandse Kust Zuid wind farm near Scheveningen, will be the world's first commercial seaweed farm. This project aims to scale up seaweed production to one million tonnes annually by 2040, providing sustainable raw materials and supporting carbon sequestration efforts. The farm will also include a year-long study on the carbon capture potential of seaweed. Additionally, research will focus on the impact of seaweed farming on the marine environment and the effectiveness of models predicting seaweed distribution and carbon sequestration.

Why floating wind is necessary

Most sea areas are more profound than 70 meters, making existing commercial foundations economically unviable for deep-sea installations. Additionally, there are insufficient shallow water areas for fixed technologies to meet renewable energy targets. However, floating wind technology presents an attractive solution in countries with deep coastal waters, such as Norway, Spain, and France. Additionally, the floating offshore wind market increases the offshore wind capacity of existing markets. It can reduce the need to develop a sea bed already constrained by competition with other human use cases such as defense, fisheries, tourism, and conservation, which could increase public support. Furthermore, many deep-water areas are far offshore, with more robust wind resources than fixed offshore ones. Fixed offshore wind foundations, typically manufactured at specialist facilities worldwide, offer limited local economic benefits. In contrast, floating substructures, being larger and heavier, are challenging to transport over long distances. Therefore, they must be produced or assembled in ports near the future floating offshore wind farms. This necessity will drive significant investment and create jobs in these local ports.

With the help of industry experience from the fixed-bottom offshore wind and oil and gas sectors, floating offshore wind is quickly moving to a commercial scale. Although there have been a few floating offshore wind demonstrators operating or in construction (Hywind Scotland & Kincardine (UK); Windfloat Atlantic (Portugal); Hywind Tampen (Norway); and Goto (Japan)), the industry still faces a lot of known unknowns. In the next two years, one of the most active global floating markets will be France, with 85MW moving into the construction phase at three projects: Les Eoliennes Flottantes du Golfe du Lion (EFGL), EolMed, and the Provence Grand Large (PGL). The French government manages several lease rounds expected to deliver up to 2GW of floating offshore wind.

Over the next five years, a small number of 100-500MW wind farms are expected to be successfully built. GWEC Market Intelligence predicts that 10.9GW will likely be built by 2030, while the critical acceleration will likely occur during the 2030s, as seen in Figure 1.5.

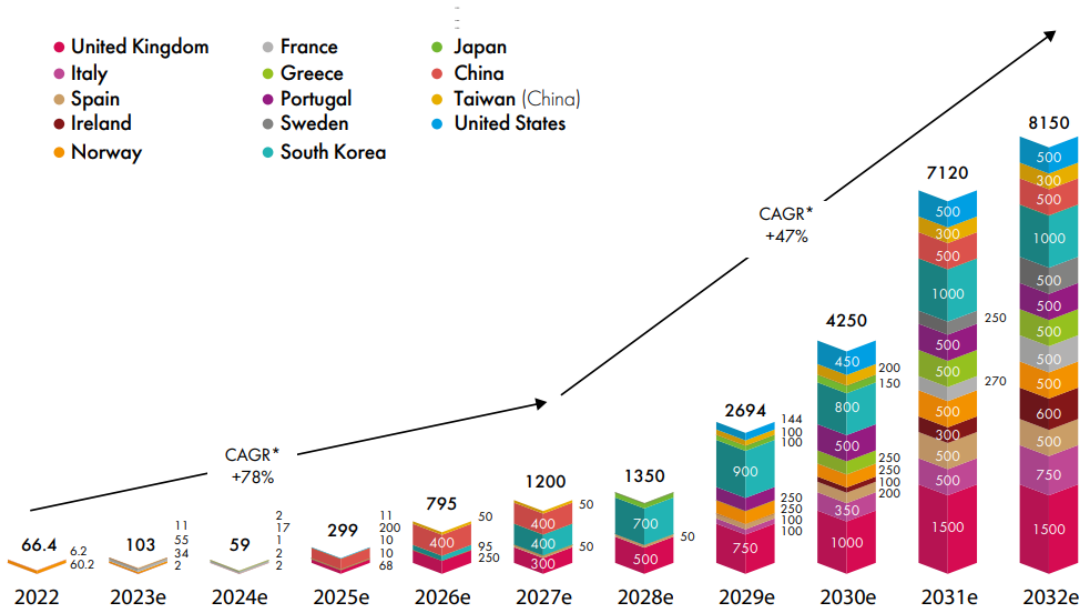

Figure 1.5: Expected global new floating wind installations in MW according to Global Wind Energy Council (GWEC) [36]

1.2. Challenges of Floating Offshore Wind Turbines

1.2.1. General challenges

However, many challenges must be met for the floating offshore wind market to become competitive and viable. This section will briefly discuss a few examples.

- **Design phase:** Compared to bottom fixed wind turbines, the FOWTs are moving: the floater has some hydrodynamic characteristics that must be coupled with the unsteady turbine loading. The 6 degrees of freedom of the FOWt implies a coupling between the aerodynamics and the hydrodynamics that has to be accounted for. One challenge is to develop accurate, fully coupled aero-hydro-elastic simulation tools for FOWTs. It is also accurate to choose the mooring line type and anchors to keep floating turbines at their location and reduce loads and fatigue for station-keeping while modeling them correctly. More details will be described in the research motivation phase.
- **Control strategies:** The control strategies are also set to differ as the FOWT moves and the rotor interacts with its wake. Different strategies can be used for the turbine, helix pulse, and others. Also, hull control strategies can be implemented, as shown in the FOCAL campaign section.
- **Installation and maintenance phase:** The logistics differ from bottom-fixed offshore wind turbines for different reasons. First, the floaters are more significant, and storing capacities are needed, dry or wet. If towed out from the harbors, some harbors are unsuitable because they are too shallow. If installed in deeper water offshore, jack-up vessels might not be used anymore, and floating vessels have to be used, adding additional complexity to the installation and maintenance process.
- **Supply chain:** Currently, there are not enough ports with the right mix of quayside length, sea depth, and storage capacity to enable the simultaneous development of gigawatt-scale floating offshore wind projects. Establishing manufacturing facilities for the large-scale production of floating substructures is necessary to address this issue and guarantee that the nation's domestic supply chain can support the growth of large-scale projects.
- **Higher costs:** Following the above, the price per MWh of floating offshore wind energy is higher than for fixed bottom wind. However, in May 2024, the world's first commercial floating wind farm was awarded a purchase tariff of 86.45€/MWh.

1.2.2. Design challenges: the need for Computational Fluid Dynamics (CFD)

Numerous commercial and open-source software packages are available for modeling Floating Offshore Wind Turbines (FOWTs). This section aims to showcase the various models, highlight their differences, and explain the motivation behind using Computational Fluid Dynamics (CFD) modeling.

Low-fidelity

For early design stages, simple low-fidelity frequency domain models can be used to simulate the dynamics of the FOWT. They help gather a general understanding of the FOWT and can help make the first design choices for optimization. Some approaches can be found in [44] [79] [63].

Mid-fidelity and its limitations

Mid-fidelity software, often called engineering tools, is used for global dynamics analysis for linear and nonlinear loads. Some of the most famous engineering tools are listed below :

- **OpenFAST** is an open-source software developed by the National Renewable Energy Laboratory (NREL) in the United States. It comprises several modules that can solve the coupled aero-hydro-elastic-mooring dynamics of FOWTs in the time domain. The underlying physics are explained in [55].
- **Bladed** is developed by Det Norske Veritas (DNV). It is an aero-elastic code that can be coupled with SINTEF's SIMA for FOWT modeling [76].
- **HAWC2** is developed by the Technical University of Denmark. It is an aero-elastic time-domain solver, including a hydrodynamic solver for FOWT modeling.

Other models include SIMA, SIMPACK, or Orcaflex. More information can be found in the references, and a summarizing table is shown in Table 1.1.

Software	Hydrodynamics	Aerodynamics	Structure
FAST	PF + ME	BEMT + GDW/FVW	RB + Modal/FEM + Dyn/QS
HAWC2	PF + ME	BEMT + GDW	FEM + Dyn
SIMA	PF + ME	BEMT	FEM + Dyn
Bladed	With SIMA	BEMT + GDW	Modal
SIMPACK	With HydroDyn	AeroDyn/AeroModule	FEM
Orcaflex	PF + ME	With FAST	RB + FEM + Dyn
Flexcom	PF + ME	With FAST	RB + FEM + Dyn

Table 1.1: Tools used in engineering for FOWT modeling, taken from Otter et al. [76]

Most engineering tools above require input from frequency-domain potential flow solvers, such as WAMIT, AQWA, or Nemoh, for the hydrodynamic coefficients. The engineering tools have been compared in the Offshore Code (OC) Comparison Collaboration project, short for OC4 [93][92] [91]. However, a code comparison does not predict the accuracy of the code. OC5 has compared the simulations with experimental data done during a campaign led by MARIN [56]. From the validation of the data, discrepancies were found and included the following :

- Ultimate and fatigue loads were under-predicted compared to the experimental campaign during OC5 [93]. The largest under-predictions were found at low-frequency responses in pitch and surge due to the inability to predict the nonlinear difference-frequency loads in wave conditions correctly.
- This led to OC6 Phase I [114]. In Phase IA, quadratic heave and pitch damping were modeled using a drag force on the heave plates. However, a linear drag term or a modified Morison equation is necessary for surge decay, particularly at low KC numbers [116]. In OC6 Phase IB [115], incorporating full quadratic transfer functions (QTFs) for second-order wave theory and adding Morison drag improved results but still fell short of matching experimental data. Further experimental validation is essential to understand the nonlinear difference-frequency loads and low-frequency effects on moored platforms.

- OC7 Phase I, which is still ongoing at the time of writing, focuses on enhancing hydrodynamic modeling practices for floating offshore wind turbine (FOWT) platforms, explicitly targeting the modeling of viscous loads. The strategy involves exploring appropriate hydrodynamic model formulations for typical platform geometric components and examining how optimal hydrodynamic coefficients—such as added mass, damping, and drag—vary with different flow conditions, including various sea states. This research aims to refine existing hydrodynamic models to accommodate different conditions better.
- Differences in aerodynamics were masked by the hydrodynamic loads, separate experimental campaigns have assessed the difference in aerodynamics such as OC6 Phase III [7] and [17] which has analyzed the characteristics of the near wake and the far wake of the rotor, with particular focus on the propagation of tip vortices in the near wake. They found no significant discrepancies in loads between the different models of fidelities but recommend their use for more realistic conditions when control is included and unsteady aerodynamic models are needed. Other work from Taruffi, Novais, and Viré [105] have shown that more unsteady aerodynamics occur for different situations and most probably show discrepancies with mid-fidelity BEM-based software like OpenFAST, as shown in Ramos-García, Sessarego, and Horcas [82].
- In fixed-bottom cases, all simulation methods closely match in predicting the tip vortex position, with convection velocities broadly aligning with experimental data, but discrepancies of up to 20% are observed in vortex strength and core radius predictions, especially with CFD ALM under-predicting vortex strength despite higher computational costs. For unsteady cases, the differences between FVW and CFD methods increase, highlighting the need for further tuning to accurately predict tip vortex behavior in floating wind turbines under surge motion.

Engineering tools generally lack the essential physics needed to accurately predict key variables in FOWT. In contrast, CFD tools can accurately predict the surge and pitch loads, even though careful parameter tuning is required.

Finally, given the distinct dynamics involved in aerodynamics, hydrodynamics, and mooring systems, assessing the coupling between these forces and understanding how they interact in the context of floating offshore wind turbines (FOWTs) is crucial. This assessment becomes particularly important when comparing high-fidelity computational fluid dynamics (CFD) and mid-fidelity models, as the latter couple interacts with different dynamic models. More detailed findings and comparisons from the literature on these coupled dynamics will be discussed in chapter 2.

1.3. Research motivation

To certify a wind turbine, several tens of thousands of load cases must be run to ensure the wind turbine does not fail in any conditions. Most of these load cases can be modeled efficiently with mid-fidelity engineering models. However, these methods do not capture rotational, turbulent, or viscous effects as described previously. These effects can have a high impact on the structure, such as when breaking or focused waves are used in the case of hydrodynamics. In these cases, higher fidelity models known as computational fluid dynamics models are used to estimate wave loads better. Similarly, when looking at wind aerodynamics, some engineering models perform well in operational conditions but might need more accuracy when modeling extreme loads or understanding some nonlinear effects, which are different for FOWT compared to fixed wind turbines due to the movement of the platform.

Ideally, the high-fidelity and mid-fidelity models would be compared against full-scale prototypes for validation. However, these prototypes are very costly. Scaled models can be built for fixed wind turbines, and Reynolds scaling can validate numerical codes, investigate different phenomena, and assess design procedures. Similarly, in the shipbuilding industry, Froude scaling can be used to design robust and efficient ships. However, with floating wind turbines, it is impossible to do so since both scaling laws would have to be satisfied simultaneously to have a small-scale model of the FOWT. Different approaches have been developed to use scaled physical models where either Froude scaling is respected and wind loads are reproduced through wind fans, or where Reynolds-scaled wind turbines are mounted on a hexapod that mimics the hydrodynamics, commonly known as hybrid testing. Tradeoffs have to be made between high-fidelity hydrodynamics and aerodynamics.

With High-performance computing progressing, another way to build and validate mid-fidelity models

is computational fluid dynamics (CFD) simulations. A well-validated CFD can be an alternative to expensive experimental testing campaigns for FOWTs [76]. There isn't much real-world or full-scale experimental data available for the FOWT market, which is still in its beginnings. As it is becoming more and more necessary to build clean and renewable power generation technologies, high-fidelity CFD validation can be a valuable tool for quickly and affordably designing trustworthy and effective FOWT.

Many efforts have been made to validate the hydrodynamic and aerodynamic models separately, as these can be compared to scaled models. Combining them is a more difficult challenge since it involves coupling both aerodynamic and hydrodynamic models. Fully coupled mid-fidelity models such as FAST can be used for some simulations; however, CFD simulations are needed to get a deeper understanding of physical phenomena. Almost all the CFD analyses of semi-submersible FOWT are concentrated around the Deep-Sea floater, on which a 5MW wind turbine is mounted on top. However, the mounted wind turbines do not correspond to the projected new wind turbines coming on the market when FOWT is effectively deployed. Therefore, the IEA has published a new semi-submersible concept, the VolturnUS-S floater with the IEA 15MW wind turbine mounted. This open-source model aims to have a common framework and investigate the effects of bigger turbines. Some experimental campaigns have examined the FOWT's behavior and reproduced the latter.

Adding to that, most of the few coupled CFD models used in the literature use software that is not open source and use most of the time ANSYS-Fluent, STAR-CCM, or Bladed, for example. Open source Computational Fluid Dynamics (CFD) models are essential because they are free and accessible to everyone, including students, researchers, and small companies. They save money and allow users to see and improve the code, making it more reliable and helpful for specific needs. The open-source community helps by sharing knowledge and fixing problems quickly. This collaboration speeds up research and development in many fields, making advanced CFD tools available to more people and promoting innovation and learning. The most popular open-source CFD modeling software is OpenFOAM.

Two previous students have used OpenFOAM to model a FOWT accurately [81] [98]. They have developed a framework for the FSI simulation of FOWTs based on the relaxation zone method -for wave-field generation and absorption, using the Waves2Foam library— and actuator line method — for rotor modeling using turbinesFoam— has been implemented in OpenFOAM. The latter has been adapted to work with floating turbines and coupled to OpenFOAM's rigid body solver. However, they haven't used to compare it to a more important floater, and only constant thrust has been modeled so far.

1.4. Research objective and research questions

Considering all the above, the research objective is the following :

Develop and verify the setup of a high-fidelity, open-source CFD model using OpenFOAM to simulate the aerodynamic and hydrodynamic behavior of the IEA 15MW Floating Offshore Wind Turbine (FOWT) on the VolturnUS-S semi-submersible platform and compare the results with mid-fidelity models to determine differences in modeling.

The questions that will be answered in the present research are the following :

- How do decay tests of the VolturnUS-S floater in OpenFOAM using waves2foam and a FEM model compare with mid-fidelity models like OpenFAST for large motions? What differences in damping can be observed?
- How do simulations of the IEA 15MW wind turbine using turbinesFoam compare to OpenFAST simulations models for both steady and prescribed harmonic motions?

1.5. Thesis outline

This thesis will provide an in-depth analysis of floating offshore wind turbines (FOWTs) and their computational modeling, explicitly focusing on verifying the performance of the VolturnUS-S floater and the IEA 15MW wind turbine using computational fluid dynamics (CFD). It will start by reviewing critical concepts from the literature and various modeling theories in chapter 2, covering hydrodynamics, aerodynamics,

and mooring dynamics. In chapter 3, a detailed description of the floater's characteristics, including a convergence study, will be provided. The latter will be followed by verification and comparison with OpenFAST, along with the addition of a validation framework for future work. In chapter 4, we will examine the aerodynamics of the IEA 15MW wind turbine. The chapter will also include a discussion on experimental benchmarks for validation and an analysis of the discrepancies between OpenFAST and OpenFOAM setups. The aim is to verify the correct implementation of the IEA 15MW model. Finally, chapter 5 summarizes the essential findings and offers recommendations for future research.

2

Background theory

This chapter will recap the critical information about floating wind turbines and their computational modeling. It will summarize essential points from two previous master theses[98] [81], which will be mentioned when relevant. Additionally, new information that is more specific to the focus of this thesis will be included to provide a well-rounded overview of the topic.

2.1. Analytical theory

2.1.1. Hydrodynamics of FOWT

Floating hydrodynamic stability and floater designs

This subsection aims to focus on the basics of static floating stability for readers who do not have a hydrodynamics background. More details can be found in specialized literature [73].

A standard method is to examine the motion of the body near static equilibrium, where the hydrostatic (or buoyancy) force $\mathbf{F}_{\mathrm{h}}$ and external forces (such as gravity, environmental, or mooring loads) $\mathbf{F}_{\mathrm{ext}}$ and moments $\mathbf{M}_{\mathrm{ext}}$ are balanced. Some examples are in [98] [81]. It is important to note that surge, sway, or yaw motions (translations or rotations along the water surface) do not alter the submerged volume and, thus, do not affect the equilibrium position. Similarly, heave motions do not create moments about the center of gravity and, therefore, do not disturb the stable equilibrium. Only pitch and roll can impact stability by causing movement of the centers of buoyancy and gravity.

This section will focus on the basics of static floating stability for readers who do not have a hydrodynamics background. More details can be found in specialized literature [73].

Using Archimedes' principle, the buoyancy force acting on a floating platform can be calculated as the weight of the displaced fluid. Buoyancy forces can also be described as the vertical component of the integrated hydrostatic pressure along the wet surface [21], which acts as an upward force that counters the weight as described in Equation 2.1. It acts at the center of buoyancy B, which is the center of mass of the displaced fluid.

$$\mathrm{d}\mathbf{F_h} = -p_h \mathbf{n} \mathrm{d}S \quad \int_S \mathrm{d}\mathbf{F_h} = \sum \mathbf{F}_{\mathrm{ext}} \tag{2.1}$$

Considering the weight acting as an external force at the center of gravity G, along with the vertical mooring force of the floating turbine, equilibrium is achieved by integrating over the wet surface, focusing on the vertical component:

$$\rho g V = mg - F_{MZ} \tag{2.2}$$

For freely floating bodies like ships, the buoyancy force and the weight balance out. For an offshore floating wind turbine, the buoyancy force can be higher than the weight due to the downward force of

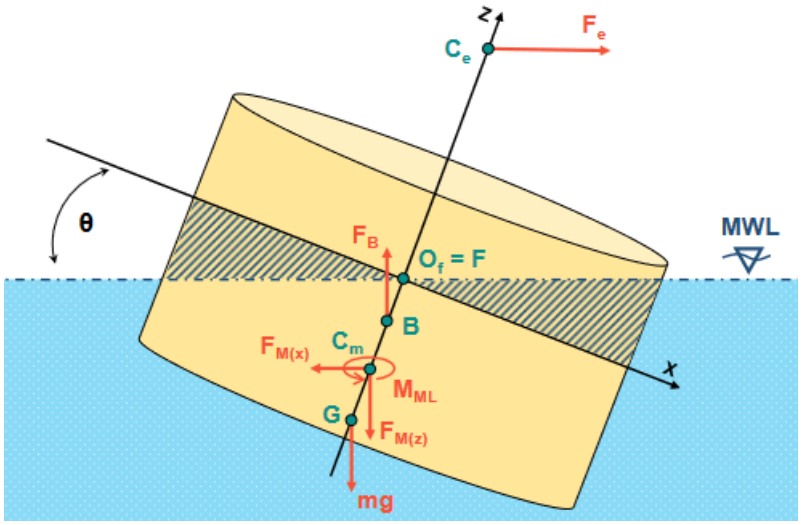

Figure 2.1: Force diagram of a generic floating wind turbine [81]

the mooring system ($F_{MZ} < 0$).

However, a floating structure achieves stability when it returns to equilibrium after being disturbed by an external force or moment. Thus, the moments should be balanced too.

$$\int_S \mathbf{r} \mathrm{d}\mathbf{F_h} = \sum \mathbf{M}_{\mathrm{ext}} \tag{2.3}$$

In ship stability, the center of gravity (G) is typically positioned below the center of buoyancy (B), ensuring stability. However, in the case of Floating Offshore Wind Turbines (FOWTs), the center of gravity (G) may be situated above the center of buoyancy (B). Consequently, in FOWT hydromechanics, it is expected to differentiate three primary factors that contribute to stability: the restoring moment generated by the waterplane area, the restoring moment influenced by the relative positioning of B and G, and the restoring moment derived from the mooring system. Detailed calculations for each contribution can be found in the thesis of Scarlatti [98].

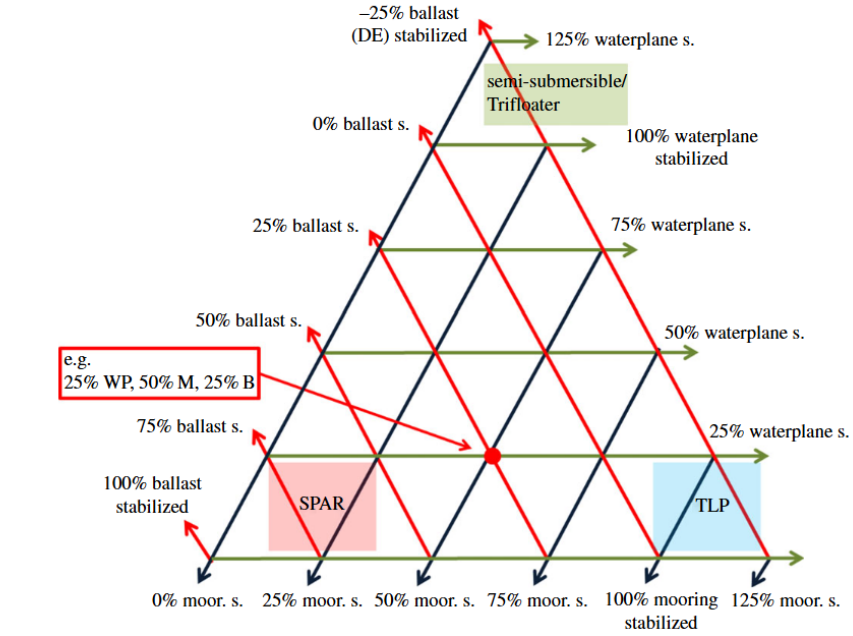

(a)

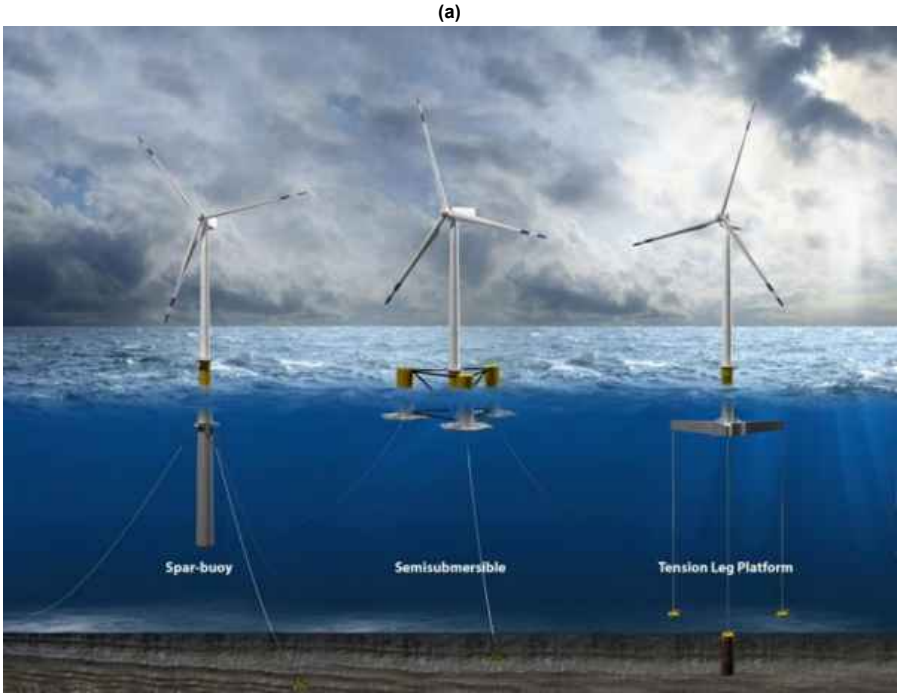

(b)

Figure 2.2: Stability Triangle: The three corners of the triangle represent the three stabilization mechanisms utilized by floating wind turbine systems [64] (a); Resulting floating structure designs for FOWT [43] (b).

Figure 2.2a provides a comprehensive summary of hydrostatic stability, comparing the primary drivers of static stability for the three main floater concepts. The percentage contribution of each stabilization mechanism is illustrated on the sides of the triangle, which explains the three main design choices currently used in the industry as depicted in Figure 2.2b.

Wave theories and sea state characterization

Waves and currents affect FOWT's movement and stability. These environmental forces also create extreme fatigue loads, which can cause wear and tear or even damage the structure over time. This

makes it essential to account for these stresses during the design and analysis stages for the system's longevity and performance. Additionally, waves and currents make installation and maintenance more challenging, requiring special techniques and equipment to handle these conditions safely and effectively. Understanding and managing these impacts is critical to keeping floating wind turbines running smoothly, so it is crucial to have accurate models to model the loads. This section will only focus on waves and wave loads, as current loads are beyond the scope of this thesis.

Linear wave theory: Airy theory The Linear Wave Theory, also known as Airy theory, is the simplest method for describing regular waves, particularly ocean waves with a small amplitude compared to their wavelength [18]. The theory behind the potential flow solvers is used in engineering models. According to the first-order Airy theory, water is treated as incompressible, inviscid, and irrotational. Due to these properties, a velocity potential (ϕ) exists that satisfies the Laplacian equation ($\nabla^2\phi = 0$). This theory follows the potential flow framework and requires three linearized boundary conditions to be accurately described:

- **Kinematic bottom boundary condition**: The flow velocity at the sea floor must be zero.
- **Free surface dynamic boundary condition**: The water pressure at the free surface must equal atmospheric pressure.
- **Free surface kinematic boundary condition**: No water flow is permitted through the free surface.

By combining these three boundary conditions and linearizing them, the following second-order differential equation is derived:

$$\frac{\partial^2\phi}{\partial^2 t} + g\frac{\partial\phi}{\partial t} = 0 \tag{2.4}$$

The resulting potential function and the harmonic wave expression for regular waves can be expressed as :

$$\begin{aligned} \phi(x,z,t) &= \xi_a \frac{g}{\omega}\frac{\cosh(k\cdot(h+z))}{\cosh(kh)}\sin(kx-\omega t), \\ \xi(x,t) &= \xi_a \cos(kx-\omega t) \end{aligned} \tag{2.5}$$

With the free surface boundary condition, the following dispersion equation is obtained :

$$\omega^2 = kg\tanh(kh) \tag{2.6}$$

At this point, it is essential to distinguish between deep and shallow waters to simplify the dispersion relation accordingly. The table below summarizes deep and shallow water wave criteria and their corresponding dispersion relations.

Water Type	Depth to Wavelength Ratio	Simplified Dispersion Relation
Deep Water	$\frac{h}{\lambda} > 0.5$	$\omega^2 = kg$
Shallow Water	$\frac{h}{\lambda} < \frac{1}{20}$	$\omega = k\sqrt{gh}$

Table 2.1: Distinction between deep and shallow water waves and their respective dispersion relations.

The water particle trajectory is also affected by the depth as shown in Figure 2.3 :

According to literature [18] and DNV guidelines on the design of offshore wind structures, the Airy theory is valid for small amplitude waves and deeper water depths and is used in many mid-fidelity solvers.

The primary benefit of linear wave theory is its capability to employ superposition, allowing complex, irregular wave systems to be modeled using the Fourier series. This approach combines numerous waves with different amplitudes and frequencies to approximate the desired wave pattern. The connection between these amplitudes and frequencies is defined by the spectral density function $S(\omega)$ such as JONSWAP or Pierson-Moskowitz spectra, which can then be used to determine wave periods and height. These are used to analyze real-world environmental conditions. By conducting 3-hour time-domain simulations using mid-fidelity software, it becomes possible to decide on the standard statistical Most Probable Extreme (MPE) values for motions and loads that follow a Rayleigh distribution.

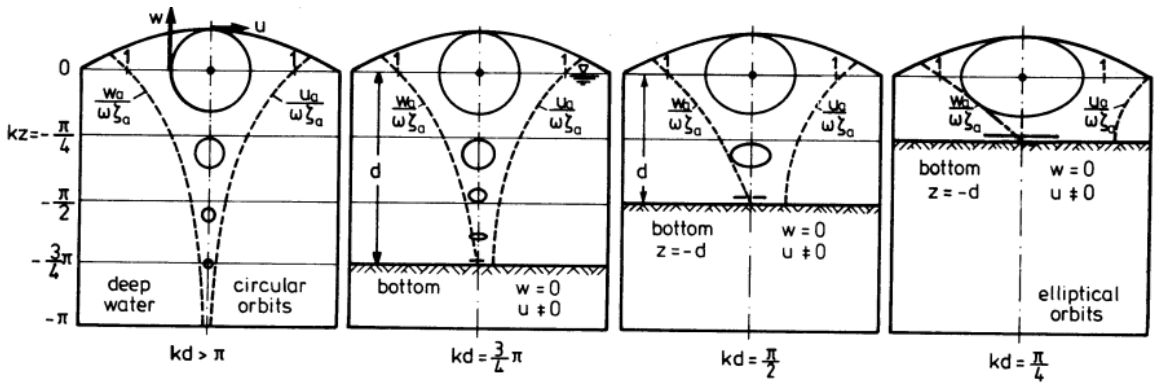

Figure 2.3: Comparison of deepwater and shallow water waves for the linear wave theory [18]

These MPE values can then inform structural considerations for the Ultimate Limit State (ULS) analysis of critical components, ensuring their reliability and safety under extreme conditions.

Nonlinear wave theory: Example of the second order Stokes theory:

In the following chapters of this thesis, second-order Stokes waves are selected for the CFD simulations using `waves2Foam`. Those waves are used for cases where linear waves are too imprecise, such as focused waves, that can induce extreme loads. While first-order Stokes theory is identical to Airy theory, second-order Stokes wave theory introduces differences by producing waves with steeper crests and broader troughs, as shown in Figure 2.4.

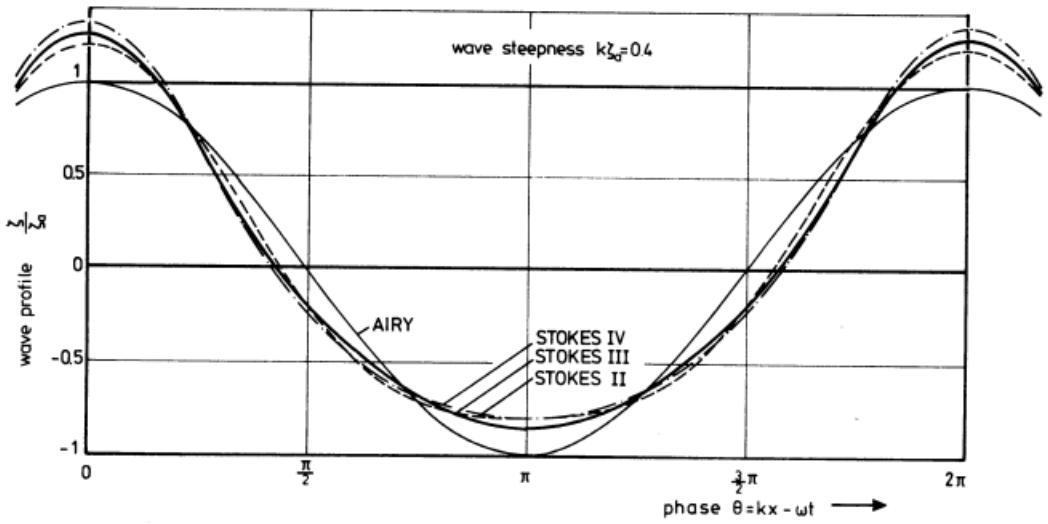

Figure 2.4: Changes in the wave profile with higher orders of Stokes wave theory [18]

In the Airy theory, the kinematic and dynamic surface conditions have been linearized by ignoring the terms related to wave slope and convective acceleration, allowing for the derivation of linear wave theory [18]. The velocity potential and the surface elevation can be expanded in power series. After truncating the procedure after second-order terms, one gets conditional equations for second-order potentials and wave elevations. For more details, one can refer to [18].

The resulting velocity potential and the surface elevation can be written as:

$$\begin{aligned} \frac{k^2}{\omega}\Phi &= (k\zeta_\mathrm{a})\,\frac{\cosh k(z+d)}{\sinh kd}\sin\theta + \frac{3}{8}(k\zeta_\mathrm{a})^2\,\frac{\cosh 2k(z+k)}{\sinh^4 kd}\sin 2\theta \\ k\zeta &= (k\zeta_\mathrm{a})\cos\theta + \frac{1}{4}(k\zeta_\mathrm{a})^2\,\frac{\cosh kd}{\sinh^3 kd}[2+\cosh 2kd]\cos 2\theta \end{aligned} \tag{2.7}$$

From the previous equations, it is evident that second-order Stokes theory extends the Airy theory described in Equation 2.5 by incorporating second-order terms into the equations of the linear theory. While extending this approach up to the fifth order is possible, doing so becomes computationally expensive and thus impractical for our cases. It has to be noted that Stokes waves are not suited for shallow waters; one should use cnoidal or stream function wave theories, which are other nonlinear wave theories.

In conclusion, wave propagation phenomena depend highly on water depth and height. Steep waves and shallow waters present significant modeling challenges that linear theory often fails to address accurately. Due to the importance of predicting wave loads in engineering, considerable effort has been dedicated to defining the range of applicability for various wave theories as shown in Figure 2.5. This ensures that the most appropriate models are used for different conditions, improving the accuracy and reliability of wave load predictions.

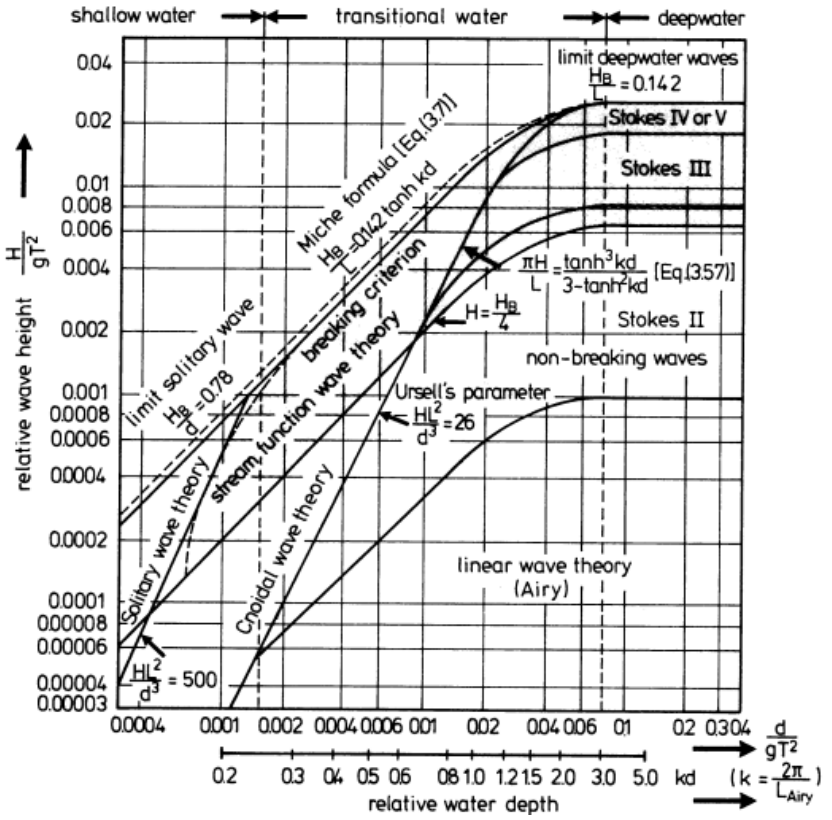

Figure 2.5: Breaking wave height and regions of validity of various gravity water wave theories [18], inline with DNV recommendations [24]

2.1.2. Mooring dynamics for FOWT

The mooring system's dynamics impact the platform's global motion responses to the entire structure through the restoring force. Depending on the modeling theories, the line tensions and the extreme loads can differ[40]. For the mounted wind turbines to generate electricity, the mooring mechanism is. Therefore, crucial [88].

General knowledge on mooring line theories

Mathematical models of mooring lines can be categorized into the following categories :

- **Quasi-Static Model:** This model assumes the motion is linear and uniform between two static positions within a given time step, where loads are considered constant. Quasi-static models use catenary formulations to derive mooring line shape and tension, assuming static equilibrium at each time step, neglecting inertia effects, and assuming the line profile follows catenary equations.

These models do not account for the impact of mass, damping, and fluid acceleration on the lines's motions. Consequently, quasi-static models overlook hydrodynamic and inertial forces on the line, which can affect the structural response and are crucial for predicting mooring loads [126]. However, quasi-static models offer computational efficiency and can be suitable for cases with minimal wave activity and low platform and mooring line velocities [67]. General findings agree that incorporating mooring dynamics in the aero-hydro-elastic analysis of FOWTs is necessary for evaluating mooring line loads in both mild and severe environmental conditions [11].

- **Dynamic Models:** Described by Newton's second law, these are the most accurate for predicting mooring tensions, loads, and snapped loads caused by additional inertia and hydrodynamic forces. These models involve linearizing the system or using numerical techniques to approximate the nonlinear differential equations governing the system. Dynamic mooring models can be broadly classified into four categories: *Lumped Mass (LM)* method, *Multi-Body Dynamics* (MBD) method, *Finite Difference Method (FDM)*, and *Finite Element Method (FEM)*. This section does not aim to describe all the models fully. For mathematical details, refer to Scarlatti [98] and Zhong et al. [126]. Instead, it will reference the various applications of the different models.

	Lumped Mass model	**FEM models**	**FDM**
References	Hall et al. [41], Jiang et al. [54]	Palm et al. [77]	Chen et al. [11]
Validated against (among others)	OC4 DeepCWind	DeepCWind and compared for VolturnUS-S	Demonstrated via modeling a subsea unit towed by a maneuvering vessel.
Opensource software	`MoorDyn`	`Moody`	`OpenMOOR`

Table 2.2: Summary of different dynamic models and their applications.

Several studies compare quasi-steady and FEM dynamic models for simulating floating offshore wind turbines:

- Masciola et al. [66] found that mooring dynamics influence platform motions primarily when those motions are significant and that dynamic response is crucial for accurately predicting mooring line loads.
- More recently, Zhong et al. [126] have conducted a comparison study to obtain insights into the performances of six mooring line models, quasi-static and dynamic models. They have concluded, among other things, that LDG FEM (i.e., `Moody`) exhibits the best performance because it is more accurate to model the behavior of snap loads. For coupled mooring dynamic models, they recommend LM and LDG FEM, the latter having slight unpredictable tension fluctuations over the motion cycle. These results align with Scarlatti's master thesis [98].

In conclusion, CFD software coupled with a quasi-static mooring model can adequately predict structure motions but not mooring loads for platforms with small motion responses. For platforms with high motion responses, a dynamic mooring model is necessary. Since one of the goals of this thesis is to build a framework that can act in any condition, an LDG FEM model, `Moody`, in this case, is chosen and will be described in the next section.

LDG FEM

The following are equations that are taken out of the manual of `Moody` and describe the equations that govern the motions :

For a cable of length L_c, we describe its position in global coordinates using the unstretched cable coordinate $s \in [0, L_c]$. The position vector of the cable is given by $\mathbf{r} = [r_1(s), r_2(s), r_3(s)]^{\mathrm{T}}$. Assuming the cable has negligible bending stiffness, the equation of motion can be written as follows:

$$\begin{aligned} \gamma_0 \ddot{\mathbf{i}} &= \frac{\partial}{\partial s}(T\hat{\mathbf{t}}) + \mathbf{f} \\ \hat{\mathbf{t}} &= \frac{\partial \mathbf{r}}{\partial s}\left|\frac{\partial \mathbf{r}}{\partial s}\right|^{-1} \end{aligned} \tag{2.8}$$

where γ_0 is the cable mass per unit length, T is the cable tension force magnitude, $\hat{\mathbf{t}}$ is the tangential unit vector of the cable and $\mathbf{f}$ represents all external forces. For notation we use $\dot{x} = \frac{\partial x}{\partial t}$ to indicate time derivatives and $|\mathbf{x}| = \sqrt{x_i x_i}$ to denote the L_2 - norm of a vector quantity x, Vector components are denoted by their index as $x_i, i \in [1, 2, 3]$, and summation over repeated indices is implied.

The total external force f of Equation 2.8 is given by

$$f = f_a + f_b + f_c + f_d \tag{2.9}$$

where f_a is the added mass and Froude-Krylov forces, f_b is the net force of gravity and buoyancy, f_c represent contact forces, typically from sea-floor interaction, and f_d is the viscous drag force.

In this model, cable bending stiffness is neglected. `Moody`'s code is not as open source as `MoorDyn`. However, it is available as a precompiled shared library that can be dynamically linked as a DLL with OpenFOAM software, for example. It has to be noted that their authors have recently released `MoodyCore`, which is a command-line interface that is an improvement to `Moody 2.0` aka `Moody` [29]. No linkage with OpenFOAM has been released by the time of the writing, which is why `Moody 2.0` will be used for the following.

2.1.3. Aerodynamics of FOWTs

The advanced design of modern wind turbines suggests a comprehensive understanding of the underlying aerodynamic principles. However, wind turbine aerodynamics remains a highly complex and unresolved field today. Simplified modeling tools for rotors can sometimes lead engineers to overlook the complex flow phenomena affecting turbine performance. The complexity increases further when considering the additional six degrees of freedom in floating offshore wind turbines (FOWTs). This section briefly reviews the aerodynamics of traditional horizontal-axis wind turbines (HAWTs) and the additional challenges posed by floating conditions. References will be given to the more curious readers.

General knowledge of Horizontal axis wind turbines (HAWT)

Many different phenomena are to be considered when explaining how HAWT works. However, one can easily explain how energy is extracted from the wind by implying assumptions using the actuator model. This method can be generalized to any turbine design. The power of a wind turbine comes from the kinetic energy of the air that passes through it. The gradual velocity decrease originated from a steep pressure jump across the rotor plane. Using assumptions and applying basic conservation principles to the expanding stream tube, one can calculate the following:

$$U_D = (1-a)U_\infty \quad , \quad U_W = (1-2a)U_\infty \tag{2.10}$$

Where U_∞, U_D, and U_W are the freestream, disk, and far wake wind speeds, respectively, and a is referred to as the axial induction factor.

The expression above indicates that half of the axial speed reduction occurs upstream of the rotor. This information is useful for assessing the forces on the rotor and the power extracted from the wind, which are typically represented by non-dimensional coefficients. These coefficients are given by:

$$C_T = \frac{\text{Thrust}}{\frac{1}{2}\rho U_\infty^2 S} = 4a(1-a) C_P = \frac{\text{Power}}{\frac{1}{2}\rho U_\infty^3 S} = 4a(1-a)^2 \tag{2.11}$$

The maximum achievable value for C_P is approximately 0.593, which corresponds to $\frac{16}{27}$ and occurs at $a = \frac{1}{3}$. This is known as the Betz limit. This value is theoretical and based on the idealized assumption of energy extraction without considering specific turbine designs. The Betz limit represents the optimal

trade-off between extracting kinetic energy from the wind and maintaining sufficient mass flow through the rotor. If we were to extract all the energy from the wind, the wind speed would drop to zero, resulting in no net flow passing through the turbine.

Blade Element Momentum (BEM) Theory

This method is most used in low/mid-fidelity models such as OpenFAST. The blade is discretized into blade elements. This method assumes that the forces on the blade elements can be determined using airfoil 2D polar data, such as angle of attack and lift and drag coefficients. BEM models can be improved using dynamic stall models such as the Beddoes-Leishman dynamic stall model to calculate unsteady aerodynamics or tip and root loss corrections models based on empirical corrections. The Glauert Correction improves the accuracy of BEM under high thrust conditions. Yaw correction can also be implemented to represent better the complex flow patterns that develop when the rotor is yawed, leading to more accurate power output and load predictions. Detailed calculations can be found in Dos Santos Malveiro's Msc. Thesis [9] and in the reference manual. Despite all these correction methods, BEM still has limitations in more complex flow scenarios.

Free Vortex Wake (FVM) Methods

Momentum-based approaches are conceptually simple but rely on several correction models, which are often empirical. Acknowledging that the external flow around a wind turbine is typically inviscid, incompressible, and irrotational allows for applying potential flow methods. The free vortex wake method (FVM), a subset of the potential flow technique, is another way of modeling wind turbine aerodynamics. Since potential flow theory allows for the superposition of elementary flows, vortex filaments, which are elementary flows, are used to model the continuous vorticity distribution using a finite number of elements. In the context of blade aerodynamics, the blades are modeled as a single lifting line, which is discretized into elements. Each element has a particular circulation according to the load on the blade elements. The vortex filament nodes move as Lagrangian markers with the local fluid flow. The wake lattice grows over time as the wake nodes are advected. The vorticity equation can be used to model the vorticity distribution in the wake using the Biot-Savart Law. The induced velocities of each filament can be calculated and then summed up to calculate the velocity distribution in the wake. More detailed information can be found in C. Dos Santos Pereira Malveiro [9] and Sebastian and Lackner [99]. It can generally provide more accurate calculations when the BEM assumptions are violated. Within OpenFAST, the OLAF model has been developed as a free vortex wake module in the Aerodyn model.

Actuator Disk model

The actuator disc model (ADM) involves using an actuator disc that applies forces to the fluid flowing through it. These forces can represent thrust or a combination of thrust and tangential forces. This approach allows for modeling wind turbine blades as a rotor disc, enabling the simulation of the resulting wake. However, it is essential to note that the ADM cannot simulate the tip vortices generated by the blades. The thrust does not consider the rotation in the flow caused by the blades. It can be uniformly loaded or changed depending on the radial position. Polar tables of airfoils can then be used to calculate the new force distributions, where the expression of the forces resembles Equation 2.11, except that the inflow velocity can be different than U_∞ since the turbine can be in the wake of another one. When comparing the actuator disc model to fully resolved blade simulations, it is a good approximation for mean flow values at distances of at least one rotor diameter away from the wind turbine [90]. However, the ADM is not well-suited for calculating the near wake of a wind turbine because it does not capture tip vortices, root vortices, or other vortical structures in the near wake. Despite this limitation, the ADM is influential for wind farm calculations, where the focus is on far wake effects over more considerable distances, and multiple wakes need to be considered [9].

Actuator line model

The actuator line model (ALM) was first introduced by Sørensen and Shen [102], and it represents each blade as a discretized actuator line, which is a thin line where aerodynamic forces (lift and drag) are applied. For each blade section, the direction and velocity of the local incoming flow are determined using blade element theory. The adequate inflow is influenced by the freestream and rotational velocities and the axial and azimuthal induction factors, which account for the non-uniform load distribution over the actuator disc and potential rotor motion. The angle of attack α experienced by the airfoil is calculated from the effective velocity angle ϕ and the blade section's pitch and twist angles ϵ. Lift and

drag forces, along with their projections (axial and in-plane forces), are then associated with each blade element based on tabulated airfoil data and the corresponding angle of attack.

Thus, the force at each section is expressed as:

$$\vec{f}_{AL} = \frac{1}{2}\rho V_{\text{eff}}^2 c(C_l \vec{e}_L + C_d \vec{e}_D) \tag{2.12}$$

where C_l and C_d are the lift and drag coefficients, c is the chord length, and V_{eff} is the local inflow velocity at the blade element. A limitation of this approach is the need for accessible lookup tables for the specific blades considered. Although this method is more complex and computationally demanding than simpler methods like the actuator disc method (ADM), it offers a more detailed representation of loads, including spanwise distribution and rotational effects. While ALM may not capture complex phenomena, such as the transition from laminar to turbulent flow or separation over the blades, it can effectively generate root and tip vortices.

The efficiency of the Actuator Line Model (ALM) is well-established, having been used successfully in numerous applications for floating offshore wind turbines (FOWTs) [2][17][68][75][103][108]. In the case of FOWTs, the unsteady inflow caused by platform motion must be considered when calculating blade loads. This is accomplished by incorporating the platform velocity into the blade element velocity triangle. A more detailed literature review will be presented in Chapter 4, where the aerodynamics of the IEA 15MW wind turbine will be given.

The forces are smeared across the neighboring cells to avoid numerical instabilities through a 3D Gaussian convolution. This is achieved by convolving the calculated local load f with a regularization function η_ϵ, as shown in Equation 2.13.

$$f_\epsilon = f_{AL} \otimes \eta_\epsilon \tag{2.13}$$

The regularization function η_ϵ is defined by Equation 2.14 [2] :

$$\eta_\epsilon(d) = \frac{1}{\epsilon^2 \pi^{3/2}} \cdot \exp\left[-\left(\frac{d}{\epsilon}\right)^2\right] \tag{2.14}$$

This equation, $d = |x - s_i|$, represents the distance between the cell-centered grid points and the point of the i'th actuator line. The parameter ϵ can be adjusted to modify the concentration of the force distribution.

The choice of ϵ is critical as it must be large enough to guarantee stable computations (no singularities) and small enough to provide accurate results. If the spreading radius is too large (i.e., for a value of ϵ/c that is higher than 0.25 while maintaining $\epsilon/\Delta_x \simeq 2.8$, the blade torque and power are too high, sometimes even exceeding the Betz limit as explained in Stanly et al. [104]. Spyropoulos et al. [103] have tested the accuracy of an actuator line model on aeroelastic simulations of wind turbines using URANS simulations. They have tested the DTU 10MW by doing a sensitivity analysis on several simulation parameters, such as the Gaussian kernel value ϵ. In literature, mainly two strategies are implemented either based on Δ_x, which fails to give a grid-independent solution, or proportional to the chord c of each blade section. The proportionality factor of 0.47 is selected so that the Gaussian projection of aerodynamic forces is limited to 1c around the emission points, with the projection width defined as $3\sigma = 3\sqrt{2}\epsilon$, meaning the projection extends to a distance of three standard deviations (3σ) from the mean of the Gaussian distribution. If the projection is designed to reach 1c, then $c = 3\sqrt{2}\epsilon$, implying $\epsilon \simeq 0.47c$. This approach enables detailed resolution of blade geometry and fine grid resolution near the actuator line (AL). Still, the reduction in chord length near the tip can cause e to become smaller than Δx, potentially leading to numerical singularities. To avoid this, a minimum value for e, emin = 2Δx, is established, as the literature recommends. Setting $\epsilon = max(2\Delta_x, 0.47c)$, it is shown that the measured power varies less with the grid refinement than with the individual strategies mentioned above, and chosen $\Delta_x = R/90$, while $\Delta_x = R/60$ still gives acceptable results.

The number of blade strips was also investigated through their length Δ_r, and it was found that even though $\Delta_r = 1.5 * \Delta_x$ gives acceptable results. The timestep Δ_t is then examined. In most Actuator Line (AL) implementations, Δt is typically chosen so that the blade tip crosses at most one cell between consecutive timesteps ($\Delta_t = \Delta_x / V_{tip}$). Stricter criterions can achieve better results ($\Delta_t = 0.5 * \Delta_x / V_{tip}$) is necessary for wind turbine (WT) simulations [103][20].

When compared to blade resolved simulations, which are used when the blade aerodynamics are essential and flow physics are investigated, Melani et al. [68] have shown that ALM predicts more diffused vortex, leading to an underprediction in vortex intensity, especially when the blade loading increases. Alternative kernel shape does not meet ALM's predictions and may be less suitable for use. They also highlight the importance of decreasing the force smearing and angle of attack sampling approaching blade extremity when the tip effects are modeled in the ALM framework. The central drawback is the ALM's dependence on 2D airfoil polar data, which is why dynamic stall models and other correction models are included in the models.

With the ALM, the CFD mesh does not need to conform to the rotation of the blades, which simplifies the modeling process. Overset grid methodologies can also be avoided when assessing interactions between the rotor wake and other configurations, such as wind turbine towers. Nacelle and towers can also be modeled using actuator lines as shown in [20]. Aeroelastic simulations can also be performed with fewer implementation difficulties, as the computational grid remains fixed and does not need to deform along with the blades.

2.1.4. Coupled CFD simulations

This section is a review of some of the relevant fully-coupled solvers. Other CFD simulations are reviewed in some other reviews [120] [101] [76] [39]. Even though this thesis will not perform any coupled simulations, this section highlights the need for coupled simulations of large FOWT due to scarce literature.

Uncoupled vs. partially coupled vs. fully coupled

In the analysis of FOWTs, three main approaches are used to simulate fluid-structure interactions: uncoupled, partially coupled, and fully coupled simulations. Uncoupled simulations examine hydrodynamic and aerodynamic forces independently, allowing researchers to focus on specific behaviors under simplified conditions. This approach reduces computational cost but may overlook the combined effects of wind and wave forces, leading to oversimplified outcomes but good first approximations. The results have been covered in the previous sections. Partially coupled simulations, on the other hand, incorporate some interaction between forces by accounting for specified motions in certain degrees of freedom (DOF), offering a more realistic representation than uncoupled methods but still lacking full interaction dynamics. It has been found by Tran and Kim [107] that surge and pitch DOF significantly affect the aerodynamics of FOWT. Wu and Nguyen [119] have found discrepancies between OpenFAST and OpenFOAM while modeling large-scale motions. Usually, these are one-way interactions, meaning the hydrodynamic loads of the turbine are transmitted to the turbine through the tower. Still, the aerodynamic loads do not affect the motion of the floater. Fully coupled simulations involve a bi-directional coupling between the turbine's aerodynamic loads and the floater's rigid-body motion, where each system influences the other. This partitioned approach, with sub-iterations, allows for a comprehensive representation of FOWT's dynamic behavior, capturing the complex interactions between wind, waves, and the structure itself. While fully coupled simulations are computationally intensive, they provide the most accurate results for FOWT performance analysis.

Aero-Hydro-mooring coupling

Cheng, Huang, and Wan [14] have developed team developed the CFD solver `naoe-FOAM-SJTU` to investigate hydrodynamic problems in ship and ocean engineering, integrating the unsteady actuator line model (UALM) into OpenFOAM for wind turbine aerodynamic simulation, solving the RANS equations with the $k-\omega SST$ turbulence model and PISO algorithm. Using the overset meshing technique, a quasi-static PEM model was chosen to model the moorings. The established coupled solver `FOWT-UALM-SJTU` was validated against experimental data, including Phase II of OC4. Results showed that turbine aerodynamics significantly influence platform motion and vice versa, with notable differences in thrust and power oscillations compared to steady-state simulations. The study also highlighted the complexity of

coupling interactions between turbine aerodynamics and platform hydrodynamics, indicating the need for further research. The same research team also compared the `FOWT-UALM-SJTU` model with another in-house code called `naoe-FOAM-os-SJTU` [15] Cheng, Wan, and Hu [16], where the second differs from the first by the modeling of the blades. Instead of using UALM, the blades were modeled, leading to lower computational efficiency and more detailed flow information for further deep mechanisms. The thrust is slightly overestimated with the UALM model, and, thus, a slight overvalue in surge motions when modeling the OC4 DeepCWind with the NREL 5MW wind turbine. The same solver has been tested with the OC3-Hywind spar platform mounted with the NREL 5MW wind turbine by Huang, Cheng, and Wan [47]. They found a negative effect on the aerodynamic power output due to the motions of the platform. By comparing a parked wind turbine with a fully coupled wind wave excited wind turbine, they concluded that the aerodynamic loads significantly influence the platform motions. Also, the motion response of the platform suggests a strong interaction between the rotor and its wake.

Zhang and Kim [125] used STAR CCM+ with the overset mesh technique to develop a fully coupled model of the OC5 semi-submersible floater. They have found heavier loads on the hub and the blades, leading to a higher thrust curve than an onshore wind turbine. The power curve, however, decreases, which could be due to the smaller project area due to the pitched platform. Unsteady flows due to blade tower interferences and turbulent wakes were also analyzed. They used a quasi-static model for the moorings.

Tran and Kim [107] have built a CFD model of the OC4 DeepCwind floater mounted with the NREL 5MW wind turbine based on the overset meshing technique. A quasi-static mooring solver models the mooring constraints, and the FOWT is considered a rigid body. The rotor and the tower are modeled like in a usual FSI approach, meaning the model is also blade resolved. The model is then tested in normal wave-wind conditions and compared to OpenFAST, using either BEM or GDW to model the aerodynamics. Significant discrepancies have been noticed for wind-wave coupling conditions, especially for the amplitudes of c_P and c_T over time. The importance of an accurate unsteady aerodynamic theory was assessed as FAST-BEM and FAST-GDW, which result in similar motions but significant differences in the thrust and power coefficients. A surge offset was also observed because of the additional force acting on the rotor, thus acting on the floater's position.

Zhou et al. [127] developed a fully coupled OpenFOAM model of the DeepCWind+NREL 5MW FOWT, in which they used `waves2Foam` for the numerical wave generation and the inbuilt quasi-static model for the moorings. They investigated the FOWT for five different wave steepnesses for both regular and focused waves. They found that the motion responses become highly nonlinear as the wave steepness increases. By comparing the simulations with the ones of potential flow solvers, they found that are not adequately captured. Focused waves also lead to more extreme loads than regular wave loads. This further highlights the need for CFD to predict high-order waves and the hydrodynamic viscous effects. Additionally, tower bending moments and mooring tension forces exhibited dynamic responses at multiple frequencies, correlating with the structure's first-, second-, and higher-order natural frequencies, highlighting the system's nonlinear characteristics.

Aero-hydro-mooring-elastic coupled modeling

Liu et al. [61] first developed an aero hydro mooring coupled model with OpenFOAM using an NWT based on the VoF method, with a sliding mesh technique and fully resolved blades of the NREL 5MW reference turbine mounted on the OC4-DeepCWind semi-submersible floater. Additionally, `MoorDyn` is used for the mooring analysis. The tool was then validated against published data, and coupling effects were shown through a thorough analysis of the platform's motion responses. Specifically, platform responses in surge and pitch drive turbine-wind interactions and downstream vortex formation, affecting aerodynamic thrust and torque variations. The wind turbine's aerodynamic thrust notably displaces the platform further in surge motion. Because of the considerable distance between the system mass center and the turbine rotation, the platform's mean pitch motion is shifted by the turbine's significant pitching moment. The same research team then improved their model [60] by including structural dynamics using a CFD-Multibody-dynamics (MBD) approach to capture the aero-hydro-mooring-elastic behavior of the floating offshore wind turbine. The structural response of the system is calculated using the open-source MBD code MBDyn, handling both rigid and flexible components. The results were then compared with the engineering tool FAST v8. The study highlights the impact of wind turbine aerodynamics with elastic blades on platform responses, mooring dynamics, and turbine performance.

They highlighted that tower interference and platform motions lead to blade deflection and bending moment oscillations, which are crucial for structural design.

Huang, Cheng, and Wan [47] also improved the `FOWT-UALM-SJTU` model to account for elasticity in the blades. The beam model represented the blade structure, and the AL model was modified to account for the induced velocities caused by the platform motions and blade deformations. The results showed that the time-averaged rotor power and thrust decreased due to the blade deformations, whereas the fluctuations were enhanced. The blade bending and deformation are affected by the turbine wake interaction.

2.2. Numerical theory: case of OpenFOAM

2.2.1. Basics of CFD

"the term "computational fluid "dynamics" (CFD) describes a group of techniques that approximate the Euler or Navier-Stokes equations numerically in a discrete domain. In their incompressible form, the latter can be expressed as follows:

$$\begin{gathered}\frac{\partial \mathbf{u}}{\partial t}+\nabla \cdot\left(\mathbf{u}\mathbf{u}^{T}\right)-v\nabla^{2}\mathbf{u}=-\frac{1}{\rho}\nabla p+\mathbf{q}\\ \nabla \cdot \mathbf{u}=0\end{gathered} \tag{2.15}$$

Where q is a source term of general momentum. Turbulence is ultimately caused by the nonlinear convection of momentum, which is the most challenging term in the equations above since they are always three-dimensional, unsteady, and relatively irregular.

Most engineering flows are turbulent, i.e., they carry irregular fluctuating motions that contribute to the transport of momentum, mass, and temperature; they affect the distribution of velocity, temperature, and concentration over the flow field. The motion encompasses a range of eddies of varying sizes. These eddies span from large ones, comparable to the size of the flow domain and associated with low-frequency fluctuations, to much smaller eddies where dissipation occurs, linked to high-frequency fluctuations. This process is described by the Richardson cascade, where energy is transferred from larger to progressively smaller eddies until it is eventually dissipated as heat at the smallest scales. There are various methods for modeling turbulence [94].

Direct Navier-Stokes (DNS). This method resolves all the details of complex turbulent fluctuating motions using the unsteady Navier Stokes equations and the continuity equation without introducing a new model. Since all scales are resolved, the size of the numerical mesh has to be the size at which the heat dissipation appears. Thus, the computational cost increases roughly with Re^3, so DNS is mainly used for fundamental research at small Reynolds numbers.

Large Eddy Simulations (LES) This method only resolves large-scale turbulent motions by solving the time-dependent NS equations; small-scale motions must be accounted for with another subgrid-scale model. One influential model that is frequently used is the Smogorinsky model. This method can be used to solve high Reynolds number flows. However, special treatment has to be done to solve near-wall domains. The computational cost that scales with the Reynolds number squared is a significant downside, prohibiting some analysis.

Unsteady Reynolds averaged Navier Stokes (URANS). Only structures of the mean flow are resolved, while all turbulent fluctuations are modeled. RANS uses the Reynolds decomposition, separating the flow variable into the mean and fluctuating components. Computational costs are lower but still more demanding than those of lower fidelity tools. RANS and LES are based on mathematical constructions with more unknowns than equations. The Reynolds stress tensor is used for RANS to close the Navier Stokes equations. Different turbulence models can be used to compute the Reynolds stresses. Further information on the many existing turbulence models can be found here [86]. Since $k-\omega SST$ models are primarily utilized in floating wind turbine applications, as demonstrated in the upcoming literature study, this thesis will not delve into the specifics of this turbulence model.

LES can calculate unsteady, turbulent flows with large-scale structures and turbulent mixing. In contrast, URANS cannot do so since RANS resolves only the mean flow and slow, unsteady effects. This

is impractical for turbine wake calculations since the flow is highly unsteady; however, literature has proven that RANS has already yielded satisfactory results.

Partial differential equations (PDEs) can be numerically solved with the help of the open-source C++ library OpenFOAM, which stands for Open Source Field Operation and Manipulation. It has powerful multi-physics simulation capabilities. It is extensively employed in computational fluid dynamics, which approximates fluid equations using the finite volume method (FVM). This part will introduce the fundamental FVM formulation and analyze the PIMPLE algorithm to solve for the coupled multiphase flow and rigid body equations, which will be a recurring theme in this thesis.

2.2.2. Finite volume method

The resulting differential equations can be discretized utilizing different methods, the most popular one being the finite volume method (FVM) for its relative ease of implementation and conservative nature. The FVM decomposes the domain into non-overlapping control volumes over which the conservation laws are integrated. Many discrete quadrature and interpolation approximations exist for this purpose, resulting in different truncation errors (numerical diffusion and dispersion) and order of convergence. More details can be found in the book of Moukalled et al. [71]. Several time discretization schemes exist, with explicit methods being less computationally intensive than implicit ones. However, explicit schemes need smaller time steps to ensure stability. An important parameter to measure this stability is the Courant-Friedrichs-Lewy (CFL) number, also called the Courant number. It is defined as :

$$Co = \frac{u\delta_t}{\delta_x} \tag{2.16}$$

The time step size of the simulation is probably the most critical numerical parameter. There are two main methods to define the time step size in OpenFOAM, either by setting a fixed time step value during the whole simulation or by setting the maximum CFL number Co and a maximum time step. In the latter case, the software determines the time step dynamically accordingly. Both methods were used in this thesis. The maximum Co method was used at the earliest stage of this research. However, due to unstable simulation, it has been chosen to decrease the maximum timestep from the previous thesis, which will be discussed in detail in chapter 3.

Numerous techniques are available for solving the discrete system; popular solvers based on pressure-velocity coupling for steady simulations and transient simulations are SIMPLE and PISO. Numerous CFD programs are available, including COMSOL, OpenFOAM, STAR-CCM, Ansys FLUENT/CFX, and OpenFOAM. There are also particular solutions for the pre- and post-processing phases.

2.2.3. Multiphase flow: the Volume of Fluid (VoF) method

These previously introduced concepts are applied in the CFD modeling of floating platforms. The total forces and moments acting on the floating body can be calculated by integrating the pressure loads provided by the CFD solver throughout the surface. Nevertheless, defining a new formulation known as volume of fluid (VOF) is necessary to add a free surface between water and air.

To do so, an indicator scalar field $\alpha \in [0, 1]$ is defined for each cell representing the ratio of the volume occupied by a given phase, with $\alpha = 0$ for gas and $\alpha = 1$ for liquid. Like turbulence, multiphase flows are inherently multi-scale, meaning that a cascade effect operates at various sizes. Giant bubbles formed on the open surface might gradually fragment into smaller formations. The VOF technique can be compared to an LES filter in that smaller structures are averaged while bubbles larger than grid sizes are caught.

The local values of density ρ and dynamic viscosity μ are then reformulated

$$\begin{aligned} \rho &= \alpha\rho_w + (1-\alpha)\rho_a \\ \mu &= \alpha\mu_w + (1-\alpha)\mu_a \end{aligned} \tag{2.17}$$

The VoF method adds a new transport equation to the system :

$$\frac{\partial \alpha}{\partial t} + \nabla \cdot [\mathbf{u}\alpha] + \nabla \cdot [\mathbf{u}_r(1-\alpha)\alpha] = 0 \tag{2.18}$$

, where u_r is the relative velocity between the two phases, expected to and pointing toward the free surface. Functioning as a compression term, it disappears far from the free surface and sharpens it without smearing.

However, it is essential to remember that surface tension effects, dynamic interfaces, small-scale structure interaction, turbulence modeling, phase mixing, and other issues related to multiphase flow provide significant modeling and simulation challenges outside the focus of the present work.

2.2.4. Pressure-velocity coupling algorithms

Pressure-velocity coupling algorithms are used to solve the incompressible Navier-Stokes equations. These algorithms are essential because the pressure and velocity fields are interdependent in incompressible flows. The solution must satisfy both the momentum and continuity equations, ensuring mass conservation. The pressure must be adjusted for incompressible flows to ensure that the velocity field is divergence-free. Several algorithms exist in OpenFOAM; the ones available are PISO, SIMPLE, and PIMPLE.

The SIMPLE algorithm is typically employed in CFD to generate steady-flow solutions. These solutions are directly applicable when flow variables cease fluctuating over time or when a flow reaches a steady state. Additionally, they can mimic somewhat unstable flows, typically at a lesser cost than a more precise transient solution [78].

The PISO (Pressure-Implicit with Splitting of Operator) algorithm, proposed by Issa in 1986, is an efficient pressure-velocity coupling method used in CFD to solve the Navier-Stokes equations. It allows for large time steps and less computational effort than the SIMPLE algorithm. Initially, it works well for unsteady compressible flows and steady-state problems. PISO uses an implicit predictor step followed by a few explicit corrector steps, making it non-iterative while achieving high accuracy [51].

The PIMPLE (PISO + SIMPLE) algorithm is a hybrid pressure-velocity coupling technique. To take advantage of the advantages of both approaches, it integrates elements of the PISO (Pressure-Implicit with Splitting of Operators) and SIMPLE (Semi-Implicit Method for Pressure Linked Equations) algorithms. This combination is beneficial when working with complex, transient, or large-scale simulations, where stability and convergence might be difficult, especially for high Reynolds number flows [74].

2.2.5. Modelling of moving bodies in OpenFOAM: Dynamic mesh methods

Dynamic meshes, or moving meshes, are numerical techniques that allow the computational mesh to change throughout a simulation. These changes can occur due to prescribed motion, flow-induced rigid body motion, fluid-structure interaction, or adaptive mesh refinement. Dynamic meshes are essential in many engineering simulations. For example, they are beneficial for simulating rotary motions, such as turbines or oscillating floaters in waves. While certain behaviors can be simulated without dynamic meshes using workarounds like Multiple Reference Frame (MRF) approaches, dynamic meshes are crucial for specific applications. In OpenFOAM, dynamic meshes can be utilized with various flow phenomena, including incompressible, compressible, and multiphase flows.

Dynamic mesh techniques are generally classified into the following categories:

- **Deformed Mesh (Mesh Morphing):** The mesh is deformed according to the movement of the object of interest.
- **Layering:** Cells are added or removed in the direction of the motion.
- **Sliding Mesh:** Groups of cells move relative to a stationary domain, connected via a sliding interface such as a Cyclic Arbitrary Mesh Interface (AMI).
- **Overset Mesh (Chimera Grids):** Involves cell-to-cell mappings between multiple, disconnected mesh regions to form a composite domain.
- **Adaptive Mesh Refinement:** The mesh is dynamically refined or coarsened during the simulation based on specific criteria.
- **Solid Body Motion:** The entire computational domain undergoes a prescribed motion.

The most used dynamic meshing techniques in the context of FOWT are deformed meshes and overset meshes. They will be briefly compared in the following subsections; more curious readers can refer to

[81] and [96].

Deformed Mesh

Deformed meshes are highly accurate because they operate within a single finite volume domain without requiring interpolation between cell groups. This approach ensures a higher accuracy among the mesh morphing techniques. It is relatively easy to set up, as it does not require particular face or cell zone configurations for coupling regions. However, deformed meshes are limited by their inability to handle large motion amplitudes. Significant body motion can cause nearby cells to deform excessively, leading to zero-volume cells and simulation failures. As a result, robust numerical schemes, linear solvers, and small time steps are necessary when using deformed meshes. This method suits single-body rigid motion problems like ship motion or vortex-induced vibration (VIV). More details on its implementation in OpenFOAM are given in subsection 3.3.4.

Overset Mesh

Overset meshes are the best option for modeling complex motions, including prescribed motions, six-degree-of-freedom (sixDoF) rigid body responses, or combinations. The primary advantage of overset meshes is their ability to handle almost any type of motion, including extremely large amplitudes, without the issues of mesh deformation and numerical instability that affect deformed meshes. Even in cases where bodies are close together and oscillating, overset meshes perform well. They also simplify mesh generation since overset meshes consist of several overlapping cell groups, making it easier to generate individual meshes than to assemble a unified mesh. However, the trade-off for this flexibility is reduced accuracy due to interpolation between overlapping cells, which can lead to less reliable results if not carefully managed with appropriate numerical schemes. It is also computationally more expensive, which is the main reason for choosing the deformed mesh technique.

2.2.6. Numerical wave tank : waves2Foam

This section aims to briefly describe the toolbox's workings without going into too many details. Curious readers can check The `waves2Foam` toolbox is utilized in the upcoming sections of this thesis project: It was created by Niels Gjøl Jacobsen and published in 2012 [52]. It allows for the creation of various wave theories and relaxation zones. Originally written in C++, this practical toolbox was intended to be integrated with OpenFOAM. Many different wave theories are currently included in the toolbox.

The `waveFoam` solver is integrated into the `waves2Foam` toolbox to investigate the interaction and propagation of waves. To account for moving meshes based on the VOF phase fraction technique to capture the free surface, this solver can be combined with the native `interDyMFoam`; the resulting linked solver is called `waveDyMFoam`. The installation procedure can be found in the `waves2Foam` manual. Several scenarios, such as wave loads on coastal bridges, breaking waves on a beach profile, and modeling floating wave energy converters, have validated the `waves2Foam` library.

`waves2Foam` facilitates the incorporation of relaxation zones within the Numerical Wave Tank to prevent undesired reflections. In the present case, an explicit relaxation technique is chosen based on a weighting between the computed solution of the velocity field and the target solution. The explicit approach is given by :

$$\phi = (1 - \omega_r)\phi_{target} + \omega_r \phi_{computed} \tag{2.19}$$

Where $\omega_r \in [0, 1]$ is the weighting function, which can be defined in different ways described in the manual. This method corrects the velocity field u and the phase field α every time step before solving the pressure velocity coupling problem. The exponential weight is chosen in the present study as it is the default choice and has been used in previous literature as well [95].

2.2.7. Turbine dynamics: TurbinesFoam

The `turbinesFoam` library, developed by P. Bachant [4] is an advanced implementation of the actuator line method (ALM) within OpenFOAM, primarily designed for simulating vertical-axis or cross-flow wind turbines. The library has been validated against experimental data and blade-resolved simulations, demonstrating its effectiveness in capturing qualitative near-wake flow features when paired with RANS models and providing a more accurate representation of shed vortices with the Smagorinsky LES model, all while significantly reducing computational costs compared to traditional blade-resolved simulations. `turbinesFoam` incorporates several key features to enhance simulation accuracy, including a dynamic

stall model based on the Leishman–Beddoes approach [58], a Prandtl tip-end correction, and an added mass model to account for the inertial forces on moving actuator elements. The library's structure is modular, with classes like `actuatorLineElement` for fundamental operations, `actuatorLineSource` for generating actuator lines, and `turbineALSource` for defining the turbine as a set of actuator lines. These features allow the library to accurately simulate complex turbine dynamics, including blade rotation and interactions between the turbine's components, while also providing users with flexibility in configuring simulations through adjustable parameters like load distribution, drag-induced wake, and mesh size. More details on the different classes used can be found in the Msc thesis of Pere Frontera Pericàs [81] and Gajjar [35]. The first has extended the library to `Floatingturbinesfoam` to account for prescribed floating motions. In contrast, the latter has coupled the library with an elastic module in Matlab to account for aeroelasticity. It has recently been used by Campaña-Alonso, Ferrer, and Méndez-López [10] to investigate the impact of wake effects from large wind turbines on neiturbines'turbines' power production and aerodynamic loads. The findings reveal significant oscillations in aerodynamic torque and blade loads, with torque variations up to 5.46% and blade root loads experiencing a $\simeq 20\%$ increase and $\simeq 30\%$ decrease due to partial wake conditions.

In turbinesFoam, the way of calculating the smearing factor is the following :

Initially, the code retrieves Gaussian profile coefficients from a dictionary with default values if not explicitly provided. These defaults are: `chordFactor` = 0.25, `dragFactor` = 1.0, and `meshFactor` = 2.0.

The ideal epsilon for lift (ϵ_{Lift}) is computed as:

$$\epsilon_{\text{Lift}} = chordFactor \times chordLength \tag{2.20}$$

Where `chordFactor` is the scaling coefficient and `chordLength` is the chord length of the turbine blade at a specific location.

For drag, the epsilon (ϵ_{Drag}) is calculated using:

$$\epsilon_{\text{Drag}} = \frac{\text{dragFactor} \times \text{dragCoefficient} \times \text{chordLength}}{2}$$

where `dragFactor` is a coefficient related to drag, `dragCoefficient` is the drag coefficient, and `chordLength` is the blade chord length.

Additionally, the epsilon based on mesh resolution (ϵ_{Mesh}) is determined as:

$$\epsilon_{\text{Mesh}} = 2 \times (\text{cellVolume})^{1/3} \times \text{meshFactor}$$

Where `cellVolume` is the volume of the computational cell and `meshFactor` is a scaling factor to account for aspect ratio variations.

The final epsilon value used in the simulation is chosen as the maximum of the threshold value and the mesh-based epsilon:

$$\epsilon = \max(\epsilon_{\text{Threshold}}, \epsilon_{\text{Mesh}})$$

where the threshold value ($\epsilon_{\text{Threshold}}$) is the maximum of ϵ_{Lift} and ϵ_{Drag}:

$$\epsilon_{\text{Threshold}} = \max(\epsilon_{\text{Lift}}, \epsilon_{\text{Drag}})$$

This approach ensures that the smearing factor accurately reflects both the blade's physical characteristics and the local mesh resolution. Using default values for the Gaussian coefficients ensures that the calculations remain robust even when specific parameters are not provided, improving the simulation's precision and flexibility.

2.2.8. Rigid body dynamics: the sixDoFrigidbody solver

The Six-DoF rigid body implementation in OpenFOAM is done through the `sixDoFRigidBodyMotion` library. It allows for the simulation of rigid-body motions, particularly in the context of floating objects. This implementation, as thoroughly detailed in the master's thesis of Pere Frontera Pericàs [81] and

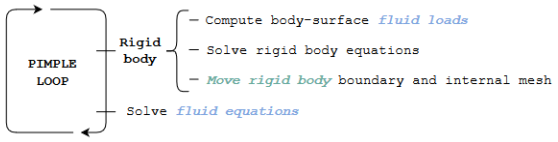

Figure 2.6: Diagram of the coupling of the fluid and rigid body solvers, taken from Pere Frontera Pericàs [81]

work of Limpens, Xu, and Abderrahim [59], integrates closely with dynamic mesh solvers, meaning its parameters are defined within the `dynamicMeshDict` dictionary. This section aims to give general working principles; more information can be found in the references below. Users must specify several key elements to define the body's motion:

- Body properties (mass and moment of inertia),
- Initial conditions (position, velocity, orientation, etc.)
- Constraints (restricting degrees of freedom)
- Restraints (applied loads such as springs or dampers)
- Solver control (selection of time-integrators)
- Output control (logging motion states)

The rigid-body motion in OpenFOAM is approximated using numerical integration methods. External loads are evaluated by computing the force and torque on the body, which are derived from fluid dynamics, including pressure and viscous stresses. To ensure stability, damping coefficients can be specified to prevent sudden jumps in acceleration, which might destabilize the simulation. These will be discussed later in Figure 3.3.5.

OpenFOAM offers two implicit time-integration methods for solving the rigid-body equations: `Newmark-`β and `Crank-Nicolson`. The Newmark-β method is flexible, allowing the user to control the amount of damping and the explicitness of the technique via the parameters β and γ. The Crank-Nicolson method offers similar control simulation stability and accuracy based on the trapezoidal rule. Although an explicit method (symplectic) is available, it is not recommended for fluid-structure interaction (FSI) problems due to its incompatibility with multiple calls within a time step.

Fluid-structure interaction (FSI) in OpenFOAM involves coupling the fluid and rigid-body motion solvers in a partitioned manner. The fluid loads depend on the body's motion and vice versa, which requires iterative sub-steps within the PIMPLE algorithm to reduce partitioning errors and stabilize the simulation. OpenFOAM allows multiple outer-corrector loops, where the rigid-body equations are solved, and the mesh is updated at each iteration, tightening the coupling between fluid and solid domains. This is shown in Figure 2.6.

However, achieving a fully coupled system is impossible in OpenFOAM, as the body motion is not guaranteed to converge along the fluid field. Instead, the number of corrector iterations is usually fixed, and stability is monitored via the mesh-based CFL number. The strongly coupled approach is only compatible with implicit solvers. It can be further stabilized using under-relaxation techniques, although more advanced methods like Aitken under-relaxation are not natively available in OpenFOAM.

3

Hydrodynamic verification of the VolturnUS-S floater

In general, there are three acceptable ways to show the technical feasibility of FOWTs: on-site measurements of full-scale models, numerical analysis through CFD, and scaled model experiments. On-site measurements are expensive to put in place; scaled model experiments can be done but can not reproduce all the coupled behaviors that a full-scale model would have, whereas numerical models can be done at full scale. While Chen, Chen, and Hu [12] reviews and compares three methods for validating the feasibility of floating offshore wind turbines, highlighting full-scale validation importance and addressing advancements and challenges in model testing and real-time hybrid approaches, this thesis focuses on the CFD part.

This chapter focuses on doing a verification study of the VolturnUS-S floater. The analysis focuses solely on the floater geometry, but the mass properties of the entire system (including the floater, tower, nacelle, and rotor) are incorporated unless stated otherwise. It begins with section 3.1, where the floater's characteristics are described, section 3.2 outlines the objectives of verification and validation studies within the context of floating offshore wind turbines (FOWTs). It then details the numerical setup in section 3.3 including sensitivity analysis on some key parameters, followed by a mesh convergence study in section 3.4 conducted for verification purposes. Decay tests are then performed in section 3.6 and compared with results obtained from OpenFAST simulations. Finally, general experimental campaigns are introduced in section 3.7, which can serve as benchmarks for validation studies in further analyses.

3.1. Description of the VolturnUS-S floater

This section summarizes the key characteristics of the floater described in the reference document intended to reproduce in OpenFOAM. The document primarily focuses on simulating a floater with a turbine on top, where the rotor is stalled, and the blades are pitched into the wind to minimize aerodynamic damping. Contrary to OpenFAST, the rotor is not physically present in OpenFOAM, but its mass and inertia characteristics are present.

3.1.1. General characteristics of the floater and its hydrodynamic modeling

The properties of the VolturnUS-S Semisubmersible Platform and the IEA 15MW Turbine mounted on it are detailed in Tables 3.1 and 3.2, respectively. These properties are issued from the definition document [1].

Table 3.1 outlines the general system properties of the IEA 15MW turbine, highlighting a hub height of 150 m and a total system mass of 20,093 t. The turbine is mounted on a semisubmersible platform with a draft and freeboard of 20 m and 15 m, respectively. The mooring system used is a three-line chain catenary. These tables provide a comprehensive overview of the physical and operational specifications for understanding the system's performance and stability.

Table 3.2 lists the platform's characteristics, including a hull displacement of 20,206 m^3 and a vertical center of gravity from SWL at 14.94m. Notably, the platform has a pitch and roll inertia about its center of gravity of 1.251×10^{10} kg·m^2. The geometrical characteristics are summarized in Figure 3.1.

The hydrodynamic modeling in OpenFAST's HydroDyn module integrates a potential flow model with coefficients derived from WAMIT v6. WAMIT computes frequency-dependent parameters such as added mass, wave-radiation damping, hydrostatic restoring, and wave forces using response amplitude operators (RAOs) and quadratic transfer functions (QTFs). This approach accurately simulates how the platform interacts with water waves. A quadratic drag model also accounts for nonlinear viscous effects based on platform velocities, enhancing the model's realism by including fluid viscosity damping. More details on the hydrodynamics modeling can be found in Allen et al. [1].

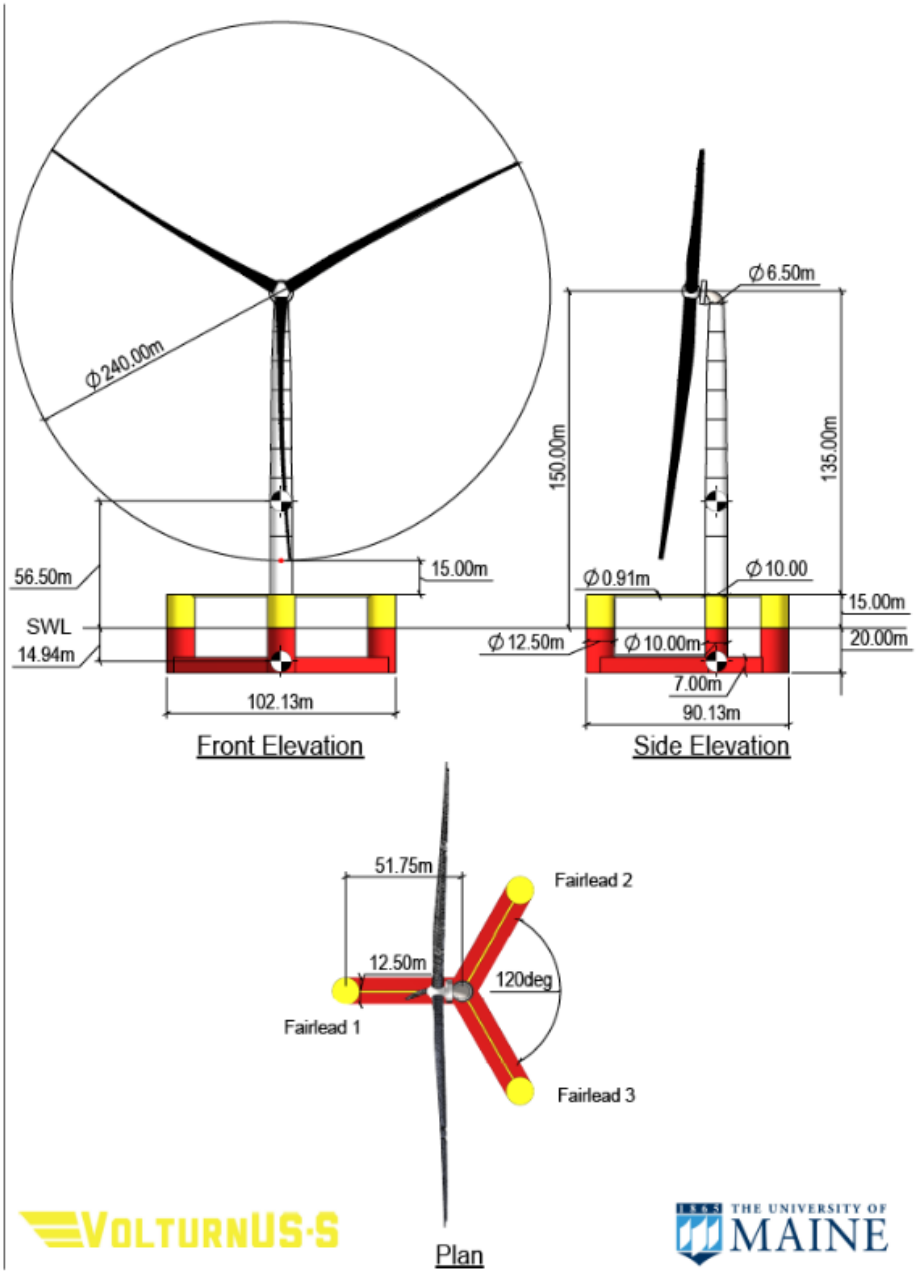

Figure 3.1: General arrangement of the VolturnUS-S floater developed by the University of Maine [1]

Parameter	Units	Value
Turbine Rating	MW	15
Hub Height	m	150
Excursion (Length, Width, Height)	m	90.1, 102.1, 290.0
Platform Type		Semisubmersible
Freeboard	m	15
Draft	m	20
Total System Mass	t	20,093
Platform Mass	t	17,839
Tower Mass	t	1,263
RNA Mass	t	991
Water Depth	m	200
Mooring System		Three-line chain Catenary

Table 3.1: General System Properties of the IEA 15MW Turbine Mounted on the VolturnUS-S Platform

Parameter	Units	Value
Hull Displacement	m^3	20,206
Hull Steel Mass	t	3,914
Tower Interface Mass	t	100
Ballast Mass (Fixed/Fluid)	t	2,540 / 11,300
Draft	m	20
Freeboard	m	15
Vertical Center of Gravity from SWL	m	-14.94
Vertical Center of Buoyancy from SWL	m	-13.63
Pitch/Roll Inertia about Center of Gravity	$kg \cdot m^2$	1.251×10^{10}
Yaw Inertia about Center of Gravity	$kg \cdot m^2$	2.367×10^{10}

Table 3.2: VolturnUS-S Semisubmersible Platform Properties

3.1.2. Mooring system properties

This section details the design of the UMaine VolturnUS-S chain mooring system. The mooring system's properties and inertial/drag properties are provided in Tables 3.3 and 3.4, respectively. The configuration comprises three 850-meter-long chain catenary lines. Each line is connected at the fairlead to one of the platform's three outer columns 14 meters below the SWL. These lines extend radially to anchors, which are spaced 837.60 meters from the tower's centerline and located at a depth of 200 meters, with the anchors positioned at 120-degree intervals in the surge-sway plane. Mooring line drag and added mass coefficients are described on DNV standards and as inputs for `MoorDyn` [41], the mooring line model used within OpenFAST.

Parameter	Units	Value
Mooring System Type	-	Chain Catenary
Line Type	-	R3 Studless Mooring Chain
Line Breaking Strength	kN	22,286
Number of Lines	-	3
Anchor Depth	m	200
Fairlead Depth	m	14
Anchor Radial Spacing	m	837.6
Fairlead Radial Spacing	m	58
Nominal Chain Diameter	mm	185
Dry Line Linear Density	kg/m	685
Extensional Stiffness	MN	3270
Line Unstretched Length	m	850
Fairlead Pretension	kN	2,437
Fairlead Angle from SWL	o	56.4

Table 3.3: Mooring System Properties

Mooring Line Coefficients	Relative to Chain Nominal Diameter	Relative to Volume-Equivalent Diameter
Normal Added Mass	1	0.82
Tangential Added Mass	1	0.27
Normal Drag	2	1.11
Tangential Drag	1.15	0.20

Table 3.4: Mooring Line Drag and Added Mass Coefficients

3.2. Definition of a verification study and methodology

Computational fluid dynamics (CFD) is an engineering tool that must be validated before use. For FOWT, these investigations must be carried out for all the pertinent flow characteristics. This includes, among other things, lift and drag on the wind turbine blades, loads on the structure and deformation of the structure, floater motions, wave propagation, and forces on the mooring line. Burmester, Vaz, and Moctar [8] describe the ingredients for a full elastic aero-hydrodynamic FOWT model with verification and validation techniques, focusing on the hydrodynamics of FOWT. It addresses wave propagation, wave loads, and rigid body motions of a semi-submersible floater. Also, different numerical schemes, turbulence models, and coupling of other tools, such as rigid body motions coupled with mooring lines, should be investigated to gain trust in the CFD models [8]. This section describes what a verification

study is, what they are used for in the context of FOWT, and how to perform them.

3.2.1. Definition of a verification study in the context of FOWTs

The verification study checks whether the equations are solved in the right way. To do so, code verification (correct algorithmic implementation of the solution) and solution verification are required. Solution verification quantifies calculation errors or uncertainties when the exact solution is unknown. Errors, requiring knowledge of the precise solution and having a sign, are distinguished from uncertainties, which define an interval expected to contain the same solution with a specified confidence level and are indicated by a plus-minus sign. Uncertainties are estimated as the absolute value of an error estimator multiplied by a safety factor [27]. Numerical errors of CFD simulations can be further decomposed into round-off errors, which can be neglected with double precision calculations, discretization errors, and iterative errors. The iterative error is unavoidable since nonlinear mathematical equations have to be solved. However, it may also be neglected if it is two to three orders inferior to the discretization error [89]. The latter arises from the approximations of the finite-volume method used to convert the continuous partial differential equations into a system of algebraic equations. In contrast to the other two sources of error, the significance of the discretization error diminishes as the grid and the timestep is refined.

If the SIMPLE algorithm is used, the iterative convergence can be tested by repeating simulations of the same test case with a different amount of SIMPLE iterations per time-step. Then, the momentum equation residuals can be compared for the base case studied in the OC6 Phase 1A work [115]. It can also be reduced by enforcing a stringent convergence criterion during the solving process. Since the PIMPLE algorithm is used for this work, previous work from Scarlatti [98] laid out optimal maximum initial and final pressure residuals. By adjusting the maximum residual values, the accuracy of the final PIMPLE iteration can be increased or decreased. These are taken over in this work. In his thesis, Pere Frontera Pericàs [81] set the number of outer-corrector loops to five, citing it as the minimum required for achieving coupling convergence. Even if the DeepCWind FOWT is used for previous assessment of the iterative error [89][124] [121], it is assumed that it is also minimal for this floater with the residuals chosen. This verification study focuses on minimizing the discretization error and uncertainty. To reduce this error, mesh refinement studies are performed to find a balance between accuracy and computational time. The methodology and theoretical foundation for assessing discretization error through grid refinement studies are extensively covered in Eça and Hoekstra [27] but will be described in subsection 3.2.2. In summary, an evaluation parameter is plotted against the relative step size of the grids. In this study, the ratio of the resolution of the refinement box is used as done in [89].

3.2.2. Description of the methodology

Surge decay simulations were repeated with four different base cells for the refinement zone to estimate the discretization error. Outside the refinement cylinders, the background mesh is unchanged. To maintain the geometric similarity of the mesh as much as possible, the mesh would have to be refined and coarsened globally by adjusting the reference size h. However, in previous works [98][81], the optimal size for the background mesh base cell and the free surface has been found, respectively 4.5m and a refinement of 3, which translates to a cell length within the free surface outside the wave absorption zones of 0.28m $(4.5/2^3 = 0.5625m)$. This validation study's interest is finding the optimal refinement of the refinement cylinders and the size of the cylinders for large surge decay tests.

P-Q analysis

This subsection presents the methodologies used to compute the linear and quadratic damping coefficients and the equivalent linear damping ratio, which are critical metrics for validation from the motion time series. The methodology used is the same as used for the OC6 Phase 1A [115] and is briefly summarized here :

For weakly damped free-decay motions, the amplitude decrease over a half-cycle is defined as $\Delta A_i = A_i - A_{i+1}$, where A_i and A_{i+1} represent the positive amplitudes of the ith peak (trough) at time $t = t_i$ and the immediate next trough (peak) at t_{i+1} in the surge-, heave-, or pitch-motion time series. The mean motion amplitude over the ith half-cycle is approximated as $A_i = \frac{A_i + A_{i+1}}{2}$. The energy loss over

the ith half cycle :

$$L_i = \frac{1}{2}k(A_i^2 - A_{i+1}^2) = \int_{t_i}^{t_{i+1}} (B_1\dot{x}(t)^2 + B_2\dot{x}^2|\dot{x}|)dt, \tag{3.1}$$

where k is the total stiffness of the system for the mode of motion, and $\dot{x}$ is the instantaneous velocity of the floater. Approximating $\dot{x}(t)$ over the ith half-cycle as:

$$\dot{x}(t) \approx \pm\bar{A}_i\omega\sin(\omega(t - t_i)), \tag{3.2}$$

Where ω is the angular frequency, the relation:

$$\frac{\Delta A_i}{\bar{A}_i} = \overline{\Delta A}_i = P + Q\bar{A}_i \tag{3.3}$$

is derived, stating that the normalized amplitude decrease $\overline{\Delta A}$ is linearly related to the mean amplitude $\bar{A}$. The intercept P and slope Q, obtained from linear regression, relate to B_1 and B_2 as follows:

$$B_1 = \frac{2k}{\pi\omega}P \quad \text{and} \quad B_2 = \frac{3k}{4\omega^2}Q \tag{3.4}$$

Since P and Q are proportional to B_1 and B_2, they are used interchangeably for brevity in the rest of the analysis. The relation described in Equation 3.3 generally describes heave and surge motions well; however, due to the surge pitch coupling, which is not taken care of in the P-Q method, the pitch analysis is not adequate for this analysis and results in a poor linear regression as will be shown in section 3.6. However, it can still provide a good characterization, especially compared to OpenFAST.

The equivalent linear damping ratio ζ, which matches the energy loss from the full linear and quadratic damping models with an equivalent linear damping model characterized by damping coefficient B_e, can also be determined from P and Q using the following expression:

$$\zeta = \frac{\omega B_e}{2k} \tag{3.5}$$

Here, ω represents the angular frequency, B_e denotes the damping coefficient of the equivalent linear model, and k represents a relevant stiffness parameter.

Alternatively, ζ can be determined using the logarithmic-decrement method. For consistency with the P-Q method, a damping ratio should be calculated individually for each half-cycle using the logarithmic-decrement method, followed by averaging weighted by A^2.

$$\zeta = \frac{\sum_{i=1}^{N} A_i^2 \cdot \delta_i}{\sum_{i=1}^{N} A_i^2 \cdot 2\pi} \tag{3.6}$$

where δ_i are the half periodic logarithmic decrements defined as $\delta_i = ln(\frac{A_i}{A_{i+1}})$.

P and Q can also be used in the following relationship:

$$\pi\zeta = P + F_A \cdot Q$$

Here, F_A represents the amplitude scaling factor, defined as:

$$F_A = \frac{\sum_{i=m}^{n} \bar{A}_i^3}{\sum_{i=m}^{n} \bar{A}_i^2}$$

Error and uncertainty analysis

In the remainder of this section, a more rigorous estimation of discretization uncertainties for the damping coefficients and ratios is performed using a least-squares approach. This method involves fitting a suitable convergence trend to data from the convergence study and extrapolating the solution to an infinite numerical resolution. The difference between the extrapolated and actual numerical solutions measures the discretization error, which can be used to construct a discretization uncertainty interval.

For any given scalar quantity of interest, ϕ, let ϕ_i be the numerical solution obtained from the simulation with the i-th grid size and time step. The hypothetical numerical solution of ϕ with infinite numerical resolution (i.e., as $\phi \to 0$ is denoted by ϕ_0. The discretization error associated with ϕ_i is defined as $\epsilon_i = \phi_i - \phi_0$ With simultaneous and consistent refinement of cell size and time step, the convergence error ϵ_i can be assumed to follow the standard power-law error estimator (Richardson extrapolation) [27]

$$\epsilon_i = \alpha \lambda_i^p \tag{3.7}$$

,where λ_i is the refinement ration associated with the ith grid. At a minimum, three grids are necessary to solve for the constant coefficient α, the apparent order of convergence p, and the value ϕ_0 using the least square minimization.

However, error estimation based on three (or two) grids is unreliable for noisy data due to the extreme sensitivity of the determination of p to scatter in the data [27]. Therefore, it is nearly impossible to determine whether a given data set is in the ”asymptotic range.” Moreover, a single grid triplet provides only one instance of p. Redundancy, and thus the possibility of a quality check on the value of p, occurs only when a fourth grid is added. Therefore, using at least four grids when some scatter in the data is expected is highly recommended, as is common in most engineering flow problems. This leads to solving the following equation :

$$\sigma = \sqrt{\frac{\sum_{i=1}^{N} \left[\phi_i - (\phi_0 + \alpha \lambda_i^p)\right]^2}{N - 3}} \tag{3.8}$$

The minimized value of σ indicates how well the convergence aligns with the assumed trend in Equation 3.7. If σ is too large, the error estimate should be deemed invalid, necessitating an alternative approach. Conversely, if σ is small and the apparent order of convergence falls within the range $0.95 < p < 2.05$ (assuming formally second-order schemes), a corresponding discretization uncertainty can be developed based on the estimated discretization error, ϵ_i, using an appropriate safety factor, F_s

$$U_i = F_s \cdot |e_i| + \sigma \tag{3.9}$$

If the apparent order of convergence from the least-squares fit exceeds the theoretical order of 2 (i.e., $p > 2.05$), the error estimates might be overly conservative. In such cases, p is set to 2 for the least-squares fit, and an additional lower bound of $F_S \cdot \Delta_M$ is imposed on the discretization uncertainty, where Δ_M is the range of ϕ_i across all cell sizes and time steps investigated. If s is small, the commonly used safety factor value of $FS = 1.25$ from the literature can be applied.

OC6 Phase Ia: findings of the P-Q analysis on a scaled DeepCWind floater

As part of the OC6 Phase Ia project, a collaborative effort was undertaken to verify and validate CFD simulations of the free-decay motion of the DeepCwind offshore wind semisubmersible platform. The CFD simulations are validated using measurements from a new experimental campaign designed to minimize uncertainties and address the hydrodynamic problem better. This campaign utilized a simplified linear taut-spring mooring system instead of the catenary mooring system used in the previous project, which had often been seen as a significant challenge in achieving successful validation [115]. The linear-spring mooring setup was created to provide nearly accurate natural periods of floater motion while significantly reducing the complexities and uncertainties involved in numerically modeling the mooring lines. The study focused on three critical load cases: free-decay motion in surge, heave, and pitch. Multiple organizations contributed CFD results for one or more of these load cases, which were then compared against experimental data collected during the OC6 Phase Ia campaign. The motion

periods, linear and quadratic damping coefficients, and equivalent linear damping ratios were derived from the experimental and numerical time series of the floater's motion using the P-Q analysis method, serving as validation metrics.

The analysis reveals that despite using a fine mesh and a small time step, discretization uncertainty remains significant, especially for the linear and quadratic damping coefficients, with grid resolution being the primary source of error. Temporal discretization and iterative errors are secondary contributors, with turbulence model uncertainties having minimal impact. Notably, the linear and quadratic damping coefficients exhibit opposite trends as the simulation is refined, leading to a consistent equivalent linear damping ratio across simulations. Thus, the equivalent linear damping ratio is the most reliable metric for tuning mid-fidelity models, though it does not differentiate between linear and quadratic damping components.

The findings highlight key characteristics of hydrodynamic damping for the DeepCwind semisubmersible. In all load cases (surge, heave, and pitch), wave radiation damping is negligible due to low natural frequencies. Heave and pitch damping are predominantly quadratic, likely from a drag on the heave plates. In contrast, surge damping shows linear and quadratic contributions, especially at low Keulegan-Carpenter (KC) numbers.

These insights are crucial for developing mid-fidelity engineering models. Quadratic damping can be accurately modeled with empirical drag forces for heave and pitch. However, traditional Morison equations lacking a linear drag term are insufficient for surge. Adding a linear term is necessary to capture surge damping accurately. This tuning is essential for accurately predicting free-decay motion, especially in the early design stages when floater designs often change.

3.3. Numerical setup

The case must be adequately set up to perform the simulations correctly. This section presents the parameters chosen for the simulations and compares them to the literature. The main goal is to have proper simulation parameters to perform an extensive surge decay test, which is the most dominant movement for harsh conditions. Indeed, large movements are expected to have the most significant discrepancy with the relevant engineering models, which is one of the reasons for performing CFD simulations.

In this work, no comparison with experimental campaigns is expected, as will be elaborated on in section 3.7; the latter have too essential uncertainties in the moorings for the First Comparative study or do not consider hydrodynamic loads only for the FOCAL campaign.

3.3.1. Characteristics of the simulation domain

A conservative approach was chosen to make the dimensions of the simulated domain exclude any boundary effects on the simulation. Usually, the driving design parameter is the wavelength of the design case, as shown in [98] [81] [95]. In the present case, no waves are simulated; it was chosen that the dimensions would be floater width-dependent. Literature suggests the domain should be at least 4-5 floater widths [98]. In the present case, six floater widths are chosen since the tested movement of the floater is expected to be significant. This is consistent with the recommended domain lengths of the OC7 campaign, which will be later described in section 3.7. The water depth is set to 200m since the anchors are placed at that depth in the general case described in the reference file [1]. The air height is 100m to perform an efficient dynamic meshing. Additionally, wave absorption zones are placed in the surge direction with the `waves2foam` toolbox to absorb radiated waves and simulate eventual waves later. Finally, a mesh grading is applied towards the boundaries to lower the number of cells used in the simulations, on which a sensitivity study has been done in the work of Scarlatti [98]. As described in the previous work of Pere Frontera Pericàs [81], the following boundary conditions are laid out in Table 3.5.

3.3.2. Numerical mooring setup

The moorings are consistent with the reference file, and additional constants were found in the `MoorDyn` input file, which the IEA task uses to perform simulations of the VolturnUS-S floater. In the present case, the mooring cables are discretized into 20 finite elements of 5th order, and `Moody` uses an explicit 3rd

	α	P_{rgh}	U
Inlet	zeroGradient	fixedFluxPressure	zeroGradient
Outlet	zeroGradient	fixedFluxPressure	fixedValue 0
Bottom	zeroGradient	fixedFluxPressure	fixedValue 0
Atmosphere	inletOutlet	total pressure	pressureInletOutletVelocity
Front / Back	empty	empty	empty

Table 3.5: Boundary conditions for the volume fraction, modified pressure, and velocity.

order Runge-Kutta scheme with a CFL number of 0.9 to integrate in time. Twenty elements to describe the mooring line are enough to explain the mooring dynamics [77][30]. Eskilsson even suggested that ten elements are enough and would decrease simulation time, but since they used an evolved version of `Moody`, 20 points were kept. Additionally, ten extra quadrature points were added to increase ground contact performance [98].

3.3.3. Refinement around the floater

Using the work of Scarlatti [98] and Pere Frontera Pericàs [81], the base element for the mesh is 4.5m, and the mesh is graded towards its boundaries as described in the previous work, which was based on literature [95]. Since decay tests are simulated, the base cell is cubic, and the aspect ratio of the base cell is 1. Using `snappyhexmesh`, the surface around the mean water level (+/- 4m) is refined at level 3 and level 2 in the wave absorption zones. The surface of the floater is refined at level 3 as well, as it has been done previously. The size and refinement of the zones around the floater are exciting, as they are essential for accurately modeling the hydrodynamic loads. These will be described in more detail in the mesh refinement study. All the other parameters can be found in `snappyHexMeshDict`.

3.3.4. Use of the dynamic mesh morphing technique

All the definitions regarding dynamic mesh capabilities in OpenFOAM are defined in `dynamicMeshDict`. The current implementation uses the `sixDoFRigidBodyMotion` solver. It applies a spherical linear interpolation (SLERP) of movement as a distance function to the object surface [81]. The body motion can be mapped onto the mesh using different diffusivity models. A common approach for rigid bodies is the inverse distance model, where the mesh morphing decreases with distance from the body. Users can use the innerDistance and outerDistance entries to constrain the mesh deformation between these two distances, usually measured by the body wall. The inner distance typically corresponds to the boundary layer thickness, while the outer distance is selected based on the minimum distance to the nearest domain boundary [77]. New boundary conditions for the mesh motions should be defined; those are extensively described in the previous work and summarized in Table 3.6.

Patch	**Boundary Condition**	**Type**
All Fixed Patches	Mesh Motion	zero
Body Patch	Mesh Motion	calculated
Body Patch	Velocity	movingWallVelocity
Body Patch	Pressure	fixedFluxPressure

Table 3.6: Boundary conditions for dynamic meshes

By default, the `waves2foam` solver is not compatible with dynamic meshes. However, the author's manual can provide a brief guide on integrating it. A new separate solver named `waveDyMFoam` is thus created. A guide will be added on how to install the simulation setup.

Large motions, however, are challenging for deforming meshes since they deteriorate mesh quality and, thus, numerical stability. Overset techniques remain the most versatile and robust tool for managing large motions across multiple degrees of freedom [23]. Overset meshes can introduce numerical diffusion and increase computational costs due to the non-conservative nature of grid interpolation. While this method effectively handles large mesh motions without compromising mesh quality, it demands careful planning and expertise. Future work could focus on implementing a setup using the overset meshing technique; due to time constraints, the dynamic mesh morphing technique is deemed good

enough.

3.3.5. Six-DoF rigid body

As seen in the previous section, the rigid body motion is closely related to the choice of the dynamic mesh method. The inputs and methods are extensively described in the master's thesis of Pere Frontera Pericàs [81].

Inclusion of the Rotor Nacelle Assembly + tower (RNA+) mass

Since it was not clear whether the mass of the RNA+ was included in the simulations of the definition file, tests have been done with a very coarse mesh to assess this.

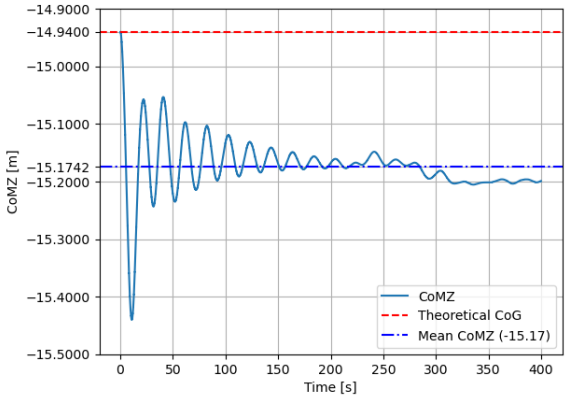

Figure 3.2: Heave position of the center of rotation of the VolturnUS-S floater with the mass of the IEA 15MW wind turbine on top, the center of rotation and the center of gravity coincide.

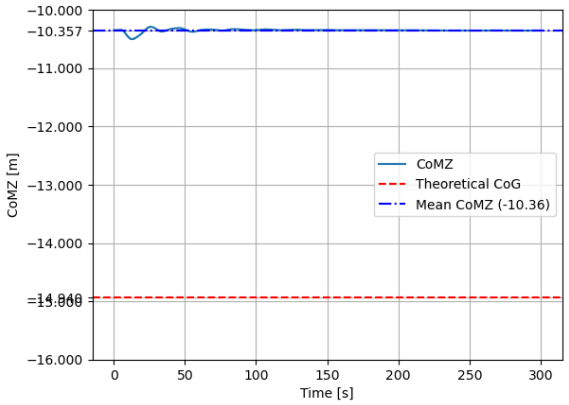

Figure 3.3: Heave position of the Center of Rotation of the VolturnUS-S floater without the mass of the IEA 15MW wind turbine on top

When simulating the floater alone, the center of rotation, which coincides with the center of gravity in this simulation, is positioned higher and differs from the equilibrium center of gravity specified in the reference document. Notably, setting the initial center of gravity of the floater at 14.94 meters results in the simulation crashing after a few seconds, despite the mass of the floater not including the RNA. It is assumed that this is due to the sudden acceleration of the floater that the simulation setup can not cope with. This shows that the characteristics in the tables 3.2 and 3.1 assume a tower on the floater. It is essential to highlight the definition of the STL file and the mooring positions. The current STL file was provided by IEA Task 30, but users must adjust the positioning themselves. Blender has been utilized for this purpose and is recommended mainly because it includes a utility called SnappyHexMeshGUI. This utility generates a template for SnappyHexMesh dictionaries, which can help new users of OpenFOAM understand how Snappyhexmeshmesh works. More details can be found in the guide.

Acceleration-relaxation

In this subsection, we highlight the significance of employing under-relaxation techniques to enhance simulation stability, controlled by the `accelerationRelaxation` keyword, which adjusts the under-relaxation coefficient Φ:

$$\ddot{\mathbf{x}} = \ddot{\mathbf{x}}^{\text{old}} + \phi \left(\ddot{\mathbf{x}}^{\text{new}} - \ddot{\mathbf{x}}^{\text{old}} \right) \tag{3.10}$$

With Φ decreasing, the stability of the numerical scheme is increasing at the price of slower convergence. However, a low value means the body does not respond to the fluid forces correctly. Recommended values are in the range of 0.9-1.

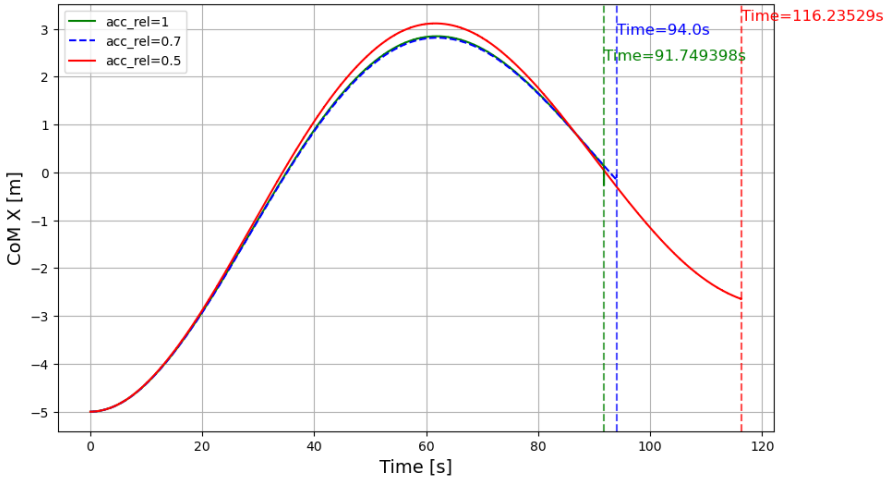

Figure 3.4: Surge decay tests with varying acceleration relaxation parameter using a coarse mesh

As shown in Figure 3.4, the `accelerationRelaxation` factor influences the floater's motion and the simulation's numerical stability. A too-small value seems to lead to higher amplitudes and lower damping, even though it provides better stability, although it still crashes after some time. In both cases, the timestep decreases very rapidly after the k or ω values (in the k-ω SST model) are bounded, eventually reaching 10^{-60} seconds before the simulation crashes. This is coherent with the fact that the Courant number (Co) becomes excessively high after a certain point, leading to instability in the simulation and causing it to stagnate and fail. To avoid losing accuracy, keeping the acceleration relaxation factor high and decreasing the maximum timestep to increase stability is better. Unless stated otherwise, the acceleration relaxation factor is set to 1 for this work.

3.3.6. Choice of the numerical timestep

Two different approaches can be used to choose the timestep. The timestep can be set dynamically to have an optimized timestep so that the maximum Courant number is close to the threshold. It offers flexibility and can be more efficient, potentially reducing the numerical cost by saving some timesteps. However, it is possible that there is a computational overhead to monitor the Courant number over the simulation, and there is a risk of instability if the adaptive algorithm is not calibrated. In OpenFOAM, it is also possible to add a maximum timestep so that it does not increase too much and the Courant number stays below the threshold. A fixed timestep can also be used; it provides more stability and predictability. However, it may lead to inefficiencies if the timestep is not optimal for all simulation conditions. Similarly, using small timesteps may lead to inefficiencies if the chosen timestep is smaller than necessary to capture fast-changing phenomena accurately. These are realistic thanks to simulations that have been done.

At first, the time step was set to change dynamically to optimize, which was successfully done for the first refinement study. However, for the second study, the simulation became unstable, and it was decided to keep the simulation time constant to maintain stability.

3.4. Verification study: grid convergence

This section aims to perform the verification study on the VolturnUS-S Floater. The study focuses on two parameters: the refinement level around the floater and the sizes of the refinement zones. The parameters that were described above were all fixed and taken either from literature or from the previous work that has been done by Scarlatti [98] and Pere Frontera Pericàs [81]. However, since the floater and the motions considered differ, a different refinement and refinement zone around the floater should capture more significant motions while keeping the cell count small enough. Instead of using a refined sphere around the initial position that would leave the upper and lower slice of the sphere unused, this model setup aims to use concentric elliptic cylinders that are larger in the surge motion, which is the dominant displacement compared to sway. Two concentric cylinders with different radii and refinement

levels are used to diminish the cell count. This mesh convergence study is divided into two parts: first, it will assess how refined the cylinders should be, and second, how big these cylinders should be.

3.4.1. Part 0: Equilibrium position of the floater

This subsection aims to determine the equilibrium position of the floater so that the results can be post-processed accurately. The fine mesh, described in Table 3.8, is used for this purpose. The simulation is run for 300s, and the equilibrium position is defined as the average over the whole simulation. The results are given in Table 3.7.

Surge [m]	Sway [m]	Heave [m]	Roll [deg]	Pitch [deg]	Yaw [deg]
-2.57E-02	9.37E-05	-10.13	3.86E-04	7.03E-05	-1.39E-04

Table 3.7: Equilibrium position of the floater without the tower mass

3.4.2. Part 1: Refinement of the cylinders

For this first part, the refinement levels of the cylinders are changed. The size of the cylinders is chosen so that the refinement cylinder does not deform too much with the large motions of the floater, which are intended to be captured accurately. The floater is located inside the inner cylinder. From Wang et al. [115], it has been decided to leave buffer space underneath the floater since, for the DeepCWind floater, the flow separation near the heave plates contributes to the surge damping. A 5m surge decay test is performed. The simulation parameters are in Table 3.8.

Mesh size	Extra fine	Fine	Medium	Coarse
Inner cylinder dimensions (a*b*h) [m]	65*65*20	65*65*20	65*65*20	65*65*20
Outer cylinder dimensions (a*b*h) [m]	90*75*40	90*75*40	90*75*40	90*75*40
Inner cylinder refinement [-]	5	4	3	2
Outer cylinder refinement [-]	4	3	2	1
Number of cells [-]	11685580	11222796	8173768	6221020
Refinement ratio [-]	2	1	0.5	0.25

Table 3.8: Parameters for the first part of the mesh convergence study

The maximum dt is set to 0.05s to ensure stability with the previous tests, while the maximum Courant number is set to 0.5. From Scarlatti [98], it has been concluded that the equivalent medium case is a good match for this sort of decay test for the DeepCWind Floater. A further increase in the refinement leads to additional computational time and a limited change in the decay. The then chosen refinement is used for this work as a base case and corresponds to the medium case described in Table 3.8.

The results are displayed in Figure 3.5. Notably, the extra fine mesh appears to be of poorer quality than the fine and medium mesh, with its positions aligning more closely with the coarse mesh.

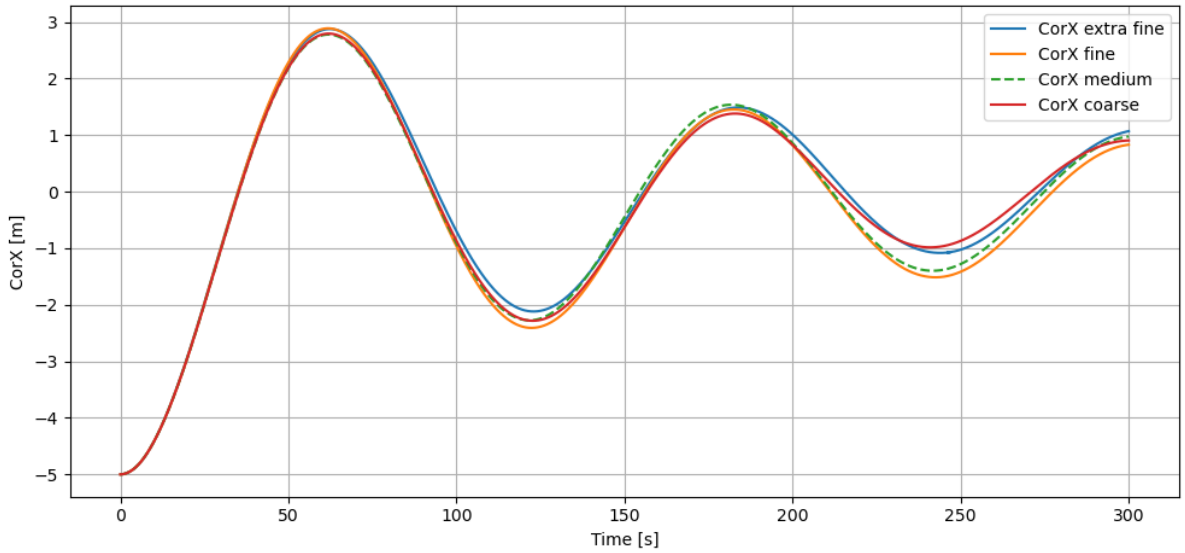

Figure 3.5: Surge decay tests for the first refinement study, where the grid is progressively refined

Figure 3.6a and Figure 3.6c show that the maximum courant number is always lower than 0.5 as expected. One could say that the maximum timestep could be increased to save simulation time since this threshold is reached for most of the simulation. However, one can see in Figure 3.6c that the Courant number almost reaches 0.5 and that the timestep had to be reduced to cope with the Courant criteria. It can be noted that the maximum occurs when the velocity of the floater is the highest. Also, when the maximum timestep was increased too much, the simulation became unstable. It is thought to be due to the adaptive timestep. When going through the log file, when the Courant number became too important, either k or ω were bounded, which most of the time then led to an exponential decrease of the timesteps. The maximum timestep of 0.05s was found through the trial and error method, and since it worked for the fine mesh, it also worked for the coarser meshes. This trial and error method is not very rigorous and complex to implement for simulations with long computational times, so it has been decided to proceed with constant timesteps for the rest of the studies. These would be optimized depending on the movements simulated to comply with the criterion $Co < 0.5$ As shown in Figure 3.6d, the maximum Courant numbers for the extra fine mesh are limited to $Co = 0.5$, and dynamic time-stepping occurs, unlike the other simulations where maximum Courant numbers hover around $Co = 0.1$. Despite the mean Courant number in the domain being consistently lower, the higher maximum Courant numbers in the extra fine mesh might account for its reduced simulation fidelity compared to the fine mesh. The additional fine mesh simulation ran for eight days on 160 cores. Visually, the medium mesh closely resembles the fine mesh, while the coarse mesh fails to capture the movement accurately compared to the fine mesh.

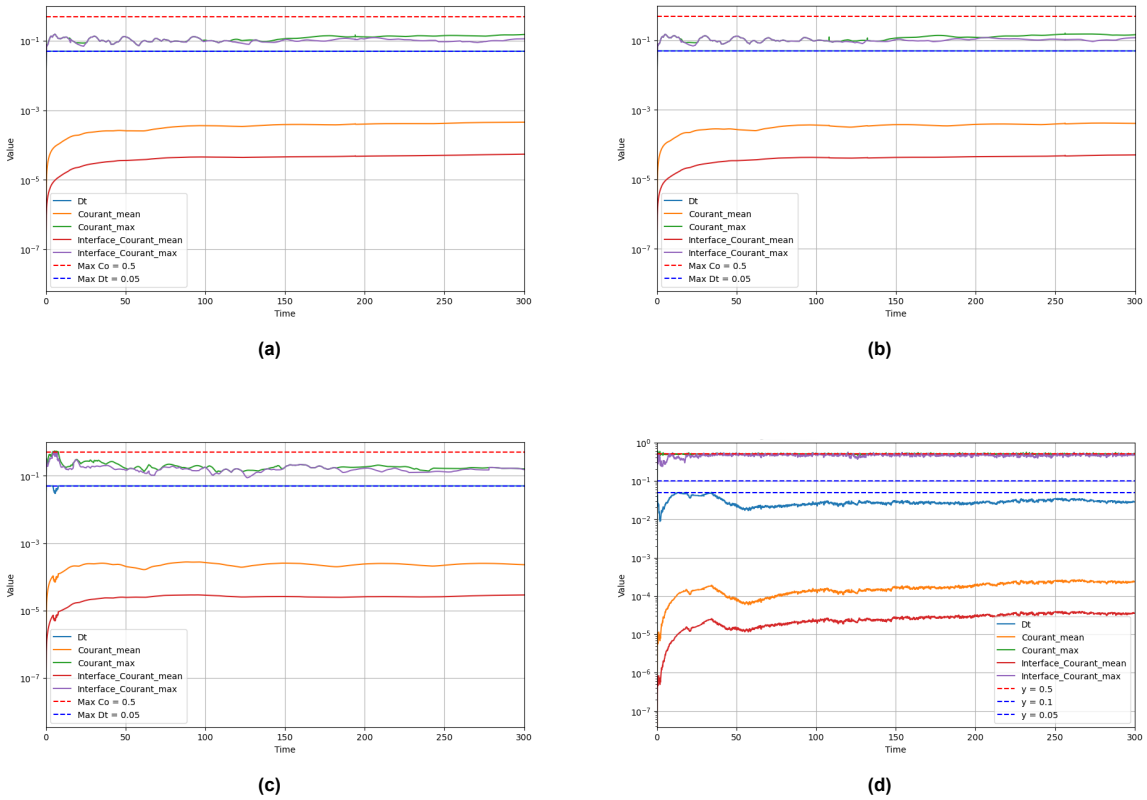

Figure 3.6: Time dependent variables, for adaptative timesteps with maxDt = 0.05 and maxCo = 0.5 for a coarse (a), medium (b), fine (c) and extra fine mesh (d).

Key parameters are evaluated and compared to the fine mesh in Table 3.9. Since the mass of the Rotor Nacelle Assembly was not included in this part of the study, the damping coefficients resulting from this study should not be used to compare with OpenFAST simulations done later in section 3.6. One can see that the amplitude comparison shown in Table 3.10 is not a strong indicator for comparing the grids. The first minima, i.e., the second extrema, is very similar apart from The errors in P and Q seem more important than the errors in ζ.

First, all simulations were run for less than three surge periods, which led to a small number of amplitude peaks to analyze. There is an essential sensitivity on the P, Q, and ζ values as shown in Table 3.9. Additionally, the low R^2 values corresponding to the linear regression to determine P and Q show the results' sensitivity and uncertainties (Table 3.10). Additionally, the equilibrium position subtracted from the raw data is also a source of uncertainty and could be mesh-dependent. Another source of uncertainty comes from the extra exemplary case. It breaks the trends shown with the increased refinement and can be further seen in Figure 3.7. One reason could be the high Courant number, leading to noncomparable results. This is why all the cases are compared to the exemplary case, which is meant to be the baseline of comparison.

Case	Q **[1/m]**	Q **abs. diff [1/m]**	P **[-]**	P **abs. diff [-]**	ζ **[%]**	ζ **rel.diff [%]**
Extra fine	-0.0231	0.15	0.375	0.41	5.24	22.57%
Fine	0.0126	0.00	-0.036	N/A	0.0052	N/A
Medium	0.0654	0.06	0.107	0.14	4.02	-6.03%
Coarse	-0.117	0.24	0.570	0.61	5.22	21.99%

Table 3.9: Results of the P-Q analysis for the first refinement study

Further performing the uncertainty analysis, as described in subsection 3.2.2, shows quantitatively how uncertain the values are. When optimizing for p, α, and Φ_0, the apparent order of convergence is smaller than 0.95. The causes for that are the same as explained above. Assuming for plotting purposes that

Case	R^2 [-]	A_1 [m]	A_1 rel.diff [%]
Extra fine	0.76	-1.85	-13.57%
Fine	0.04	-2.14	N/A
Medium	0.11	-2.01	-6.26%
Coarse	0.40	-2.01	-5.88%

Table 3.10: Results of the amplitude analysis for the first refinement study

the order of convergence is two since we assume second-order schemes, the results of the uncertainty analysis are shown in Figure 3.7 and the values are given in Table 3.11. The uncertainties are presented in absolute values since the values are scattered and near 0.

Case	P [-]	Uncertainty P [-]	Q [1/m]	Uncertainty Q [1/m]	ζ	Uncertainty ζ
Extra fine	0.3750	$\pm$0.6487	-0.0231	$\pm$0.2342	5.24	$\pm$1.9107
Fine	-0.0361	$\pm$0.5521	0.1260	$\pm$0.2018	4.28	$\pm$1.3313
Medium	0.1070	$\pm$0.4718	0.0654	$\pm$0.1673	4.02	$\pm$1.7857
Coarse	0.5700	$\pm$0.3752	-0.1170	$\pm$0.1349	5.22	$\pm$1.2063

Table 3.11: Discretization uncertainty of key damping parameters

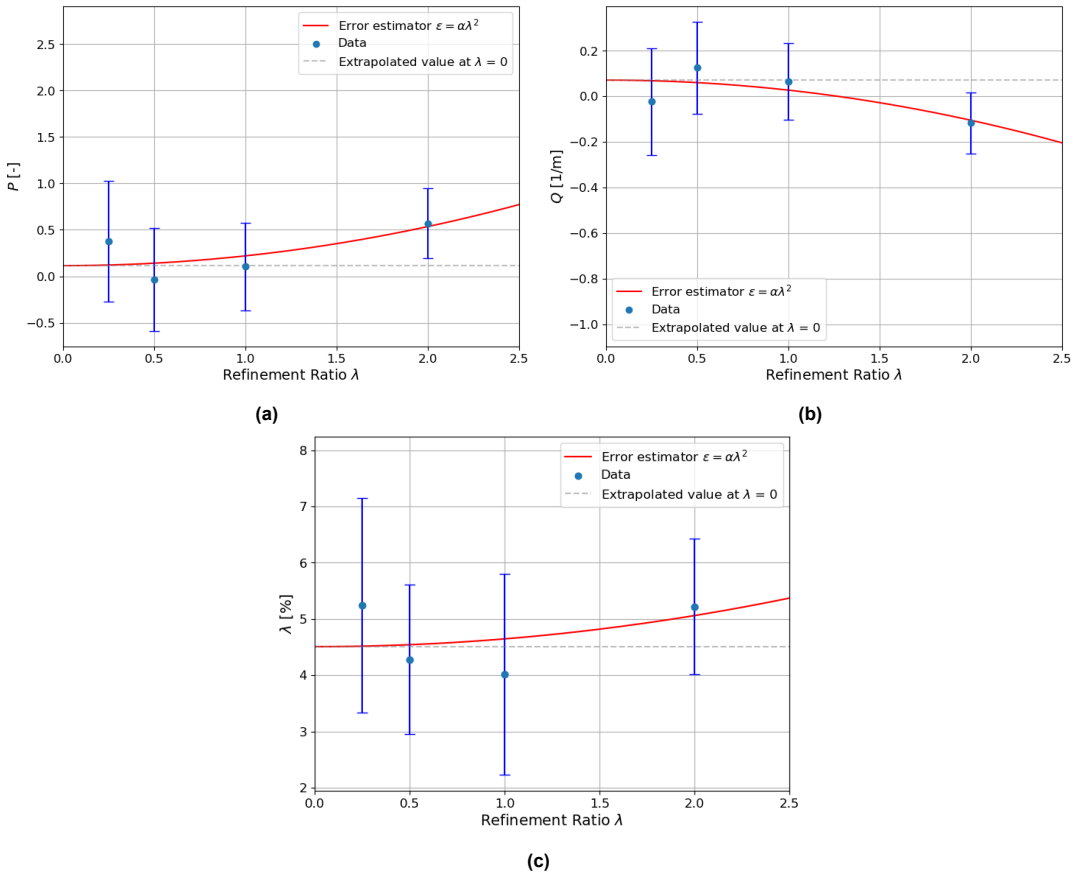

Figure 3.7: Convergence of the linear damping coefficient, quadratic damping coefficient and equivalent damping ratio in surge with different grid refinements in a, b and c respectively. The dots are the CFD solutions computed for four different refinement ratios as detailed in Table 3.8. The estimated discretization uncertainties are depicted as symmetric uncertainty bands attached to the dots

The Figure 3.7 further shows the extra fine mesh is out-of-line. The increasing trend of P and λ with the refinement and the decreasing trend of Q are coherent with the analysis done by Wang et al. [115] during OC6 Phase 1A. Significant uncertainties are found for the linear and quadratic damping, whereas interestingly, the equivalent linear damping has fewer uncertainties. Notably, the decrease in P is nearly

offset by the increase in Q with refinement, leading to a more stable equivalent linear damping. This trend has also been observed in [115].

It has not been deemed useful to calculate the uncertainties by multiplying the variable range by a safety factor, as that would give even larger uncertainties, as the range in refinement ratios is very large compared to other similar studies.

In conclusion, these results are interesting in comparing the grids and noticing their differences analytically. They also show how uncertainties can be reduced, mainly through simulating for longer times, and what factors come into play. As will be seen later in the chapter, future work could try to implement the finding of the equilibrium position and see if the uncertainties could be reduced using this technique. Despite the significant uncertainties remaining from the P-Q analysis, which is post-processing intensive, the medium mesh refinement is selected as the most computationally efficient option, providing results close to those of the fine mesh.

3.4.3. Part 2: Size of the cylinders

This second part of the refinement study aims to indicate the size of the refinement zone around the floater. Since the thesis's initial goal is to simulate large motions with a dynamic mesh morphing technique at reduced computational cost, the size of the refinement zones around the cylinders has to be increased compared to the first refinement study. Some grids will be excluded from the second refinement study by showing the instability of 30m decay tests. This central part of the second refinement study will perform a large decay test of 15m, which is the amplitude that can be expected for harsh conditions and which is close to the movement amplitude that the floater can have in focused wave conditions [87]. In the second phase, an auxiliary set of surge decay tests will be conducted using a 24m amplitude corresponding to the initial amplitude used during the Plymouth campaign. This will assess the validity of extending the decay offset to support the refinement study. It has to be noted that even though the first part of the refinement study did not perform the same decay test due to time constraints, the result obtained in part 1 is still valid since the refinement of the floater is relevant to judging the accuracy of the hydrodynamic loads. The first tries were done; however, the adaptive timestep setting was proven to be unstable. Thus, it was decided to go towards a fixed timestep that is small enough to keep the Courant number below 0.5 at all times if possible.

Analytically speaking, a P-Q analysis was done, together with a relative comparison of the first amplitude peaks.

Equilibrium position of the floater

The tower's mass was included in the second part of the refinement study, resulting in a new equilibrium position. However, after the simulations were completed, an issue with the origin point of the STL files for the floater was identified, causing an anomaly in the sway direction. Despite this, it is believed that the anomaly does not impact the conclusions of the refinement study, as sway is not the movement of interest. However, the values obtained from the P-Q analysis should not be used for comparison purposes without considering this error.

Surge [m]	Sway [m]	Heave [m]	Roll [deg]	Pitch [deg]	Yaw [deg]
-2.34E-02	2.58E-01	-15.06	5.42E-01	-1.89E-03	2.24E-02

Table 3.12: Equilibrium position of the floater with the tower mass and sway mistake

The error explains why the roll and sway values deviate from 0 despite theoretically being expected to be near zero. Additionally, the heave equilibrium position differs slightly from the reference document's. This discrepancy is likely due to differences in the mooring simulation.

Surge decay test with 30m offset, unstable for coarser meshes

A high amplitude decay test was performed to test the robustness of the chosen refinement. In Table 3.13 are indicated the sizes of the cylinders used in this set of tests :

For coarse and medium coarse refinement levels, it has been found that the simulations are unstable for high-offset decay tests at 30m, which is why they are excluded from the 15m-surge decay tests, which will make the second refinement study. In both cases, the maximum Courant number of the air-water

	Dimensions [m]	Refinement Levels				
		Coarse	**Medium-Coarse**	**Medium**	**Fine**	**Extra Fine**
Inner Cylinder	Length	65	80	90	100	110
	Width	65	65	65	65	65
	Height	40	40	40	40	40
Outer Cylinder	Length	90	110	120	130	140
	Width	75	75	75	75	75
	Height	20	20	20	20	20

Table 3.13: Dimensions for different refinement levels

interface increases exponentially until it diverges, as seen in Figure 3.8. The simulations are stable for the medium and fine meshes, despite the usual peak for the fine mesh, as seen in Figure 3.9. This is probably due to the mesh quality, which undergoes a significant deformation at high speed, 65 seconds being half a period, where the velocity of the floater is maximum. This also highlights the limitation of dynamic meshing for high amplitude decay tests. Detailed reasons for the simulation's instability are out of this thesis's scope.

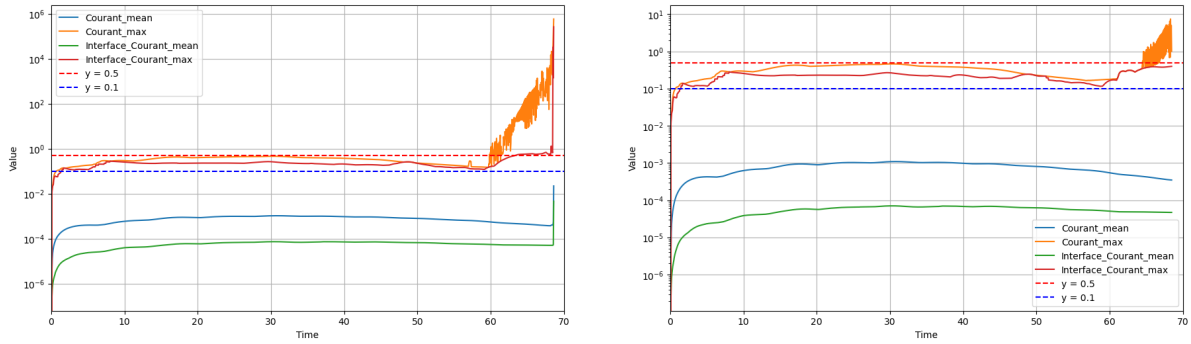

(a) **(b)**

Figure 3.8: Comparison of 30m-surge decay tests for coarse and medium-coarse mesh in a and b respectively. Unstable results are found.

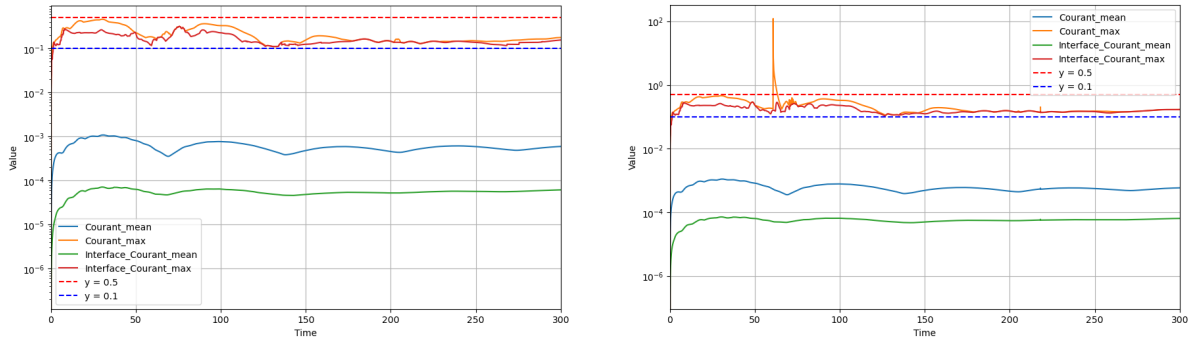

(a) **(b)**

Figure 3.9: Comparison of 30m-surge decay tests for medium and fine mesh as shown in a and b respectively. The results are stable.

Surge decay test with 15m offset

Following these results, the second phase of the refinement study is conducted. A 15m surge decay test is performed with the cylinders placed at the initial position to facilitate dynamic meshing. Placing the refinement cylinders at the equilibrium position around the origin would reduce simulation precision,

as it would no longer refine the flow around the floater, which dynamically deforms the mesh with its movement.

As illustrated in Figure 3.10, the surge movements of the fine and extra fine meshes, defined in Table 3.13, show good agreement. In contrast, the medium mesh diverges from the reference extra fine mesh after approximately two surge periods. All simulations are stable, maintaining Courant numbers well below 0.5, as shown in Figure 3.12. This criterion ensures simulation stability; doubling the timestep would still meet the criterion, potentially halving the simulation time as discussed in subsection 3.3.6.

Furthermore, simulations have been extended from the 300s to 450s to investigate if the fine mesh also diverges at later times. From Figure 3.11, differences in oscillatory periods between the fine and medium meshes can be observed, with varying amplitudes occurring at different times. These differences diminish over time due to the decaying motion of the floater.

The results of a quantitative P-Q analysis are given in Table 3.14 and Table 3.15. The strongly post-processed variables P and Q differ significantly with the size of the refinement zones, highlighting the sensibility of such an analysis despite close positions between the extra fine and the fine mesh. It can be seen from the P, Q, and ζ values that the fine mesh is good enough to capture the movement and the loads of the floater. From the R values of the linear regression, one can see that the added points of the decay test improve the quality of the linear regression compared to the first refinement study, thus decreasing the uncertainty on the calculations of P and Q. However, it is still not optimal, and future work could try to adopt the optimization technique laid out in the next section to find the equilibrium. In this case, it is not possible to follow the procedure of Eça and Hoekstra [27] to estimate the uncertainty on the damping values since the meshes do not have different refinements; however, from the relative comparison of the values P, Q, and ζ some conclusions can be drawn.

Case	Q [1/m]	Q Relative [%]	P [-]	P Relative [%]	ζ	ζ Relative [%]
Extra Fine	3.55E-02	0.00%	1.36E-01	0.00%	5.51E+00	0.00%
Fine	2.60E-02	-26.76%	1.77E-01	30.15%	5.39E+00	-2.18%
Medium	1.74E-02	-50.99%	2.67E-01	96.32%	5.83E+00	5.81%

Table 3.14: Results of the P-Q analysis for the second refinement study, 15m surge decay test

Case	A_1 [m]	A_1 rel.diff [%]	R^2
Extra Fine	-5.46	0.06%	6.59E-02
Fine	-5.46	-N/A	4.10E-02
Medium	-5.47	0.32%	6.72E-02

Table 3.15: Results of the amplitude for the second refinement study, 15m surge decay test

For future simulations, the fine mesh will continue to be chosen to ensure accurate approximation of large motions.

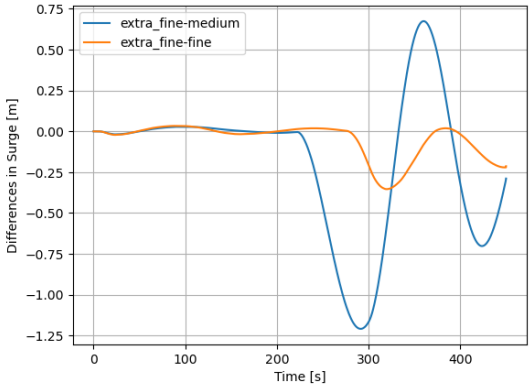

Figure 3.11: Difference in surge motions between the extra fine mesh and the fine/medium meshes in the second refinement study

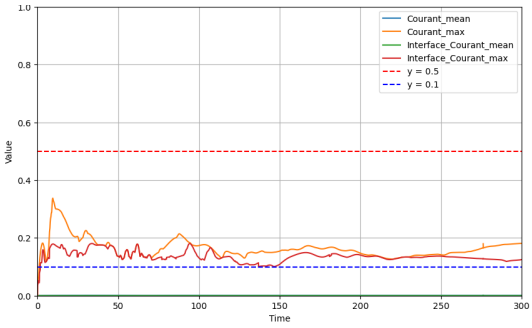

Figure 3.12: Courant numbers for the fine mesh, 15m Surge decay test

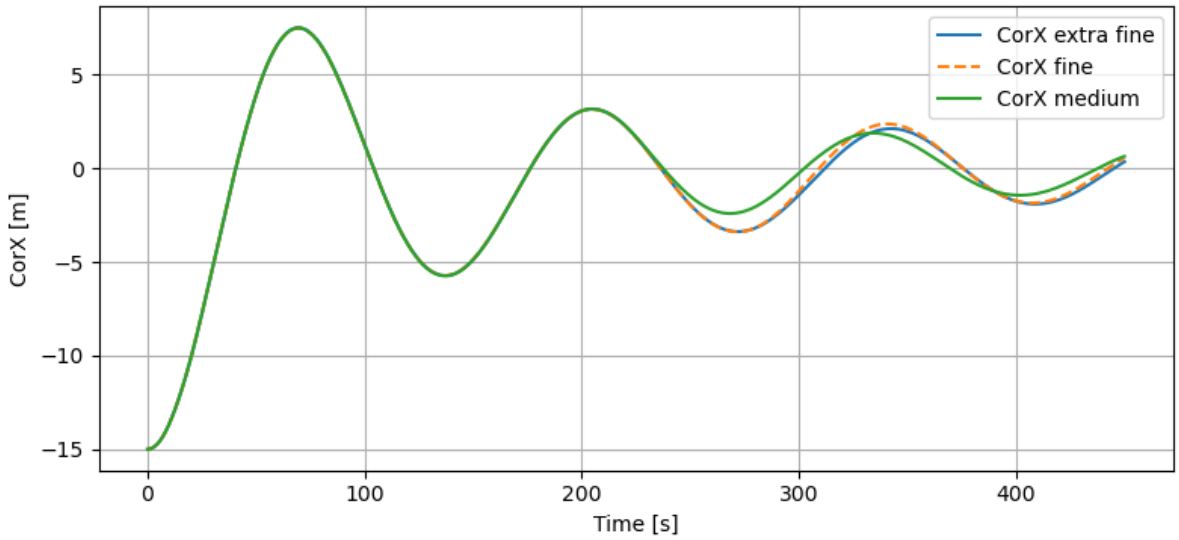

Figure 3.10: Surge decay test for the second refinement study, where the size of the refinement zone of the floater is varied

Additional sensitivity study: Surge decay test with 24m offset

To see how the increase of the offset affects the mesh result, the same refinement study is performed for 24m as well, which corresponds to the amplitude of the decay tests done in the Plymouth experiment when brought to scale. The goal is to show that even for bigger motions, the size of the cylinders used for 15m decay tests is also valid. From Figure 3.13, it can be seen that the movements of the floater are very similar for the first periods of the movement. The Table 3.16 confirms that all three meshes are similar in damping ratios, even suggesting that the medium mesh is closer than the fine mesh. However, these analyses were not run for long periods due to time constraints, so it isn't easy to be sure that this trend will continue until equilibrium. It can also be noted that the quadratic damping is more critical for more extensive motions when compared to the 15m Surge decay test from Table 3.14. The linear damping coefficient is lower for the part where the motion amplitudes are still significant. It is difficult, however, to confidently conclude this trend with these results since the linear regression is done on very few points. Still, it fits the analysis that quadratic damping dominates over linear damping for large motions. This trend will be further analyzed in the results section, where heave and pitch tests will be examined in more detail, and the simulation time will include more natural periods of motion. From this sensitivity study, however, one can justify using the same mesh for more significant motions.

Case	Q [1/m]	Q Relative %	P [-]	P Relative %	ζ	ζ Relative %
Extra Fine	-1.57E-02	0.00%	5.59E-01	0.00%	7.09E+00	0.00%
Fine	-9.35E-03	0.01%	4.93E-01	0.07%	6.80E+00	-4.21%
Medium	-1.48E-02	0.00%	5.50E-01	0.01%	7.05E+00	-0.66%

Table 3.16: P-Q analysis results for the sensitivity test on the 24m offset surge decay test

Case	A_1 [m]	A_1 Relative %	R^2
Extra Fine	-7.29	0.32%	1.43E-01
Fine	-7.29	N/A	6.98E-02
Medium	-7.32	0.44%	1.25E-01

Table 3.17: Amplitude analysis results for the sensitivity test on the 24m offset surge decay test

3.4.4. Bonus Part: Time optimization running on HPC12

In High-Performance Computing (HPC), compute nodes and cores are essential for large-scale computations. A compute node is a server within an HPC cluster, and each node has multiple cores within its CPU. These cores can work simultaneously, enabling parallel processing. By distributing tasks across many nodes and utilizing multiple cores per node, HPC systems can perform complex calculations

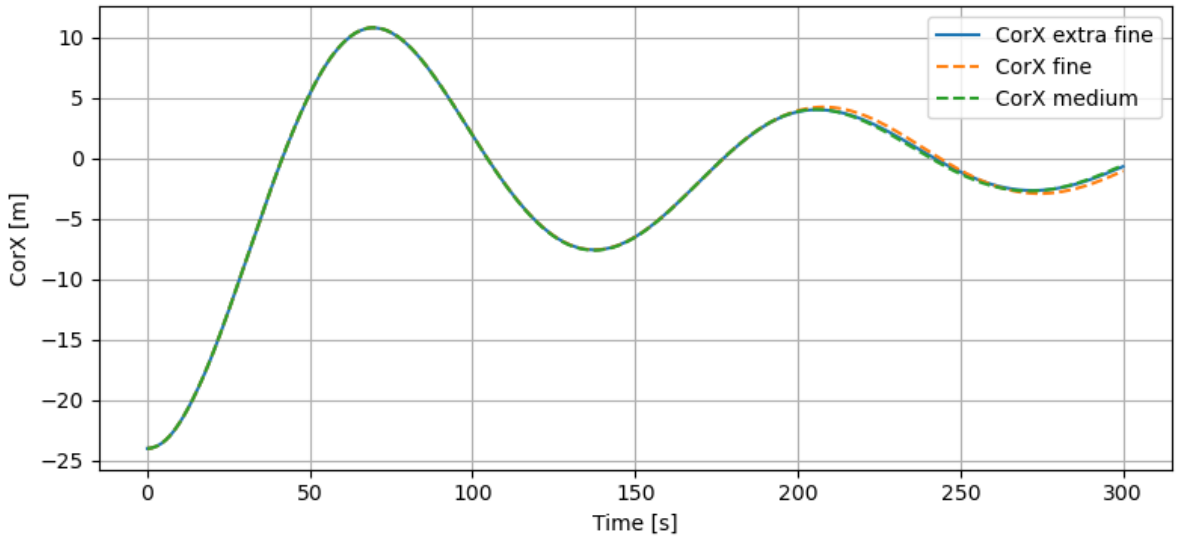

Figure 3.13: Sensitivity analysis of the mesh refinement zone around the floater for a surge decay test with a 24m offset

much faster than traditional computers. The objective is to choose an HPC architecture that closely aligns with the data structure, ensuring an even distribution of computational loads.

This section aims to show some characteristics of HPC12 of TU Delft and which running configurations to use for an optimal runtime. Despite using the same setup, some configurations were up to ten times slower during the experiments described above. A few cases were run to better understand the best practices to follow.

A surge decay test with a 15m offset and a coarse mesh was conducted using 160 cores in two different configurations: 5x32 cores on type J cores and 5x32 cores on type M cores. The type M cores were distributed across five nodes, each capable of containing 96 cores. Unlike the type J cores, which benefit from InfiniBand connectivity, the type M nodes were connected via Ethernet. During the simulation, another user utilized the remaining cores on the type M nodes. As shown in Table 3.18, despite having similar memory and an equal number of cores, the execution times per timestep varied significantly between the two configurations. The type M configuration showed a tenfold increase in execution time, likely due to the slower Ethernet connection hindering node communication.

Configuration	**Type J**	**Type M**
Number of cores per node	160	160
Number of nodes	5	5
Memory available per simulation (GB)	480	426
Mean execution time (s)	14.29	128.7

Table 3.18: Comparison of configurations with type J and type M nodes

Another simulation that has been run is a heave decay test, where the same simulation was run on a different number of cores. All the simulations were run on the same type of cores. The results given in Table 3.19 show an optimum number of cores for which the simulation can not be optimized. It may be inferred that the simulation time would remain constant after an inevitable increase in the number of cores. There would be a physical limitation since some calculations would not be parallelized anymore. However, the experience shows that the runtime increases if the number of cores increases too much. This might be due to the communication between the nodes. Since the data from the previous timestep is used for every timestep, one core has to access data from more cores if the mesh is split among a more significant amount of cores, which increases the total runtime. It also has to be noted that the parallelization method is essential since some regions might become bottlenecks if one area has a more critical number of calculations to do because of poor convergence.

Number of cores	60	80	100	120	140	160	200
Number of nodes	3	4	5	6	7	8	10
Memory per node (GB)	256	256	256	256	256	256	256
Cores per node	20	20	20	20	20	20	20
Execution time/timestep (s)	98.33	56.16	23.00	178.57	179.86	59.75	144.00
Execution time/(core*timestep) (s/core)	1.64	0.70	0.23	1.49	1.28	0.37	0.72
Faster runtime	1.00	1.75	4.28	0.55	0.55	1.65	0.68
Cells per core	159311	119483	95587	79655	68276	59741	47793

Table 3.19: Sensitivity study on the number of nodes used to perform a 5m heave decay test

3.5. OpenFAST modelling

To minimize the aerodynamic damping, the OpenFAST files have been set so that the rotor is not rotating and the pitch is null. The other parameters of the OpenFAST simulations are set to be coherent with the OpenFOAM parameters.

The provided settings configure the initial conditions for the wind turbine simulation. The `GenDOF` parameter is set to `Off`, and `PCMODE` is set to `0`, indicating that the generator degrees of freedom and the pitch control mode is disabled, thus simplifying the simulation by excluding active control systems. Additionally, `VSContro` is `0`, confirming that variable speed control is turned off, which means the turbine operates at a constant speed. The rotor speed is set to `0` with `RotSpeed`, implying that the turbine is stationary at the start. Both `CompInflow` and `CompAero` are set to `0`, suggesting that inflow and aerodynamic computations are disabled, further simplifying the model. The `GenTiStr` parameter is set to `True`, indicating that time-dependent generator structural effects are included.

The RNA (Rotating Nacelle Assembly) offset settings in the Elastodyn module for initial platform displacements are adjusted to zero. This includes setting `Precone angles` to `0`, `Overhang` to `0`, `NacMxn` to `0`, and `NacMzn` to `0`. These adjustments ensure no initial offsets or misalignments in the nacelle's position relative to the platform, establishing a baseline condition for the simulation with minimal initial perturbations.

Regarding the hydrodynamic modeling in OpenFAST, still, water is modeled using `WaveMod=0`. This implies that no waves are simulated, and no current is modeled. The configuration utilizes WAMIT-based frequency-to-time domain transformations for potential flow modeling, along with a DFT-based wave excitation model. No second-order floating platform forces could be included since the still-water model within OpenFAST was used. No additional linear restoring stiffness or linear damping was added. However, the platform's characteristics included the standard additional quadratic drag.

A quick note on the accuracy of this model. A potential flow model is used in the present case: WAMIT output files such as the linear dimensionless hydro-static restoring matrix, frequency-dependent hydrodynamic added mass matrix, and damping matrix are used. Also, the convolution method is used to track the radiation memory effect. The quadratic damping is modeled with the additional quadratic damping matrix. From the developers of OpenFAST, it is best practice to tune the hydrodynamic coefficients and other physical properties of the model before tuning the additional linear stiffness `AddCLin` or the additional linear damping `AddBLin`. The viscous drag matrix was derived using CFD simulations and SimpleFOAM. The main limitation of using simpleFoam is that it is a solver that does consider only one fluid and does not account for the interaction between the air and the surface. Thus, some damping is left out from the near-surface effects that have been described and for which OpenFAST has been modified in Wang et al. [114].

Within Hydrodyn, it is also possible to manually tune the hydrodynamic characteristics and use them in place of the strip theory. Strip theory models hydrodynamic loads on multi-member substructures, where the members can be inclined, tapered, flooded, or ballasted with marine growth. It accounts for distributed loads like inertia, added mass, and viscous drag using the Morison equation, as well as concentrated loads at member ends and axial loads on tapered members. Hydrodynamic loads are derived from undisturbed wave and current kinematics at the undisturbed position of the structure. This method particularly applies to fixed-bottom and floating platforms with slender members and complex

interconnections. More details can be found in the Hydrodyn guide. This approach has been used to improve OpenFAST during the OC6 campaign to better account for nonlinear low-frequency forces in wave conditions Wang et al. [114]. This tuning, however, is out of the scope of this thesis and will be one of the outcomes of OC7.

3.6. Results: Comparison with OpenFAST

This section compares the high-fidelity OpenFOAM simulations to the mid-fidelity OpenFAST simulations. It shows which motions OpenFAST provides a decent fit to high-fidelity simulations. Decay tests will be run and compared to OpenFAST simulations.

For this section, the OpenFOAM setup has also been corrected, and the new equilibrium position is now like the following :

Solver	Surge [m]	Sway [m]	Heave [m]	Roll [deg]	Pitch [deg]	Yaw [deg]
OpenFOAM	-6.25E-03	5.46E-03	-15.09	1.77E-03	7.35E-04	1.38E-04
OpenFAST	1.65E-04	2.68E-06	-15.28	2.64E-07	5.5E-04	7.17E-07

Table 3.20: Equilibrium position of the floater for OpenFAST/OpenFOAM study

From that comparison, one can see that both configurations are close to one another, except for the equilibrium position of the vertical axis. This may be due to the difference in the mooring modeling as described in subsection 2.1.2.

3.6.1. Surge decay tests

Surge decay tests with amplitudes of 5m, 10m, 15m, and 24m were run for 600s in both OpenFAST and OpenFOAM.

The P-Q analysis was initially performed as outlined in subsection 3.2.2. The study results are shown in Figure 3.14. From the graph, it is evident that for the OpenFAST simulations, the data aligns well with a linear function, where the offset, i.e., the linear damping, is almost negligible compared to the mean from the OpenFOAM simulations. In contrast, the OpenFOAM data appears scattered and includes some anomalies, such as negative decreases in amplitude. These anomalies suggest that the floater may accelerate during a half cycle, reaching a higher amplitude than in the previous cycle.

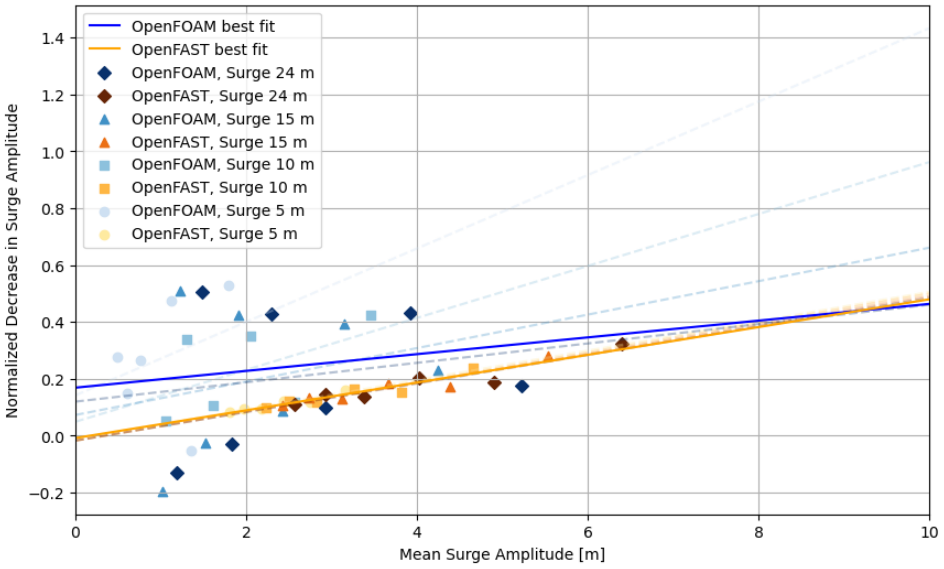

Figure 3.14: Mean amplitudes vs. normalized amplitude decrease (P-Q analysis), for surge movements, over half cycles without optimization

It is worth noting that the best-fit curve deviates even further if the first amplitude value is included, which is consistent with recommendations from the literature to exclude this data point [115]. Several

factors contribute to this behavior and have been investigated. First, there is a significant sensitivity to the floater's equilibrium position, subtracted from the data to account for oscillations around the mean position. Using the average position over the simulation is insufficient, as significant variations occur, and even differences of 5 cm can significantly impact the results due to extensive post-processing. This offset in the mean position explains the negative values and the apparent symmetry in the curves, as observed in the 24m decay test. However, this issue is only present in the OpenFOAM simulations and not in the CFD simulations performed by Wang et al. [115]. One explanation could be `Moody`, which shows different behaviors because it is more accurate than `Moordyn` in large amplitude motions. However, both mooring line models should perform similarly for small motions. Another possible explanation is that the equilibrium position in OpenFOAM differs between decay tests, likely due to variations in the mesh quality of the deformed mesh at equilibrium.

Optimization of the equilibrium position

Different optimization strategies were tested to find the equilibrium positions for each OpenFOAM simulation numerically. The analysis results are given in Table 3.21. A first attempt was to determine the equilibrium position in OpenFOAM simulations using a best-fit algorithm that minimizes the error between the surge data points and a fitted exponential decay function employing a dichotomy algorithm. It was first thought that this method would ensure that there is also a high correlation factor between the mean surge amplitude and the normalized decrease in amplitude. However, this approach assumes that the decay test is an exponential decreasing oscillation, ignoring the quadratic damping terms. Simulated annealing method and brute force have also been tried to find the optimum for an exponential decay. The optimization improved the exponential fitting of the surge decay test for every optimization method tested. However, it did not improve the results of the P-Q analysis significantly $r^2 = 0.18$, leading to worse results for the low amplitude surge decay tests as seen in Table 3.21. Another way of optimizing the equilibrium position based on the simulation is to fit the data points of the P-Q analysis to a linear curve. This assumption is debatable since Wang et al. [115] only tested a decay test with a 5m initial offset on a scaled Deep-Sea Wind floater, albeit with a very high correlation factor. However, Table 3.21 shows that the linear fit gives more coherent results: the equilibrium positions are closer, and the correlation factors are higher. With this way of optimizing, one could reach a generally higher correlation factor of 0.21, even 0.70, if the 5m surge case was excluded.

Surge Decay Test	Strategy	Surge Equilibrium [m]	P [-]	Q [1/m]	R^2
5m	No optimisation	-6.25E-03	1.42E-01	1.29E-01	9.06E-02
	Exponential fitting	-8.63E-02	3.16E-01	-1.29E-02	5.12E-04
	Linear fit	-1.24E-02	1.67E-01	1.09E-01	6.77E-02
10m	No optimisation	-6.25E-03	4.92E-02	9.13E-02	2.72E-01
	Exponential fitting	-1.34E-01	1.80E-01	3.53E-02	1.78E-01
	Linear fit	-9.57E-02	1.43E-01	5.12E-02	4.95E-01
15m	No optimisation	-6.25E-03	7.31E-02	5.88E-02	6.86E-02
	Exponential fitting	2.62E-01	1.79E-01	3.23E-02	1.36E-01
	Linear fit	1.91E-01	1.50E-01	3.96E-02	9.78E-01
24m	No optimisation	-6.25E-03	1.20E-01	3.41E-02	3.98E-02
	Exponential fitting	4.34E-01	2.83E-01	-7.17E-04	1.92E-05
	Linear fit	2.19E-01	2.03E-01	1.65E-02	4.18E-01
Every datapoint	No optimisation	NA	1.69E-01	2.95E-02	1.64E-01
	Exponential fitting	NA	2.59E-01	5.91E-03	3.83E-02
	Linear fit	NA	2.13E-01	1.64E-01	2.18E-01

Table 3.21: Results of the P-Q analysis by identifying varying surge equilibrium positions in OpenFOAM, using different optimization methods

To test the hypothesis that the average value plays a significant role, an adapted P-Q analysis was conducted on complete cycles, comparing only the maxima of the amplitudes instead of the extrema. In that way, the influence of the mean value is left out. While the P-Q analysis is also applicable over

two half cycles (as described in the appendix), the approximations become more significant, and both P and Q are mathematically doubled. However, the approximation errors increase as the approximate expression of the velocity becomes less valid. The results are presented in Figure 3.15. From Table 3.22, it is clear that this approach has improved the correlation factor between the two datasets for both OpenFOAM and OpenFAST, especially in the case of OpenFOAM. If the linear optimization was used, the global correlation factor even reaches 0.91 of the OpenFOAM simulations, where the equilibrium positions converge to the same values as in Table 3.21. This indicates that the choice of the mean value is crucial when performing a P-Q analysis. The optimized P-Q analysis, however, did not resolve the disparity for the 5m decay test, which could highlight the importance of the mooring modeling, which will be further highlighted during the analysis of the heave decay test.

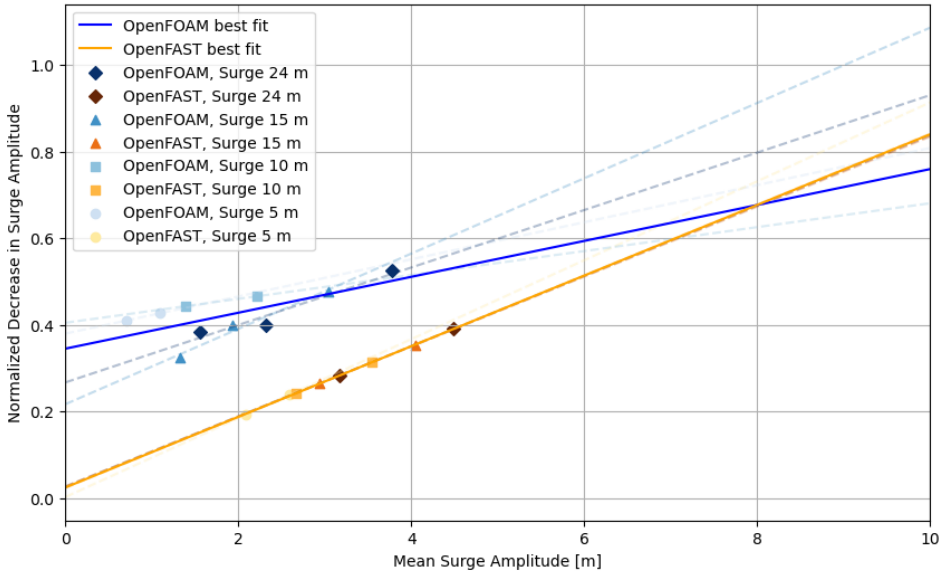

Figure 3.15: P-Q analysis on surge movements, over full cycles, without optimization

Case	Software	R^2	P [-]	Q [1/m]
Full cycles	OpenFOAM	0.69	0.34	0.04
	OpenFAST	1.00	0.02	0.08
Half-cycles	OpenFOAM	0.16	0.16	0.29
	OpenFAST	0.96	-0.01	0.05

Table 3.22: Best fit comparison for surge decay tests performing a P-Q analysis, with equilibrium position based on the equilibrium simulations

General P-Q analysis

To compare the OpenFAST simulations with the OpenFOAM simulations, linear optimization to adjust the equilibrium positions and a half-cycle analysis have been chosen, as it is unclear how accurate the full-cycle P-Q analysis is regarding the assumptions.

Overall, it can be said that the OpenFAST simulations are very consistent and almost independent of the amplitude since it is diverging a little for higher amplitudes, showing the minor limitations of a P-Q analysis for high-amplitude motions. The consistency and high correlation factor can be explained by the fact that OpenFAST does not show the same degree of non-linear behaviors as OpenFOAM and assumes a more linearized framework. It does not efficiently capture turbulence, vortex shedding, or near-surface, which becomes more critical for high amplitude decay tests. More importantly, surge, like sway and yaw, are motions with weak or absent hydrodynamic restoring forces. Unlike heave, where buoyancy provides restoring force, horizontal motions mainly rely on the mooring system for restoring forces. For large amplitude free decay tests in these directions, the mooring system's dynamics play

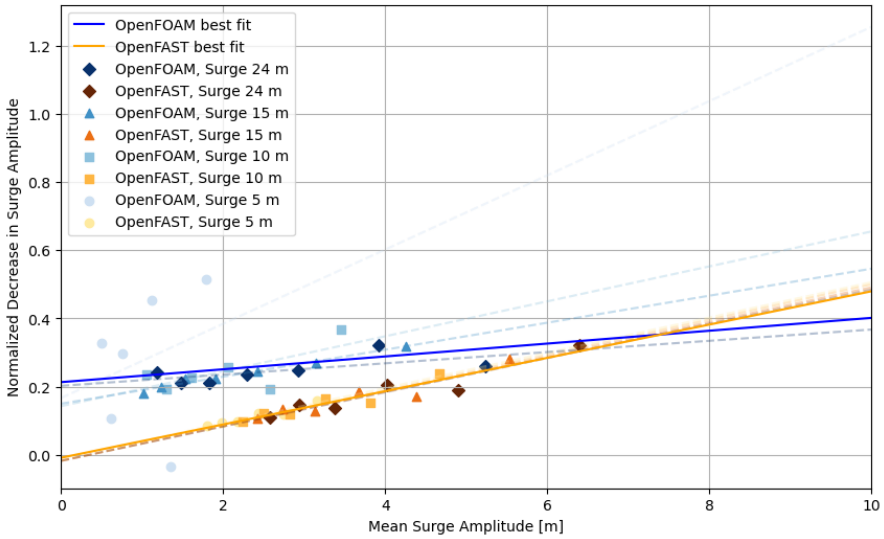

Figure 3.16: P-Q analysis on surge movements, using linear optimization to get the equilibrium positions

a crucial role in the platform's response. In this context, snap loads can occur if the mooring lines go slack due to excessive displacement and rapidly tighten when the platform moves back. These events are highly nonlinear and require accurate tension modeling, which `Moody`'s FEM approach is better at handling than the more straightforward lumped mass method used by `MoorDyn`. A more detailed analysis of the mooring loads was not conducted due to lack of time but could be part of future work to analyze key differences between `Moody` and `MoorDyn`.

Going more in detail, keeping in mind that there is a low correlation factor for the OpenFOAM simulations, the following trends can be observed :

- **Period P**: The period differences between the two platforms are minimal, with a relative variation ranging from 1.17% to 4.21%. This suggests both simulations capture similar mass-inertia and restoring force properties of the floater. However, OpenFAST tends to slightly overestimate the period, especially for high initial displacement decay tests. In OpenFOAM, the system becomes stiffer as the amplitude increases, reflecting the higher ability of `Moody` to capture high-amplitude motions. The role of the deformed mesh is unknown and could also be part of the explanation for the growing discrepancy with rising amplitude.
- **P coefficient**: There is a significant discrepancy between OpenFOAM and OpenFAST for the P coefficient, with OpenFAST showing slightly negative values in all cases; the linear damping is not the most important in OpenFAST. The contribution of linear damping to global damping is much higher in OpenFOAM, which may indicate that linear damping is underestimated in OpenFAST. This may be due to tuning linear damping coefficients using potential flow theory.
- **Q coefficient**: The Q coefficient varies significantly in OpenFOAM simulations. This might be due to the mooring modeling at high amplitudes, which shows an outlier for the second mean surge amplitude at 5.3m. Regarding the 5 m surge decay test, it is unclear what exactly causes the difference in behavior compared to the other decay tests.
- **Normalized quadratic coefficient**: Similarly to the previous analysis, there is a lot of uncertainty regarding the normalized quadratic coefficient. Analyzing the results for OpenFOAM, one notices that the normalized damping coefficient decreases with the amplitude, although it should increase with the higher amplitude. This can be explained by the fact that the P-Q analysis deviates at high amplitudes because it relies on the hypothesis described in subsection 3.2.2. Interestingly, the damping seems slightly more linear than quadratic in OpenFOAM simulations, whereas the damping in OpenFAST is quadratic.
- **Linear equivalent damping coefficient** ζ: OpenFOAM predicts a consistently higher damping ratio ζ compared to OpenFAST, suggesting more substantial energy dissipation in OpenFOAM

Case	Parameter	OpenFOAM	OpenFAST	Relative %
Surge_05	Period [s]	1.35e+02	1.36e+02	1.17%
	P [-]	1.67e-01	-1.02e-02	-106.09%
	Q [1/m]	1.09e-01	5.16e-02	-52.52%
	$F_A * Q$ [-]	1.51e-01	1.32e-01	-12.66%
	ζ	6.00e-02	1.96e-02	-67.42%
	First Minima Amplitude [m]	-2.25e+00	-3.41e+00	51.40%
Surge_10	Period [s]	1.34e+02	1.37e+02	2.46%
	P [-]	1.43e-01	-1.70e-02	-111.87%
	Q [1/m]	5.12e-02	5.17e-02	0.97%
	$F_A * Q$ [-]	1.35e-01	1.88e-01	38.98%
	ζ	4.61e-02	2.78e-02	-39.80%
	First Minima Amplitude [m]	-4.09e+00	-5.22e+00	27.43%
Surge_15	Period [s]	1.32e+02	1.37e+02	3.85%
	P [-]	1.50e-01	-1.73e-02	-111.54%
	Q [1/m]	3.96e-02	5.09e-02	28.57%
	$F_A * Q$ [-]	1.27e-01	2.17e-01	71.30%
	ζ	4.46e-02	3.26e-02	-26.99%
	First Minima Amplitude [m]	-4.92e+00	-6.31e+00	28.12%
Surge_24	Period [s]	1.32e+02	1.37e+02	4.21%
	P [-]	2.03e-01	-1.69e-02	-108.33%
	Q [1/m]	1.65e-02	5.02e-02	204.15%
	$F_A * Q$ [-]	6.53e-02	2.45e-01	274.60%
	ζ	4.28e-02	3.75e-02	-12.51%
	First Minima Amplitude [m]	-5.91e+00	-7.43e+00	25.73%

Table 3.23: Comparison of OpenFOAM and OpenFAST Simulation Results for surge movements observed during surge decay tests

and in the mooring model, which is coherent with the high linear damping ratios. The relative difference in ζ ranges from -67.42% to -12.51%, indicating that OpenFOAM simulates more dissipation of surge energy compared to OpenFAST, possibly due to better resolution of viscous and wave-induced damping forces in the CFD-based model.

- **First minima amplitude**: The first minima amplitude, which was chosen over the first maxima to leave out the transient behavior happening in OpenFOAM during the first half period, is consistently over-predicted by OpenFAST, by differences of 1.2-1.5m. It has to be noted that when looking at the first maxima amplitude, it seems that OpenFAST and OpenFOAM simulations coincide more for higher amplitudes than for lower amplitudes. It is unclear why OpenFAST is not closer to the OpenFOAM simulations for the 5m decay test, as it needs a more detailed investigation. The 5m decay test is also an outlier regarding the correlation factor of the P-Q analysis as depicted by the light blue dots in Figure 3.14. One shortcoming could be that the movement was not constrained in the surge direction and that the floater had to reach its equilibrium position at 15.13m during the simulation.

In conclusion, the comparison between OpenFOAM and OpenFAST simulations for surge decay tests highlights several significant differences, mainly due to the distinct modeling approaches of each software. OpenFAST provides consistent results across various amplitudes, thanks to its more linearized framework, but it fails to capture the complex nonlinearities present in OpenFOAM, particularly for high-amplitude decay tests. OpenFOAM's CFD-based model accounts for critical effects such as turbulence, vortex shedding, and mooring dynamics, leading to higher energy dissipation and variable damping behavior. The differences in P and Q coefficients and the damping ratio ζ underscore OpenFOAM's ability to simulate nonlinear hydrodynamic effects. At the same time, OpenFAST simplifies these dynamics, showing weaker performance in capturing the nuances of large-amplitude motions. To analyze the differences in detail, one can perform surge decay tests using `MoorDyn` in OpenFOAM to remove that

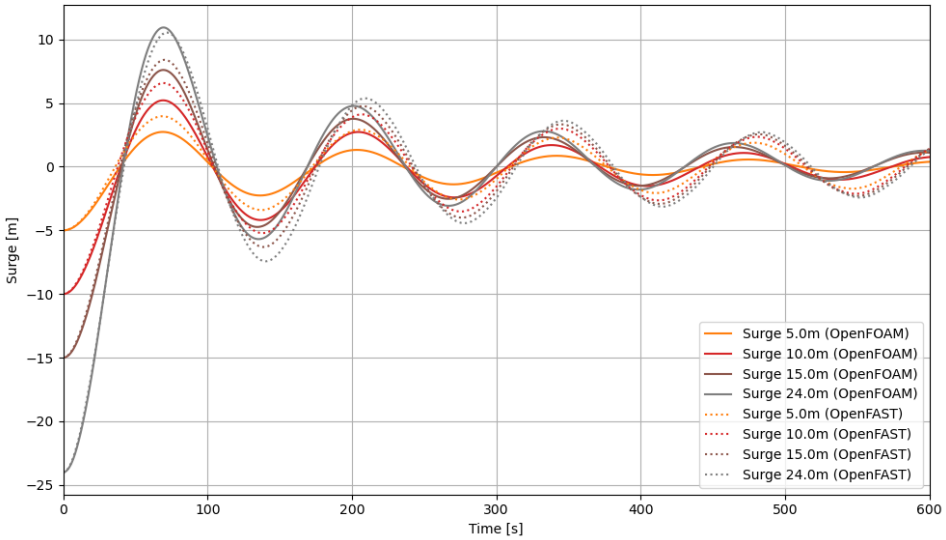

Figure 3.17: Comparison of surge position during surge decay tests between OpenFAST and OpenFOAM

modeling difference and focus on the differences in the modeling of hydrodynamic loads. To perform an even more detailed analysis, but less realistic, one could also constraint the motion of the floater in the surge direction to prevent the floater from moving in the vertical direction (max 0.2m amplitudes) and the pitch direction (max.0.2 degrees) and add additional damping. Even though this slight deviation could not explain the significant differences, it may highlight the proportion of the modeling differences.

3.6.2. Heave decay tests

In this case, heave decay tests were conducted at 2.5, 5, and 7.5 meters offsets. It has been tried to run a 10-meter decay test, but the simulation failed due to numerical instabilities. It was assumed that the mesh used in the surge decay tests could be reused, with the only modification being the extension of the refinement zone vertically around the floater to capture the flow better in the oscillating direction. The mesh refinement remained unchanged, although a mesh refinement study would be ideal to ensure the extraction of accurate values. Since the period of oscillation in heave is shorter than in surge, the simulation timestep was reduced to $dt = 0.03$. While a temporal discretization study would be preferable, the Courant number was maintained below 0.5 for stability.

In contrast to surge motion, the restoring force in heave motion is primarily driven by buoyancy, with the mooring forces playing a minimal role. This allows for a more direct comparison of the accuracy of the P-Q analysis in this case with the previous surge scenario, providing insight into the impact of mooring modeling on the results.

Optimization of the equilibrium position

As for the surge decay tests above, it was found that looking for the optimum equilibrium position would enhance the results of the P-Q analysis.

The Table 3.24 presents the results of P-Q analysis for heave decay tests, comparing OpenFOAM and OpenFAST post simulation's post-processing under different conditions: complete cycle vs. half cycle analysis and with/without equilibrium position optimization.

The results from the heave decay tests indicate that OpenFAST consistently outperforms OpenFOAM in both full-cycle and half-cycle analyses, showing near-perfect correlation ($r^2 \approx one$) and stable values for P and Q, regardless of optimization. Conversely, OpenFOAM benefits significantly from optimization, particularly in half-cycle analysis, where the correlation improves drastically from $r^2 = 0.177$ to $r^2 = 0.946$. While linear optimization marginally improves OpenFOAM's performance in full-cycle analysis, the adjustments to P and Q are minimal. This suggests that OpenFAST is less dependent on equilibrium position tuning, as it is independent of the studied case, providing reliable results without optimization. In contrast, OpenFOAM requires careful adjustment for accurate half-cycle predictions.

Case	Equilibrium Position	Software	R^2	P [-]	Q [1/m]
Full cycle	No optimisation	OpenFOAM	0.9370	0.0946	0.2480
		OpenFAST	0.9999	0.0028	0.1405
Full cycle	Linear optimisation	OpenFOAM	0.9832	0.0796	0.2435
		OpenFAST	0.9999	0.0028	0.1405
Half cycle	No optimisation	OpenFOAM	0.1771	0.0022	0.3918
		OpenFAST	0.9989	0.0010	0.0712
Half cycle	Linear optimisation	OpenFOAM	0.9456	0.0260	0.1489
		OpenFAST	0.9989	0.0010	0.0712

Table 3.24: Optimization of the offset position for the heave decay tests

The change due to optimization is visualized in Figure 3.18.

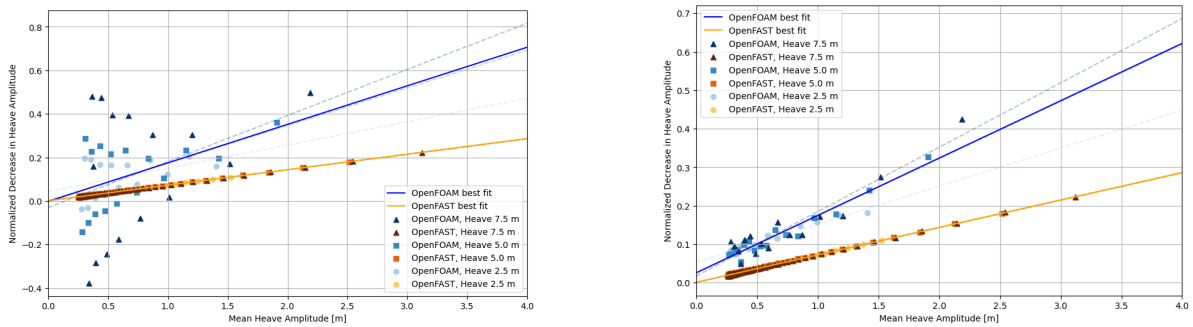

Figure 3.18: Comparison of two P-Q analyses for heave decay tests: without optimization (a) and with linear optimization (b)

General P-Q analysis

After optimization of the equilibrium position for each heave case presented in Figure 3.19, a P-Q analysis is performed, and results are given in Table 3.25.

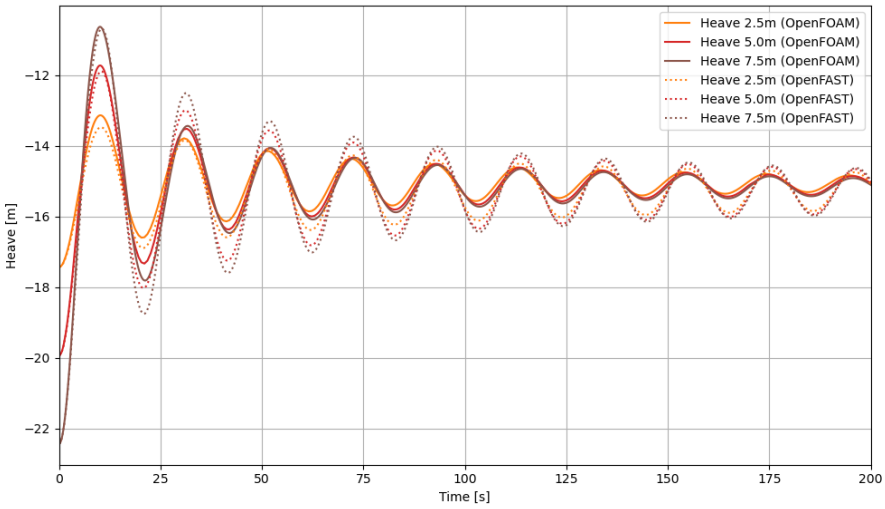

Figure 3.19: Comparison of heave position during heave decay tests between OpenFAST and OpenFOAM

The following elements can be extracted from the analysis :

- **Period:** Both solvers show close agreement in the predicted period of oscillation, with relative differences consistently under 1%. This indicates that both OpenFOAM and OpenFAST accurately

Case	Parameter	OpenFOAM	OpenFAST	Relative %
Heave_25	Period [s]	2.05e+01	2.06e+01	0.49%
	P [-]	5.34e-02	8.71e-04	-98.37%
	Q [1/m]	9.87e-02	7.15e-02	-27.55%
	$F_A * Q$ [-]	9.57e-02	7.68e-02	-19.76%
	ζ	2.39e-02	1.24e-02	-47.87%
	First Minima Amplitude [m]	-1.53e+00	-1.61e+00	4.85%
Heave_50	Period [s]	2.05e+01	2.06e+01	0.69%
	P [-]	2.52e-02	1.19e-03	-95.29%
	Q [1/m]	1.49e-01	7.11e-02	-52.12%
	$F_A * Q$ [-]	1.88e-01	1.20e-01	-36.24%
	ζ	3.58e-02	1.96e-02	-45.23%
	First Minima Amplitude [m]	-2.22e+00	-2.74e+00	23.46%
Heave_75	Period [s]	2.05e+01	2.06e+01	0.62%
	P [-]	1.75e-02	1.43e-03	-91.82%
	Q [1/m]	1.67e-01	7.09e-02	-57.60%
	$F_A * Q$ [-]	2.43e-01	1.47e-01	-39.67%
	ζ	4.55e-02	2.41e-02	-47.05%
	First Minima Amplitude [m]	-2.65e+00	-3.47e+00	30.80%

Table 3.25: Comparison of heave motion parameters between OpenFOAM and OpenFAST

model the oscillation period.

- **P (Damping Coefficient):** There is a significant discrepancy in the P parameter, with OpenFOAM predicting much higher values than OpenFAST. Relative differences range from -91.82% to -98.37%, suggesting that OpenFOAM estimates higher damping than OpenFAST, which indicates that the viscous damping is less accurately captured in OpenFAST. As for the surge motion, the tuning in OpenFAST is slightly off. Since the correlation coefficient for OpenFOAM is more important, the confidence for the underprediction is higher than for the surge decay tests. The main contributor to linear damping is radiation damping, considered in OpenFAST. There may be an underestimation there. Finally, it may also be that since the motion is slow, the drag on the bottom of the floater is predominantly linear, but further research still has to be done.
- **Q (Quadratic Term):** The Q parameter shows a more minor but consistent difference, with OpenFOAM predicting higher values compared to OpenFAST. Relative differences vary from -27.55% to -57.60%, indicating that OpenFOAM accounts for more nonlinear effects in the heave motion. This can be explained by the fact that the OpenFAST quadratic damping model has been tuned using an OpenFOAM solver that does not account for near-water-level interactions, where the drag is more important.
- **Normalized quadratic term:** In OpenFOAM simulations, the quadratic coefficient increases with the amplitude, while for OpenFAST, it stays approximately the same for all the amplitudes. The increase in OpenFOAM can be explained by the fact that more viscous phenomena are happening, while in OpenFAST, this effect is not correctly captured. From these results, it can also be seen that the damping is predominantly quadratic.
- **Damping Ratio (ζ):** The damping ratio values also differ significantly, with OpenFOAM predicting higher damping ratios. The relative differences range from -45.23% to -47.87%, reflecting a more pronounced energy dissipation in OpenFOAM's model.
- **First Minima Amplitude:** The amplitude of the first minima is notably different between the solvers, with OpenFOAM predicting smaller values. Relative differences range from 4.85% to 30.80%, suggesting that OpenFOAM predicts a quicker decay in heave displacement compared to OpenFAST. In contrast to the surge decay tests, the small movements are more accurate than the bigger ones, highlighting the importance of the mooring modeling for surge decay tests, as it does not impact the motions in the heave direction, which is guided by the buoyancy.

Altogether, the damping is underestimated in OpenFAST compared to OpenFOAM. While in OpenFAST, the linear terms of the damping are small and approximately constant, as is the case for the quadratic damping term, the simulations in OpenFOAM show an increase of quadratic damping with the amplitude, suggesting that it becomes more important with the higher amplitudes, which takes over the linear damping terms. However, this is not the case for the OpenFAST simulations.

3.6.3. Pitch decay tests

The pitch study is less extensive than the previous analyses due to time constraints. The earlier setup was unsuitable for decay tests involving higher pitch angles. As a result, only a single decay test was conducted with an initial offset of 2.5 degrees.

Adjustments were made to the setup in OpenFOAM: the inner refinement zone around the floater was extended to account for its rotational motion. The floater was not tilted, as it was discovered that tilting caused unstable simulations beneath the tilted refinement cylinder. Additionally, the timestep was reduced to $dt = 0.025$ seconds. At all moments, the Courant number was kept below 0.5.

In OpenFAST, the mass properties were modified from the initial configuration to concentrate all the mass in the floater. It was observed that the tower and RNA (Rotor-Nacelle Assembly) significantly increased the mass moment of inertia, approximately doubling the period of the motion. To address this, the masses of the tower and RNA were set to zero and added to the mass of the floater. All degrees of freedom other than pitch were constrained to maintain the exact center of mass as in the OpenFOAM simulations.

General P-Q analysis

The results of the P-Q analysis are given in Table 3.26 and visually depicted in Figure 3.20.

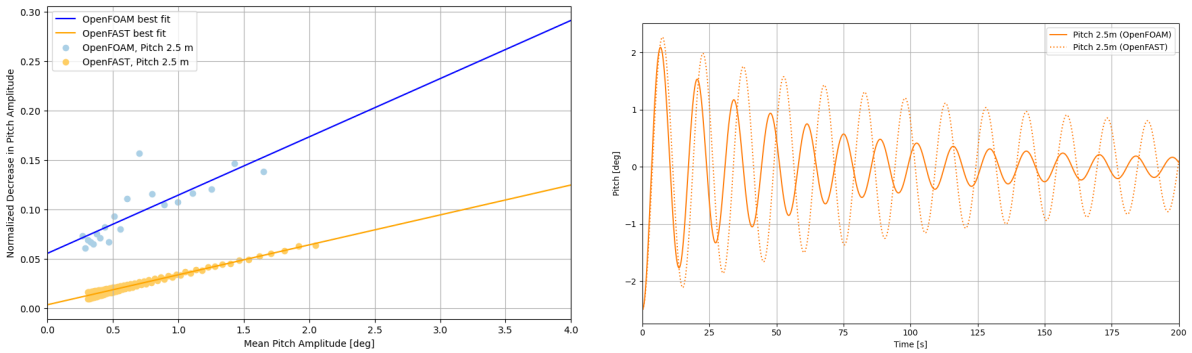

(a) (b)

Figure 3.20: P-Q analysis for pitch movements (a) and pitch amplitudes for the decay test (b)

Case	Parameter	OpenFOAM	OpenFAST	Relative %
Pitch_25	Period [s]	1.36e+01	1.51e+01	10.61%
	P [-]	5.55e-02	3.77e-03	-93.21%
	Q [1/m]	5.90e-02	3.01e-02	-49.04%
	$F_A * Q$ [-]	6.68e-02	4.38e-02	-34.37%
	ζ	1.93e-02	7.60e-03	-60.68%
	First Minima Amplitude [m]	-1.76e+00	-2.11e+00	19.77%

Table 3.26: Comparison of pitch motion parameters between OpenFOAM and OpenFAST

The following elements can be extracted from the analysis:

- **Period:** There is a 10% discrepancy in the periods. Several reasons may account for this: Firstly, the setup might not be fully adapted for pitch simulations, necessitating a convergence study to validate the mismatch in the modeling. Secondly, as pitch motion is influenced by both the mooring loads and the restoring force of the moorings, discrepancies in mooring modeling could explain

this variation as it did for Surge. Lastly, the altered inertia of the tower and rotor in OpenFAST might also affect how OpenFAST handles these dynamics.

- **P (Damping Coefficient):** Similar to the surge and heave cases, the linear damping coefficient is underestimated in OpenFAST. This is likely due to OpenFOAM's greater precision in capturing radiation damping and differences in mooring modeling. However, a more comprehensive convergence study in CFD modeling is needed for pitch analysis.
- **Q (Nonlinear Term):** The Q parameter also shows a difference, with OpenFOAM predicting higher values than OpenFAST. As observed in the heave case, OpenFOAM's quadratic damping coefficient is more significant, which can be attributed to its better representation of the near waterline drag during pitch motion.
- **Normalized quadratic term**: The linear damping coefficient in OpenFAST remains underestimated compared to OpenFOAM. This indicates that for small amplitudes, damping in OpenFAST is predominantly quadratic. In contrast, OpenFOAM shows a more balanced contribution from linear and quadratic damping components.
- **Damping Ratio (ζ):** The damping ratio differs significantly between the two models, with OpenFOAM predicting a higher value. This reflects the more pronounced energy dissipation captured by OpenFOAM's model, as seen in Figure 3.20b.
- **First Minima Amplitude:** In line with previous observations, the amplitude of the first minima is smaller in OpenFOAM compared to OpenFAST. This can be explained by the above reasons, including the more accurate representation of nonlinear effects in OpenFOAM.

The comparison of OpenFOAM and OpenFAST simulations for all surge heave and pitch decay tests reveals key differences between the two approaches, which are largely influenced by their distinct modeling techniques. OpenFOAM excels at capturing nonlinear hydrodynamic effects, such as turbulence, vortex shedding, and mooring dynamics, leading to more complex damping behavior and energy dissipation. OpenFAST, on the other hand, employs a more linearized and simplified representation of these dynamics, which results in consistent but less nuanced outputs, particularly in high-amplitude decay tests.

For surge decay tests, the P-Q analysis results demonstrate that OpenFOAM can simulate nonlinear phenomena at larger amplitudes, with increasing quadratic damping as the amplitude rises. Conversely, OpenFAST shows relatively stable damping coefficients, failing to replicate the complex nonlinearities observed in OpenFOAM. This discrepancy highlights OpenFOAM's capacity to model detailed fluid-structure interactions that become significant at higher amplitudes, whereas OpenFAST underestimates damping, primarily because of its simplified system representation. It also seems to differ in the linear damping, which can be inferred from the potential flow model and its modeling accuracy. Mooring line modeling differences could also be the cause for discrepancies.

The heave decay tests further corroborate these findings, though with notable differences in the role of restoring forces. In heave motion, buoyancy is dominant, with mooring forces being less significant. The P-Q analysis for heave decay revealed a similar trend as in the surge tests, with OpenFOAM capturing more pronounced nonlinear effects. The linear and quadratic damping coefficients in OpenFOAM displayed less variation with amplitude than for surge motions. At the same time, OpenFAST provided a more simplified picture, especially in higher amplitude motions. The underestimation of the quadratic damping may be due to a simplified tuning approach used in OpenFAST, while the simplified linear damping modeling in OpenFAST might also explain the difference.

The pitch decay test results show that for small amplitude oscillations, the P-Q analysis remains reliable, with high correlation coefficients. However, both linear and quadratic damping are underestimated in OpenFAST, as previously noted for heave and surge motions. A more detailed convergence study for pitch and heave is still needed to confirm this conclusion.

A common challenge in all cases is the application of P-Q analysis in high-amplitude decay tests, which is uncertain in ensuring a good comparison, especially for surge motions. The low correlation factor in OpenFOAM simulations, especially for low amplitude surge decay tests, suggests that P-Q analysis may not be the most effective tool for capturing dynamics for surge displacements. While there does not seem to be any issue with the heave displacements even for low displacements in pitch, it can

be concluded that the mooring model `Moody` has to be further investigated and eventually switched to `MoorDyn` within OpenFOAM to show similar behaviors with OpenFAST to be sure that the mooring model is the cause of this unexpected behavior.

One notable criticism is the application of P-Q analysis on high-amplitude decay tests. As a reminder, the P-Q analysis relies on writing down the loss of energy in terms of both potential energy and loss of energy due to linear and quadratic dampings. It is supposed to work for weakly damped motions when the approximations done are still realistic. The low correlation factor observed in OpenFOAM simulations indicates that this method may not be the most suitable for analyzing large motions. It is, however, unclear why small surge amplitude decay motions differ between OpenFAST and OpenFOAM; it may be inferred from the mooring modeling differences. More extended simulations can also be run to have more data points to perform a more reliable linear regression, and simpler mooring models can be used to assess the phenomenon's importance.

3.7. Outlooks for further validation studies

Estimating the modeling error or uncertainty is a task in the engineering process known as validation. It applies to the mathematical model and is carried out for a few chosen flow quantities, requiring experimental errors/uncertainties. It verifies that the correct equations have been solved. Unlike for verification, the modeling errors are the most relevant. Validation studies aim to validate the numerical studies with experimental data.

Renstchler et al. [89] have insisted on the importance of conducting verification and validation studies to create a good foundation for the comparison with experimental results. Their work indicated that CFD models accurately predict the hydrodynamic natural period. Still, careful tuning of the numerical setup has to be done to have correct damping coefficients. The restriction of motions also has to be thoroughly assessed, as geometric models can produce asymmetric flows.

While this study does not explicitly validate the numerical simulations, this section provides a comprehensive review of various experimental campaigns that can serve as a basis for future research. Due to time constraints and other modeling limitations, this validation was not feasible within the scope of this work.

Issues for validation campaigns

Comparing numerical results with experimental data obtained in laboratory basins remains a crucial step in the design process for most FOWT designers. As turbine sizes increase, the platform sizes of FOWTs also expand. To accommodate the growing dimensions of scale models and minimize the uncertainty in physical modeling, laboratory testing techniques for FOWTs are continually evolving. The geometrical, kinematic, and dynamic similarity between model scale and full scale is essential for the experimental validation of numerical models.

Since inertial forces dominate over viscous effects when analyzing the hydrodynamics of the floater, one can use the Froude number as a similarity number between the scaled model and the full-scale model :

$$Fr = \frac{U}{\sqrt{gL}} \tag{3.11}$$

U is velocity, g is gravitational acceleration, and L is physical length. It compares the inertial forces to the gravitational forces that apply to the body.

Similarly, the dynamic similarity requirement between the two scales used to compare aerodynamics is the Reynolds number :

$$Re = \frac{UL}{\nu} \tag{3.12}$$

where ν is the kinematic viscosity. Since the kinematic viscosity of air remains constant for both the prototype and scale model, a Froude-scaled rotor with geometric similarity will exhibit a lower Reynolds number at the model scale compared to the full-scale rotor. The impossibility of matching Froude and Reynolds scaling is depicted Figure 3.21. λ_L is the length scale factor while λ_V is the velocity scale factor. If one uses the Reynolds scaling, the velocity is too high, which is unfeasible. On the other hand, if one chooses the Froude scaling, then the velocity of the turbine is too low, leading

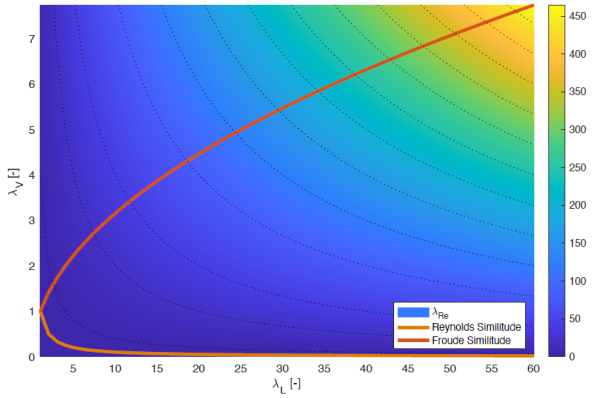

Figure 3.21: Froude-Reynolds scaling conflict as illustrated in [5], demonstrating the incompatibility of satisfying both Froude and Reynolds scaling simultaneously

to bad aerodynamics. As a result, the lift coefficient of the model-scale rotor will be lower, and the drag coefficient will be higher than that of the full-scale rotor, which causes a misrepresentation of the aerodynamic performance of the model-scale turbine. Nevertheless, the primary focus for scaled turbines is on accurately replicating Froude-scaled rotor thrust and torque. Rotor thrust is the most significant aerodynamic load influencing the motion response of FOWT models.

Complete physical testing is a way to emulate aerodynamic forces. It can be done with a mechanical pulley system that can capture steady thrust loads but cannot capture aerodynamic damping or the effects of turbine control [76]. Increasing wind velocity can lead to achieving an accurate rotor thrust. Still, maintaining the rotor speed at higher velocities means the tip speed ratio can not be maintained, leading to inaccurate aerodynamic dampings and rotor torque. Geometrically modified aerofoils to compensate for low Reynolds numbers are better for emulating aerodynamic loads and capturing damping effects and blade pitch control while maintaining TSR. This is called performance scaling of the rotor [5][80]. To accurately model floater motions under combined wave and wind loads in laboratory basins, the model turbine must have a correct thrust coefficient. In contrast, the influence of the power coefficient is negligible. This is achieved with performance scaling of the rotor.

Hybrid testing is an alternative to complete physical testing. This method generates waves physically, but a numerical substructure substitutes the aerodynamic loads. The Froude/Reynolds mismatch is addressed by calculating the full-scale aerodynamic loads and then applying them to the physical model at the Froude scale using one or more mechanical actuators. The two most commonly used actuators in hybrid FOWT wave basin testing have been dynamic cable winches and propellers, which have advantages and drawbacks as listed in [76]. Hall and Goupee [42] describes a possible setup and how it compares to physical wind-wave tests. This approach, however, provides a realistic aerodynamic thrust on the scaled model by calculating the force while accounting for the platform's motion, thereby incorporating the effects of aerodynamic damping. Due to latency, BEM is most commonly used to model aerodynamic loads in real-time, but it has limitations.

It is also possible to numerically model the hydrodynamic loads. This enables the validation of aerodynamic forces in an environment with better wind quality. This approach helps study the evolution of the turbine wake of FOWT and how downwind turbines and farm layouts are affected. The UNAFLOW campaign used this setup and later investigated the effect of large surge motions on aerodynamics during the IEA OC6 Phase 1a campaign.

Plymouth campaign, 1st comparative FOWT experiment

The hydrodynamic responses of the floating platform, especially the heave, surge, and pitch motions, significantly impact the wind turbine's aerodynamic performance. Consequently, the University of Plymouth provides the model and experiment data of a Y-shaped platform for floating offshore wind turbines to study the hydrodynamics of this platform, namely the 1st FOWT Comparative Study. The *1st comparative FOWT study* considers the hydrostatic and hydrodynamic response of a 1:70 scale model of the IEA 15MW reference wind turbine and the UMaine VolturnUS-S semi-submersible plat-

form. The test cases include static equilibrium load scenarios, free decay experiments (in heave, surge, and pitch), and focused wave scenarios (one 'operational' and one 'extreme'). It's important to note that this comparative study only considers hydrodynamic loading, excluding any aerodynamic loading on the floating offshore wind turbine (FOWT). The experimental layout and the characteristics of the floater can be found in the description file of the experiment [87].

Cui et al. [22] used STAR CCM+ with the overset meshing technique and found that errors in the period in the decay tests are within the margins, thus validating their setup. They also found good consistency for both the focused wave experiments.

Using OpenFOAM with a dynamic mesh, with `waves2foam` and `MoodyCore`, an improved version of `Moody2.0`, Eskilsson et al. [30] first tested the initial mooring setup as it was undetermined in the experimental campaign. Their model leads to a slightly different equilibrium position since the tensions differ from the experiment. Overall, a satisfactory agreement was also reached for focused waves.

Gong et al. [37] used QaleFoam combined with a dynamic mesh and a method similar to `Moody` also found good agreement with the experiment. Like Eskilsson, they have seen a higher tension in the fore fairlead. They also point out that for the focused wave experiment, the accuracy of the cable tension may be a reason for a difference in the surge motion. Jagdale et al. [53] also used the exact solver and reached the same conclusion.

Xue et al. [122] used the naoe-FOAM-SJTU solver combined with a quasi-static model and surprisingly found no mismatch with the experiment for the surge motion despite more considerable discrepancies in the pitch and heave motions. They attribute this to the different calculations of the mooring force.

Holcombe et al. [46] used Ansys AQWA to calculate rigid body coefficients that are then used to feed potential flow software Orcaflex and OpenFAST. They found that the decay tests were generally captured well, with less than a 5%

The FOCAL campaign and OC7

The turbine and platform designs are often proprietary, and performing basin-scale model tests can be costly. Similar to the DeepCwind [57], INNWIND.EU [3], and COREWIND [38] programs, the FOCAL project selected open designs for both the turbine and platform to provide an accessible dataset for floating offshore wind research. The FOCAL program used a performance-matched wind turbine modeled after the IEA Wind 15 MW reference turbine [34], including the Reference OpenSource Controller (ROSCO), with a Froude-scale floating platform and corresponding environments. The goal was to examine the aerodynamic load effects of controller actions in the coupled floating system and to assess the ROSCO controller's performance, where it controlled the blade pitch and generator torque. To date, fully coupled wind/wave experimental results with controls for the IEA Wind 15 MW turbine are not publicly available. The floater was a scaled version of the VolturnUS-S Floater [1].

The four experimental campaigns in the FOCAL project targeted turbine controls, hull design and flexibility, and fully coupled wind-wave dynamics. Results showed that numerical models replicated experimental results well, particularly regarding torque, thrust, tower top forces, moments, and damped system responses. With optimized controller parameters, the turbine controller reduced system dynamics and lowered costs. This validation confirmed that numerical tools can model real-time aerodynamic load responses, making them valuable for control co-design. Future work will enhance these tools and further integrate turbine control in upcoming experiments.

The first campaign [69] achieved several key milestones:

- Development of a performance-matched design methodology for scale-model testing of the IEA Wind 15 MW turbine.
- Integration of NREL's ROSCO controller into scaled-model experiments.
- Demonstration of control at model scale to simulate full-scale turbine performance.

Results from Campaign 1 will refine the 1:70 scale turbine model and ROSCO controller for future tests on floating platforms. FOCAL's datasets are publicly available.

The second and third experimental campaigns [113] involved model-scale wave-basin experiments with the VolturnUS-S semisubmersible platform fitted with three tuned mass dampers (TMDs). These

TMDs were designed to reduce the system's response to wave excitation by tuning them to either the platform's pitch resonance or the first fore-aft tower-bending resonance. Comparisons with a baseline case, where TMDs were locked, showed significant reductions in floater motion and system load. When tuned, the TMDs reduced platform pitch motion by 21% to 47% and tower-base bending moments by approximately 60%. Over the entire frequency range, pitch motion variance was reduced by up to 23%, while tower-bending variance was reduced by 3% to 8%.

The experimental data was used to validate modeling tools for capturing the influence of hull control on floating wind systems. These validated tools are crucial for control co-design, which integrates control systems into the design optimization process to reduce costs further. The models aligned well with the experimental results, but some overpredicted the TMD effects, likely due to difficulty capturing nonlinear wave excitation and viscous hydrodynamic damping. The preliminary validation suggests future model improvements should focus on better-predicting platform resonance and tower-bending moments.

The fourth campaign [33] used OpenFAST simulations to model the FOCAL Campaign 4 floating wind turbine experiment, analyzing wind-only, wave-only, and combined wind-wave cases. Comparisons between simulations and experiments revealed good agreement in platform surge, pitch, and tower-base bending moments, though OpenFAST underpredicted surge response at the platform's natural frequency. For wind-only cases, rotor torque variations in the experiment led to differences in blade pitch actuation and rotor speed regulation compared to OpenFAST predictions. OpenFAST further underpredicted surge resonant responses in combined wind-wave conditions, likely due to differences in aerodynamic damping and viscous effects. However, blade pitch activity increased at higher frequencies, leading to more significant platform pitch motion and tower-base moments in both the simulation and the experiment.

The FOCAL project faces a few limitations about the scope of the project, particularly concerning the availability and scope of data. As of the time of writing, data from the decay tests are not yet available; these tests are scheduled to begin after the initial forced oscillation tests, which will continue until July, with decay tests planned for July and August. Additionally, the published data for the FOCAL campaign focuses on control strategies, as seen in campaigns 2 and 3, or on the turbine alone, without incorporating control aspects. While the project is valuable for its fully coupled model, it lacks the inclusion of control in the data currently available, which could limit its applicability for studies specifically interested in control mechanics.

OC7

Different campaigns have been made to understand the behavior of CFD simulations better. The campaigns presented in subsection 1.2.2 highlight the need for CFD simulations to capture accurately nonlinear loads for smaller floaters, the DeepCWind floater surmounted with the NREL 5MW wind turbine. However, those do not correspond to the standard installed offshore; some FOWT farms even project to install 22MW wind turbines, even though they do not exist yet. To address this issue, the IEA has initiated a new collaboration campaign OC7, which is based on the VolturnUS-S floater [1], which can hold the IEA 15MW wind turbine [34]. Since this is recent, few campaigns have been made, and few CFD results have been published. This section aims to describe the floater and the experimental campaigns that have been created.

OC7 Phase I aims to enhance hydrodynamic modeling practices for floating offshore wind turbine (FOWT) platforms, focusing on viscous loads. The main deliverable outlines recommended hydrodynamic model formulations and tuning practices applicable to various designs. The project will investigate hydrodynamic model formulations for standard platform components and analyze how optimal coefficients (e.g., added mass, damping, drag) vary with flow conditions.

To support these mid-fidelity modeling improvements, OC7 Phase I will use high-fidelity computational fluid dynamics (CFD) simulations to study hydrodynamic viscous loads on rectangular pontoons commonly found in floating offshore wind semisubmersibles. The CFD simulations will explore localized hydrodynamic loads and their dependence on the Keulegan-Carpenter number in different conditions. This includes forced oscillation and free decay in calm water and regular wave simulations. The CFD work will encompass both 2.5D and 3D simulations of various pontoon configurations, aiming to ensure the validity and consistency of the simulation results.

As it was ongoing during the thesis, it was not used to validate the built CFD model; however, this could be part of future work. Also, the mesh proposed within this task is about 28 million cells, considered too high to do fully coupled simulations.

3.8. Key findings

In this chapter, we first completed a spatial convergence study and identified the optimal parameters that balance computational efficiency and accuracy. After discovering the instability of using dynamic timesteps, constant time-stepping was used. This led to the drawback that the Courant numbers were not kept below the same threshold, leading to a discrepancy in the extra-fine mesh.

Then, an optimal refinement zone was found for a 15m decay test, balancing accuracy and computational efficiency. This mesh has proven good quality for a 24m decay test. Both convergence studies found that more extended simulations were needed to have more data points and do a more convergent P-Q analysis. A temporal convergence study could be of interest as the focus has been set on mesh refinement and the maximum Courant number.

OpenFOAM and equivalent OpenFAST surge, heave, and pitch simulations were then performed, and a P-Q analysis was performed on each simulation separately. For surge, it was first found that OpenFAST had an almost perfect correlation for low amplitudes, which diverged a little for higher amplitudes, while data points stemming from the OpenFOAM simulations were scattered at first. The origin appears to stem from the different equilibrium positions towards which the floaters from different meshes converge. Assuming a linear correlation for the P-Q analysis, finding the equilibrium position that differed by a maximum of 5cm became possible. Future work could try to do a similar study on data that the OC7 campaign has just released.

After the optimization was done for all decay tests, one can conclude that generally, OpenFAST and OpenFOAM coincide in modeling the correct frequencies. OpenFAST, however, both underestimated the linear and quadratic coefficients, which is coherent with the findings of OC6 on the DeepCWind floater. This is mainly due to the viscous effects modeled in OpenFAST through simple tuning to get the quadratic damping coefficients. There is also an underestimation of the linear damping coefficients due to the modeling through a potential flow solver. The OpenFOAM simulations showed that the mooring theory influences the P-Q analysis, especially for the 5m surge decay test, which the difference in mooring modeling could explain. This uncertainty could be solved by using the same mooring line model `MoorDyn` in OpenFOAM and further identifying the differences between OpenFAST and OpenFOAM hydrodynamic modeling. The heave and pitch decay tests showed similar trends but differed from the surge decay tests. OpenFAST simulations underestimated both linear and quadratic damping coefficients.

Recommendations would be to tune the viscous damping matrix in OpenFAST better using another solver like `waves2foam` and use the strip theory to better account for linear damping. Furthermore, if this is insufficient, one could add additional damping in OpenFAST. It has to be noted, however, that tuning these coefficients is not an easy task and might be valid for free decay tests, but it differs from CFD simulations/experiments in met ocean conditions. Another action could be to modify the OpenFAST setup to include second-order platform forces in the model while still considering water. These changes may seem incompatible at the moment of writing.

Finally, possibilities for validation have been explored, and strategies have been laid out to validate this numerical setup with experimental campaigns, either with the Plymouth experiment or using data from the FOCAL campaign that feeds the OC7. An elementary mooring theory must be developed to show the differences in hydrodynamic modeling further.

To conclude, `waves2foam` and `Moody` for the hydrodynamic and mooring modeling has been used to build a robust setup. This setup can capture more significant motions while maintaining reasonable decay test convergence tests. This underscores the importance of using computational fluid dynamics (CFD) to enhance mid-fidelity models like OpenFAST.

4

Aerodynamic verification of the 15MW wind turbine

This chapter aims to validate the implementation of the IEA 15MW wind turbine model in OpenFOAM to be used in future coupled motions analysis. The purpose of this section is also to emphasize the differences between the setups in OpenFAST and OpenFOAM. A detailed description of the underlying physics is provided in Pere Frontera Pericàs [81]. An overview of the relevant literature on this large turbine is presented in section 4.1, along with further discussion on Actuator Line Modeling (ALM) and its applications. The IEA 15MW wind turbine is introduced in section 4.2. Subsequently, the numerical configurations for both OpenFOAM and OpenFAST simulations are outlined in section 4.3. The results encompassing steady-state and prescribed motion simulations are analyzed in section 4.4. Finally, key conclusions are drawn in section 4.5.

4.1. Litterature review

4.1.1. Differences between fixed wind turbines and FOWT

Sebastian and Lackner [99] highlight that offshore floating wind turbines' flow field is more complex than conventional offshore turbines due to the increased degrees of freedom (DOFs) in floating systems. These additional DOFs can cause unsteady aerodynamic loading, making traditional methods like BEM theory insufficient. Accurate aerodynamic load estimates for these turbines require more advanced modeling techniques to effectively handle unsteady, skewed, and shear transitional flows at high tip speed ratios. In the context of floating wind turbines, the effect of the moving platform is twofold. First, the flowfield around the rotor is modified [107] [13], causing differences in the relative wind speed, for example. Second, it is also possible that in case of severe sea states, the blades enter their wake affecting the structural dynamics and the wake behavior [84][17].Sebastian and Lackner [99] have pointed out that surge and pitch motions combined with high TSR could result in four different working states: windmill state, turbulence state, vortex ring state, and propeller state. their description can be found in [99] and [25]. In these cases, engineering models based on BEM might not be applicable anymore, especially when large motions are considered. Studies have found no agreement on whether BEM can still be used [107], especially when platforms with possible large motions, such as semi-submersible, are considered. There is broad agreement that the motion of FOWTs should enhance wake mixing and recovery, which would be advantageous for downstream turbines and could permit a reduction in rotor spacing [39].

The latter motions can make FOWT behave in four different conditions as depicted in Figure 4.1. In the windmill state, the turbine efficiently extracts energy from the wind, following the principles of BEM, with both the tip-speed ratio (TSR) and reduced frequency remaining relatively low. As TSR increases, the turbine enters the turbulent wake state, where blade-wake interactions cause a turbulent region to form behind the rotor. This state occurs when the axial induction factor falls between 0.5 and 1, and engineering corrections, such as Glauert's, are used to account for the associated aerodynamic

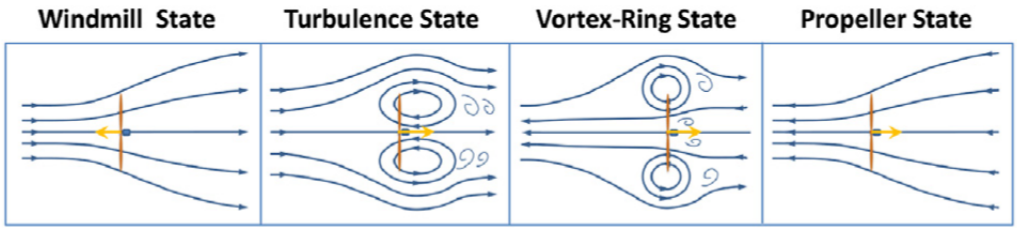

Figure 4.1: The four working states of floating wind turbines from [25]

effects. At even higher TSR, the turbine transitions into the vortex ring state. At this point, a circular flow pattern forms around the rotor, causing the airflow to become unstable and irregular [25]. This results in alternating forward and backward velocities across the rotor plane, leading to significant fluctuations in thrust and power and increased fatigue on the blades due to energy dissipation in the vortex ring. Eventually, the turbine reaches the propeller state at a sufficiently high TSR, where the relative wind speed reverses. In this state, the wake reverses direction, resulting in negative angles of attack and thrust, causing the turbine to impart energy into the flow, effectively behaving like a propeller.

Fang et al. [31] investigates the impact of surge motion on the rotor aerodynamics and wake of a 1:50 scale FHAWT using CFD with improved detached eddy simulations. The results indicate that even small surge motions can significantly affect rotor thrust, torque, and power. Surge amplitude and period influence these fluctuations, with increased relative wind speeds leading to dynamic stall near thrust and torque peaks. Surge motion also enhances average rotor power, with amplitude and frequency contributing to this increase. In the near wake, rotor-wake interaction improves aerodynamic performance, while more robust, concentrated root vortices are observed.

Proper wake modeling is also crucial, as the motion of a wind turbine's wake, often called wake meandering, impacts both fatigue loading and the power output of downstream turbines [123]. The latter offers a comprehensive analysis of previous studies on wake meandering, focusing on its origins and characteristics. One crucial aspect is predicting the distance wind velocity returns to normal. The wake is defined by a decrease in velocity and various swirling structures that continue to affect velocity recovery even after they dissipate. This makes tip vortices especially interesting. While significant research has been conducted on tip vortices shed from fixed-bottom turbines, the analysis and modeling of wakes become more complex with floating offshore wind turbines (FOWTs) due to platform motion, which alters the rotor's aerodynamic response.[68] evaluated the effectiveness of the Actuator Line Method (ALM) in simulating tip vortex effects using a NACA0018 wing. The analysis used three different kernel shapes to compare high-fidelity blade-resolved CFD, standard ALM, and ALM with spanwise force data (frozen ALM). The study concluded that it is crucial to reduce force smearing and angle of attack sampling near the tip in the ALM framework as interaction scales decrease towards the blade extremity. The study found that ALM tends to produce a more diffused vortex than blade-resolved CFD, leading to an underestimation of vortex intensity and downwash while overestimating vortex aging in the far wake. This discrepancy may be due to limitations in the ALM formulation or inherent differences between ALM and CFD. Overall, the findings underscore the need to improve ALM formulations to capture tip vortex dynamics better.

This complexity results in noticeable differences between the wakes of fixed-bottom and floating turbines. For instance,Arabgolarcheh, Jannesarahmadi, and Benini [2] used an actuator line model (ALM) CFD approach to demonstrate how platform surge and pitch motions introduce periodic changes in tip vortex strength, leading to a highly unstable wake and faster velocity recovery. Similarly, Ramos-García et al. [84] analyzed the wake shed from a FOWT under imposed surge and pitch motions, finding that different motion frequencies alter the near-wake vortical structures. However, wake recovery is not significantly affected by surge motion.

4.1.2. Experimental campaigns and validation campaigns

The UNsteady Aerodynamics for Floating Wind (UNAFLOW) is an EU-IRPWIND experimental campaign aimed at studying the unsteady aerodynamics of floating wind turbines, with a focus on advanced

aerodynamic modeling of multi-megawatt floating rotors [32]. A comprehensive dataset was generated through wind tunnel experiments involving harmonic motions in the surge direction, capturing local airfoil performance and overall rotor performance variables. This experimental data was then used to validate three different tools of varying fidelity: Blade Element Momentum (BEM), lifting line, and Computational Fluid Dynamics (CFD).

Phase III of the OC6 campaign will be discussed here, as phases I and II were briefly covered in the earlier sections and Scarlatti's Msc. thesis [98]. The OC6 Phase III campaign uses the results of the UNAFLOW campaign. The first part of the campaign concentrated on validating the aerodynamic loading on a wind turbine rotor experiencing substantial motion induced by a floating support structure [7]. The second part of OC6 Phase III focuses on the analysis of the wake itself [17].

During the first part of OC6 Phase III, a scaled model of the DTU 10 MW RWT was used to study system responses under steady and unsteady wind conditions. The results from various numerical models were compared with experimental data from Politecnico di Milano, showing good agreement for platform surge and pitch motions between the different models of varying fidelities during the forced experiments. The aerodynamic rotor load was linearly proportional to the apparent wind, indicating a quasi-steady response. Additional tests revealed that variations in rotor speed and blade pitch, combined with platform motion, led to unsteady aerodynamic responses. Numerical models showed significant differences based on including dynamic inflow effects, with discrepancies in load variations. The study concludes that while unsteady aerodynamic models may not be necessary for predicting loads in simple turbine motions, realistic scenarios involving generator torque and blade pitch adjustments require these models for accurate predictions. The first phase has also been reproduced in some parts by Pere Frontera Pericàs [81]

During the second part of OC6 Phase III [7], CFD and FVM are used and compared to benchmark experimental data from Politecnico di Milano's wind tunnel where a 1:75 scaled model of the DTU 10MW reference wind turbine was mounted on a hexapod that imposed surge motions. For the fixed bottom case in the near wake, the effect of platform motion on tip vortices is analyzed using velocity fields obtained through particle image velocimetry (PIV), while in the far wake, the focus is on wake recovery, a crucial parameter for wind farm planning, using hot-wire anemometer (HWA) data. CFD actuator line model (ALM) simulations underpredict strength despite higher computational costs and overprediction of core radius in CFD ALM results, highlighting a limitation affecting wake modeling reliability. These findings show that properly tuned FVW methodologies can capture tip vortex behavior at a fraction of the cost of CFD methods. The differences increase even more for unsteady cases, highlighting the need for fine-tuning these models to validate them.

Dose et al.[26] developed a CFD framework of flexible wind turbine rotors using a fluid-structure coupled solver that combines OpenFOAM with their in-house structural solver BeamFOAM. Thanks to an efficient mesh transformation, the structural response of the NREL 5MW reference wind turbine is accurately modeled compared to available literature without a significant increase in computational complexity. Under frontal inflow, there are only minor deviations in power and thrust between rigid and deformable blades. However, there were substantial deviations with yawed inflow, suggesting that blade deformations could improve correction models for BEM tools based on entire rotor CFD simulations.

Ramos-García, Sessarego, and Horcas [82] investigated floating IEA Wind 15 MW reference wind turbine and its wake utilized the multi-fidelity vortex solver MIRAS, coupled with the finite-element solver HAWC2. Results from MIRAS-HAWC2 were compared with the lower-fidelity HAWC2-BEM method. Significant differences were noted, particularly at high wind speeds and regular wave conditions. Compared to LL methods, the BEM method over-predicted motion amplitudes by over 50%

Trigaux, Chatelain, and Winckelmans [109] investigated how blade flexibility affects the loads and wake of the large IEA 15 MW reference wind turbine [34]. Using a flexible actuator line method (ALM) integrated with the nonlinear structural solver BeamDyn, large-eddy simulations (LES) were employed to evaluate the unsteady aerodynamic forces on each blade and their impact on flow dynamics. In uniform flow, comparisons between the flexible ALM and OpenFAST's free vortex wake model showed similar force distributions and time-averaged loads. The ALM demonstrated that the impact of blade deformations on aerodynamic forces was more accurately captured compared to BEM models, which

indicated a need for higher-fidelity aerodynamic models. In a turbulent boundary layer, blade flexibility led to notable flaps and torsional displacements, reducing thrust by 14%

Ramponi, Amaral, and Viré [85] investigated how varying platform motions impact the aerodynamic power of floating wind turbines, considering uniform inflow and a rigid turbine. The analysis involves prescribed coupled motions, such as pitch-surge, pitch-yaw, and surge-yaw, with phase shifts between these motions. Key findings include that phase shifts in pitch and surge motions can either enhance or diminish power production, with phase opposition often being desirable. The yaw motion was found to be less significant in comparison. In the absence of a controller, increased amplitude and frequency of pitch-surge motions generally boost power production, though phase shifts can reduce potential gains. When the controller is active, increased motions lead to power losses due to the power limit in the above-rated regime. The results highlight that pitch and surge motions have a more substantial impact than yaw. Additionally, phase shifts between motions can positively affect power production by reducing regime transitions. Despite some simplifying assumptions, such as the absence of inflow turbulence, this study provides fundamental insights into the effects of coupled motions on power production. It sets a baseline for future research with more realistic conditions and higher fidelity methods.

Other research domains regarding aerodynamics are not mentioned here, such as the impact of turbulence on FOWT, dynamic stall modeling, or wind farm optimizations, but these topics are out of the scope of this thesis; interested readers can read a review made by Micallef and Rezaeiha [70].

4.2. IEA 15MW reference wind turbine

Table 4.1 provides key parameters for the IEA Wind 15-MW turbine, a bottom-fixed tower wind turbine designed to operate in IEC Class 1B wind conditions. It has a power rating of 15 MW with a specific rating of 332 W/m². The turbine features a large rotor with a 240-meter diameter and a hub height of 150 meters. It uses a low-speed, direct-drive drivetrain with variable speed and collective pitch control. The rotor, designed with an upwind orientation, has three blades made from the FFA-W3 airfoil series, each with a mass of 65 tons. The maximum rotor speed reaches 7.56 rpm, with a tip speed of 90 m/s. The entire rotor-nacelle assembly weighs 1,017 tons, supported by an 860-ton tower and a monopile foundation embedded 45 meters deep into the seabed, with a monopile mass of 1,318 tons.

Parameter	Units	IEA Wind 15-MW Turbine
Power rating	MW	15
Turbine class	-	IEC Class 1B
Specific rating	W/m^2	332
Rotor orientation	-	Upwind
Number of blades	-	3
Control	-	Variable speed Collective pitch
Cut-in wind speed	m/s	3
Rated wind speed	m/s	10.59
Cut-out wind speed	m/s	25
Rotor diameter	m	240
Airfoil series	-	FFA-W3
Hub height	m	150
Hub diameter	m	7.94
Hub overhang	m	11.35
Drivetrain	-	Low speed Direct drive
Design tip-speed ratio	-	9.0
Minimum rotor speed	rpm	5.0
Maximum rotor speed	rpm	7.56
Maximum tip speed	m/s	90
Gearbox ratio	-	-
Shaft tilt angle	deg	6
Rotor precone angle	deg	-4.0
Blade prebend	m	4
Blade mass	t	65
Rotor nacelle assembly mass	t	1,017
Tower mass	t	860
Tower base diameter	m	10
Transition piece height	m	15
Monopile embedment depth	m	45
Monopile base diameter	m	10
Monopile mass	t	1,318

Table 4.1: Key Parameters for the reference IEA Wind 15-MW Turbine with bottom fixed tower [1]

Table 4.2 outlines the blade properties of the IEA 15-MW wind turbine, emphasizing its key dimensions and performance characteristics. Each blade is 117 meters long, with a root diameter of 5.20 meters and a maximum chord of 5.7 meters located 27.2 meters from the root. The blade has a tip prebend of 4 meters and a precone angle of 4 degrees. Weighing 65,250 kg, the blade's center of mass is positioned 26.8 meters from the root. The design tip-speed ratio is 9.0, while the first flapwise and edgewise natural frequencies are 0.555 Hz and 0.642 Hz, respectively. Additionally, the blade's design power coefficient (C_P) is 0.489, and its thrust coefficient (C_T) is 0.799. The turbine generates an annual energy production of 77.4 GWh.

Description	Value	Units
Blade length	117	m
Root diameter	5.20	m
Root cylinder length	2.34	m
Max chord	5.7	m
Max chord spanwise position	27.2	m
Tip prebend	4.00	m
Precone	4.00	deg
Blade mass	65,250	kg
Blade center of mass	26.8	m
Design tip-speed ratio	9.00	-
First flapwise natural frequency	0.555	Hz
First edgewise natural frequency	0.642	Hz
Design C_P	0.489	-
Design C_T	0.799	-
Annual energy production	77.4	GWh

Table 4.2: Blade Properties of the IEA 15MW wind turbine [1]

4.3. Numerical setup for steady conditions

This section aims to describe the numerical setups for the different simulations. First, steady simulations are done at constant wind speed and compared to OpenFAST by [10]. Then, we can confirm that the ALM model correctly captures steady-state loading. Then simulations of the upstream turbine were carried out for a prescribed surge motion of 15m amplitude and frequencies of 0.01419 (typical surge), 0.02441 (typical pitch), 0.05676 (typical storm sea state), and 0.11352Hz (typical sea state) [84]. These simulations aim to describe the differences between a higher fidelity CFD model and the BEM model used in OpenFAST.

4.3.1. Assumptions

At first, we assumed the turbulence intensity to be 5%, which is typical for offshore wind applications. After the first simulations, however, uniform and steady wind was used to have fewer uncertainties in the mean values calculated during the simulations. Neither wind shear nor veer is modeled. To effectively compare turbulent wind simulations between OpenFAST and OpenFOAM, an ideal approach would be first to perform the simulation in OpenFOAM, extract the wind field from a plane positioned at the start of the actuator zone in front of the rotor, and then use this data as input for the OpenFAST simulations. This approach was not used due to time constraints, but it could be a valid method for future work.

Then, we assume that there is no tower to simplify the model and focus on the differences due to the blade modeling. Due to limited data on the airfoil polars for different Reynolds, the ALM, and the BEM models use single Reynolds tables to model the blade loading. To the author's knowledge, some campaigns, like the UNAFLOW campaign, had data available, which is not the case for the IEA 15MW turbine.

Root-tip correction models are kept in OpenFOAM and OpenFAST, but further work could test the effect of not taking them into account in OpenFOAM. A more detailed discussion is presented in subsection 4.3.5. Furthermore, neither a dynamic stall nor an inflow model is used. Results from the UNAFLOW projects [32] have shown that the motion of the turbine does not imply modeling unsteady aerodynamics to predict the loads on the turbine. Still, it is relevant when control is included.

Both simulations rely on look-up tables, thus using a static polar approach. An inherent limitation of this method is that the Reynolds numbers change during the simulation due to dynamic inflow, changing the profile's loft and drag coefficients. An additional uncertainty is due to the initial calculations of the polar tables, which rely on simulations rather than experiments.

4.3.2. Turbulence modelling

In the continuity of the above-presented literature [75][10] [111], the $k-\omega SST$ turbulence model is used, instead of the $k-\epsilon$ turbulence model used in the thesis of Pere Frontera Pericàs [81]. This formulation blends in $k-\omega$ near walls and the $k-\epsilon$ model in the far field. Even though $k-\epsilon$ is computationally more effective in these conditions, since the boundary layers are not of interest, using the latter model has been deemed more coherent. It will also be used for coupled motions analysis when the boundary layers of the floater are of significant importance. This model is particularly suited for simulating flow away from boundary layers, as it assumes a balance between the production and dissipation of turbulence. When using this model, it is necessary to solve two additional differential equations: one for the turbulence kinetic energy k and another for the turbulence dissipation rate ϵ. The constants required for these equations are set to their default values in the RAS section of the `turbulenceProperties` dictionary in OpenFOAM.

4.3.3. Domain

The domain size was investigated and chosen based on the available literature. Domain dimensions vary across studies depending on the simulation characteristics. For instance, Oliveira et al. [75] used a relatively small domain of $(5 \times 3 \times 3)D$ to analyze the temporal discretization of a fully resolved IEA 15MW model, resulting in almost 36 million cells. Arabgolarcheh, Jannesarahmadi, and Benini [2] employed a $(10 \times 3 \times 4)D$ domain for URANS-ALM simulations, which allowed them to analyze the wake and its decay. In contrast, Trigaux, Chatelain, and Winckelmans [108] utilized a cubic domain with a side length of $12D$ and a blockage ratio of 0.5%, enabling comparison of LES-ALM calculations with OpenFAST, which does not account for the presence of walls. When not making comparisons, they used a $(12\times4\times4)D$ domain. Similarly, Wang et al. [112] used a $(21\times8\times8)D$ parallelepiped to account for full flow development using the overset meshing technique. Campaña-Alonso, Ferrer, and Méndez-López [10] also considered a domain width of $10D$ for URANS-ALM simulations with turbinesFoam.

For computational reasons, it was decided to keep the domain width and height to $6D$, which allows for a sufficiently small blockage ratio. The domain length is set to $10D$, as the wake characteristics will not be analyzed in detail. The cell aspect ratio increases towards the x and y boundaries to further reduce the cell count. However, a constant cell aspect ratio is maintained within the region $x \in [-2D, 4D]$, $y \in [-1.5D, 1.5D]$, and $z \in [-1.5D, 1.5D]$.

Based on previous literature, the refinement strategy has been chosen as follows:

- The finest refinement region is a cylindrical area centered around the turbine. This cylinder has a base radius of $1.5R$ and a length of $1D$, with the turbine at the center. Within this region, particularly around the blade, the desired cell width is set to $\Delta x_3 = D/128 = 1.875m$, which has shown accurate results in similar setups [103].
- For the near wake, a cylindrical refinement region is employed with a radius of $2R$, spanning from $x \in [-0.5D, 5D]$ along the streamwise direction. The cell size in this region is twice as coarse as that in the turbine region.
- The turbulence zone is defined as a rectangular box extending from $x \in [-1.5D, 7D]$ and $y, z \in [-2D, 2D]$ and is four times as coarse as the turbine region.

For the cases with prescribed motion, the boundaries of the rotor zone are enlarged in both x directions. These parameters are also similar to the ones used by C. Dos Santos Pereira Malveiro [9] in his MSc. Thesis when he was doing his refinement study. To simplify the problem and reduce computational costs, the boundary layer region near the walls will not be simulated.

4.3.4. ALM modelling

Spyropoulos et al. [103] have found that the number of blade elements modeled did not add additional computational complexity and have recommended that $\Delta r \leq 3 \times \Delta x$, an increased refinement did not affect much the precision on the power output of the turbine. In this model, 50 actuator points are chosen per blade, meaning $\Delta r = 117/50 = 2.34m$ on average. This means that there is one AE for every $\simeq 1.25$ grid elements, which fall under the recommendations of literature [103]. For simplicity's sake, we also assume that there is no pre-bending of the blades, shaft tilt, or precise angle. This section aims to compare the aerodynamic loads with the literature and verify the correct implementation of

the turbine setup, which will go to coupled simulations later. The smearing factor is the same as the one described in Equation 2.1.3. It could be interesting to analyze its influence more in detail since changes can be hardcoded, but it is out of the scope of our analysis. Also, the nacelle is not included in the analysis. However, it is assumed to affect rotor loads in a minor way. Tower loads are also not included; its implementation could affect the wake, but its analysis is out of this project's scope. More information can be found in Wang, Zhou, and Wan [117] and Santo et al. [97].

4.3.5. On the inclusion of hub and tip loss factors

The tip loss factor refers to a correction applied in aerodynamic models, especially those using Blade Element Momentum (BEM) theory, to account for the reduced efficiency of blades near their tips. This factor is crucial in wind turbine modeling, as the flow around the blade tips differs from the rest of the blade due to three-dimensional effects like vortex shedding, which reduces the local lift and thrust forces.

Near the blade tips, the air from below the blade tends to spill over to above the blade, leading to a flow detachment and a swirling flow at the blade tip. This flow and the continuous rotation of the blade lead to the helical structure. This flow detachment leads to a loss of lift near the blade tips and practically to a reduced thrust and torque. Since steady-state or simplified simulations like BEM theory do not model the flow around the blade, corrections such as Prandtl's tip loss factor are applied to account for the loss of efficiency near the blade tip.

Even though ALM simulations in OpenFAST simulate the flow, these simulations simplify the turbine blades as actuator lines and do not resolve the tip vortices exactly, thus theoretically needing correction factors as well. However, it is believed that the tip loss factors are naturally simulated by flow modeling. The impact of their inclusion is out of the project's scope and would probably include a test against an experimental campaign such as the one performed during the UNAFLOW project [32].

4.3.6. Temporal discretisation

Generally, it is recommended to have good accuracy of the simulations to have a CFL number of 1, meaning that the tip of the blade does not jump over a simulation cell during one timestep. Mathematically, this means :

$$\Delta_t = \frac{\Delta x}{U_{tip}} \tag{4.1}$$

However, the conditions are stricter to reach a correct number of 0.9. The timestep is set to a fixed one for the steady wind turbine.

4.3.7. Boundary conditions

Field	**Inlet**	**Outlet**	**Walls & Atmosphere**
Velocity (U_x)	fixedValue, U_x	inletOutlet, U_x	slip, (0 0 0)
Pressure	zeroGradient	fixedValue, 0	zeroGradient
Turbulent Kinetic Energy (k)	fixedValue, k	fixedValue, k	fixedValue, k
Specific Dissipation Rate (ω)	fixedValue, ω	fixedValue, ω	fixedValue, ω

Table 4.3: Summary of boundary conditions for each field.

The boundary conditions are set as the following :

- **Velocity Field (U_x)**: The internal field is uniformly set to $(U_x, 0.0, 0.0)$. A fixed value boundary condition is applied at the' inlet', matching the internal field value. The 'outlet' uses an 'inletOutlet' boundary condition, allowing flow to leave the domain with the internal field as the default value and specifying a zero velocity for incoming flow. Walls and the atmosphere are treated with a 'slip' condition, where the velocity parallel to the wall is not constrained, reflecting a frictionless boundary.

- **Pressure Field**: The internal field is initialized to 0.0. The ‘inlet‘ boundary is defined as a ‘zeroGradient‘ condition, allowing pressure to adjust based on internal conditions. The ‘outlet‘ applies a ‘fixedValue‘ condition, setting the pressure to the internal field value. Similarly, the walls and atmosphere boundaries also employ a ‘zeroGradient‘ condition, ensuring no pressure gradient across these surfaces.
- **Turbulent Kinetic Energy (k)**: The turbulent kinetic energy is set with a uniform internal field, where the value is calculated as $k = 1.5 \times (I \times U_x)^2$, with I representing the turbulence intensity and U_x the incoming velocity. The boundary conditions for k are set as ‘fixedValue‘ for all boundary types, using the internal field value.
- **Specific Dissipation Rate (ω)**: The specific dissipation rate is also defined uniformly, calculated using $\omega = \frac{\sqrt{k}}{0.09^{0.25} \times \text{chord}}$, where ‘chord‘ represents a characteristic length scale, such as a blade chord length in wind turbine simulations. A ‘fixedValue‘ condition is used for all boundaries, ensuring that ω is consistent with the internal field.
- **Additional Fields**: Other fields, such as the pressure gradient and any additional turbulence parameters, are initialized with ‘calculated‘ or ‘fixedValue‘ boundary conditions across the ‘inlet‘, ‘outlet‘, ‘walls‘, and ‘atmosphere‘, depending on their nature, ensuring consistency across the domain.

This setup defines a complete and consistent set of boundary conditions for a turbulence simulation. It is particularly suited for modeling external aerodynamics, with attention to accurately capturing inflow turbulence and flow behavior at boundaries.

4.3.8. Solver settings

In this simulation setup for modeling the IEA 15MW wind turbine in OpenFOAM using the Actuator Line Method (ALM), the PIMPLE algorithm is employed, which is a hybrid of the SIMPLE and PISO algorithms, which is operating in PISO mode for these simulations. The `momentumPredictor` is set to `false`, indicating that no initial prediction for the velocity field is made before the correction steps, typically done to improve stability and computational time. It is recommended to be set to yes for transient simulations and more complex flows. The `correctPhi` is set to `no`, meaning that the mass fluxes are not corrected after velocity updates, which could be acceptable if the primary focus is not on precise mass conservation or the flow is relatively stable. It should be set to yes for dynamic meshes or transient simulations; however, it has been set to no due to computational reasons. The assessment of its impact could be part of a future study. The `nOuterCorrectors` is set to `1`, meaning there is a single outer loop iteration per time step, ensuring the overall convergence of the solution within each time step. The `nCorrectors` is set to `3`, indicating that three corrector steps are performed within each time step to improve the pressure-velocity coupling, which is crucial for accurately capturing the unsteady aerodynamic effects. Additionally, `nNonOrthogonalCorrectors` is set to `1`, ensuring one correction iteration to address non-orthogonality in the mesh, which helps maintain accuracy in complex geometries. It can be set higher if complex geometries, such as the floater, are involved in the simulations. Finally, `turbOnFinalIterOnly` is set to `false`, meaning turbulence is resolved during every iteration, which could be necessary for accurately capturing the detailed turbulent structures around the turbine. This configuration is tailored to balance accuracy and computational efficiency while modeling the dynamic behavior of the IEA 15MW wind turbine.

4.3.9. OpenFAST modelling

OpenFAST simulations have been performed, and the standard setup has been modified to match the OpenFOAM setup. Since turbulence is modeled within OpenFOAM through the $k - \omega SST$ turbulence closure model, Turbsim is used to model turbulence within OpenFAST. There is no wind shear to avoid differences in modeling, as there is no veer. The rotor speed is constant, no control is included, and the rotor rotates to match the ideal tip speed ratio below rated conditions. The air density is kept constant in both simulations at $1.225 kg/m^3$. Despite all these approximations, a comparison was made to assess the differences between the two simulation methods.

4.4. Results

4.4.1. Method of analysis

The method of analysis used in this code focuses on detecting the convergence of a time-dependent variable, the power coefficient c_p, from wind turbine data by analyzing the gradient behavior over time. The main steps include:

- First, a moving average filter is applied to smooth the selected variable, reducing noise due to turbulence and modeling and highlighting the underlying trends. The window used is 100 timesteps, i.e., one second, thus still maintaining the effect of turbulence in the wind.
- The gradient of the smoothed data is then calculated with respect to time. Since the gradient oscillates around zero when converging due to turbulence, the mean gradient is computed over sliding time windows of 60 seconds to see the trend.
- The code searches for the first point where the mean gradient remains consistently below a given threshold; for this analysis, $5.10^{-}5$ has been chosen, indicating convergence of the variable towards a steady state.

Combining these steps provides a systematic way to detect and quantify the steady-state behavior of wind turbine variables based on time-series data.

Regarding the prescribed motion simulations, the analysis is done over a time window when the steady state is reached, defined by simulation times above three periods. For consistency reasons, the three last periods of the simulations are considered and averaged together to perform the prescribed motion analysis.

4.4.2. Steady inflow

Influence of the turbulence intensity

As described above, turbulence intensity should not significantly impact the mean loads and c_p since these are averaged values. However, turbulence intensity influences wake development, which is beyond this project's scope. Here, the effect of turbulence intensity is studied.

The results are shown in Table 4.4. For the different wind speeds, the differences in thrust and c_p are minimal (less than 0.6%). Therefore, it can be assumed that the difference in turbulence modeling in OpenFOAM plays a minor role. However, as will be seen in future analysis, the definitions of the turbulence intensity in OpenFOAM and OpenFAST seem to differ. Here, the wind looks more uniform without any turbulence. In contrast, the wind is considered constant for the rest of the analysis; as a more thorough investigation is out of this project's scope, the continuous and uniform wind will be used in all the following simulations, as explained in subsection 4.3.1.

Wind speed [m/s]	TI (OpenFOAM) [%]	c_p [-]	Thrust [N]	Convergence Time [s]
8	2	0.5320	1,168,559.944	163.23
	5	0.5295	1,166,391.773	167.68
10.59	2	0.5313	2,046,571.558	138.46
	5	0.5289	2,042,962.485	139.73

Table 4.4: Influence of turbulence modeling in OpenFOAM

Regarding the post-processing of this analysis, it is important to note that different thresholds and time windows yield different results. Figure 4.2a shows the analysis of the steady-state wind case at 10.59 m/s with a turbulence intensity of 5%, using a 1-second averaging window for c_p. When the averaging window is increased to 10 seconds, the results are shown in Figure 4.2b. Larger fluctuations due to turbulence are significantly reduced by averaging, leading to smoother results. Additionally, there is a period where the gradient fluctuates more around zero, which could serve as another threshold criterion for future work.

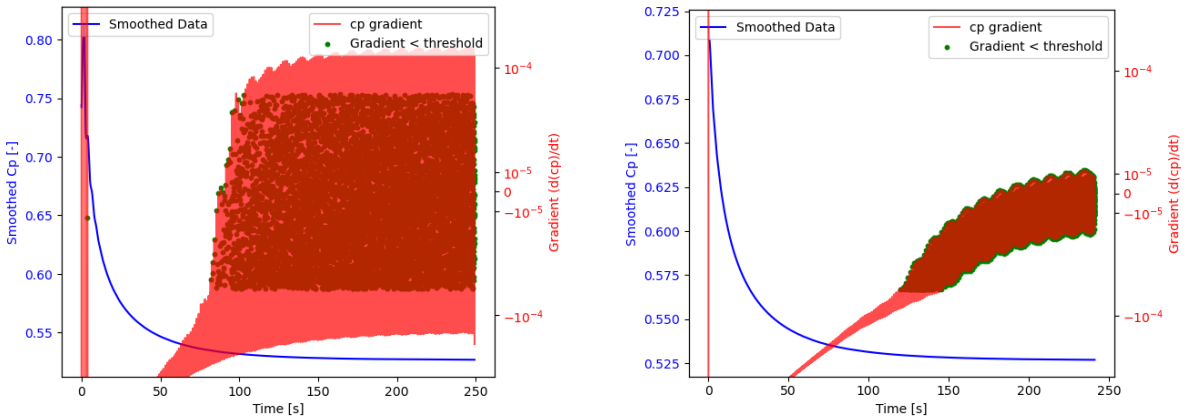

Figure 4.2: Convergence for a wind turbine operating at a steady wind speed of 10.59 m/s and 5% turbulence intensity in OpenFOAM, with a time averaging over 1 second (a) and 10 seconds (b) respectively

Comparison between OpenFOAM and OpenFAST

OpenFAST and OpenFOAM simulations are run for the same inflow conditions, and different metrics are compared.

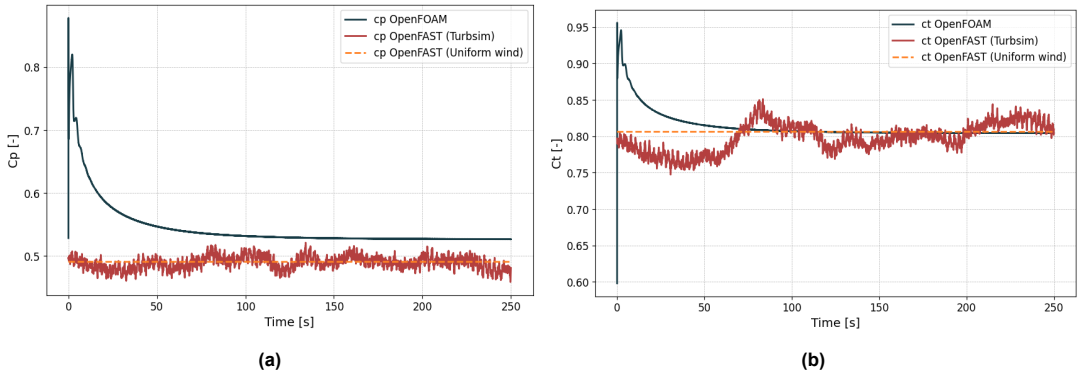

Figure 4.3: Comparison of power and thrust coefficients of the IEA 15MW wind turbine in a steady state with a 10.59 m/s uniform wind in (b) (a) respectively in OpenFOAM and OpenFAST.

From Figure 4.3a, one can see that the power coefficient in the OpenFAST simulation using Turbsim fluctuates more because the wind is much more fluctuating. Since the wind fluctuations are coming from the turbulence intensity, this shows that the turbulence modeled in OpenFOAM is not the same and resembles more uniform wind, so uniform wind conditions will be used in OpenFAST to compare with OpenFOAM in all future simulations. This shows that it is probable that in OpenFOAM, the input is not an absolute value and not in percentage as thought written in previous Msc. of Pere Frontera Pericàs [81] and Scarlatti [98].

From Figure 4.3b, it can be seen that the thrust coefficients are very close to each other. In his MSc, these results have also been found by C. Dos Santos Pereira Malveiro [9]. Thesis. The tip speed ratio and the turbine speed are the same in both simulations as shown in Table 4.5. The thrust, however, differs between 1 and 2%, suggesting differences in relative velocities between the two approaches. As can be observed in Figure 4.5a, slight differences are evident at the blade's root and tip. The discrepancy may be attributed to the correction models utilized in OpenFAST, which inadequately account for the thrust loss at the blade tip. Removing these correction factors resulted in an increase in thrust to $2.58MN$ in OpenFAST. Furthermore, the ALM simulation is imperfect, as the refinement study may reveal inaccuracies due to numerical errors.

In Figure 4.3a, it can be observed that there is a significant mismatch between the two power coeffi-

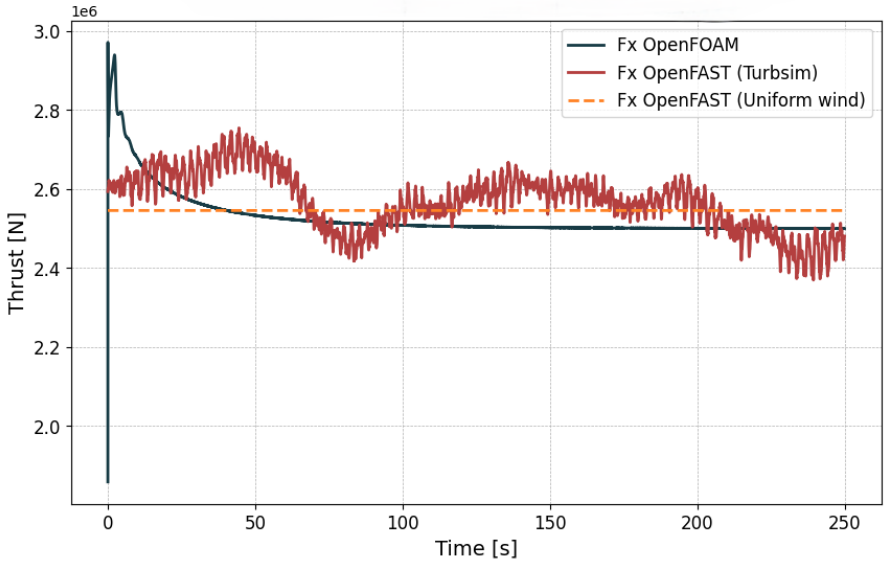

Figure 4.4: Comparison of turbine thrust in steady-state conditions with 10.59 m/s uniform wind between OpenFOAM and OpenFAST

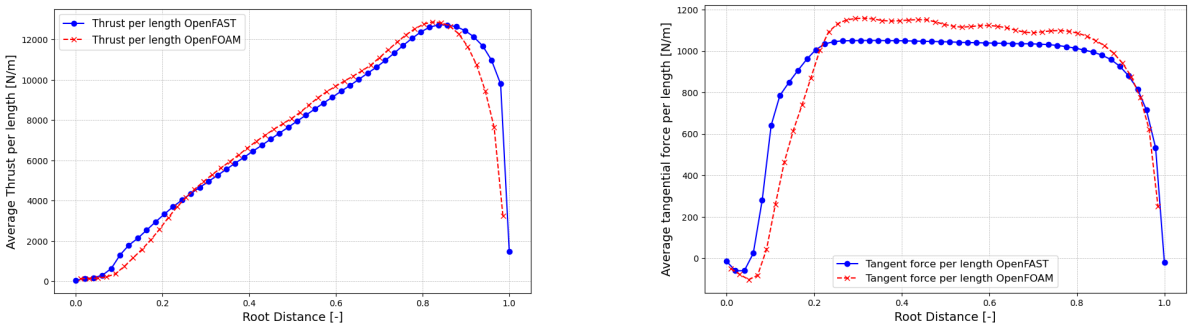

(a) (b)

Figure 4.5: Comparison of the thrust (a) and tangential force (b) per unit length of a single blade in steady-state conditions with 10.59 m/s uniform wind between OpenFOAM and OpenFAST

cients. More specifically, Figure 4.5b shows that the tangential force is underestimated in OpenFAST for over 80% of the blade span. Since the tangential force is the source of torque, the higher in-plane force in OpenFOAM explains the overall overestimation of the power coefficient. The underestimation of forces in the mid-section of the blade can be attributed to the different angles of attack, as illustrated in Figure 4.6a. Given that the rotational speed is nearly the same in both simulations, the difference arises from OpenFAST underestimating the angle of attack across all blade sections. This discrepancy stems from OpenFAST overestimating the velocity deficit at the rotor plane. The axial velocity at the rotor plane is shown in Figure 4.6b. OpenFAST is calculated using $U_x = (1 - a) \cdot 10.59$, which explains why the velocities are inaccurate at the blade root and tip. In regions where the tangential force is most significant, it can be noted that the velocity deficit is overestimated in OpenFAST. This is because the deficit is computed using the Blade Element Momentum (BEM) theory, which does not explicitly model the induction zone contrary to ALM.

These results have also been observed in [9], where various metrics were compared among a BEM model, an FVW model, and an ALM model. He explained that since the power coefficient is based on wake calculations, the different wake methods could lead to more differences in the power coefficient than in the thrust coefficient. BEM underestimates the reduction in axial velocity because it can not calculate the effect of the wake. In contrast, the ALM method calculates the wake of the blades to calculate the power coefficient. A more detailed study of that underestimation is out of the scope of

this study. However, the overestimation of the ALM simulation compared to OpenFAST could also be found in Trigaux, Chatelain, and Winckelmans [108].

Mean wind speed	Software used	Thrust [N]	c_p [-]	c_t [-]	TSR [-]	Ω_{rot} [rpm]
8	OpenFOAM	1.43 E+6	0.527	0.804	9	5.726
	OpenFAST	1.45 E+6	0.491	0.806	9.04	5.73
10.59	OpenFOAM	2.50.E+6	0.527	0.804	9	7.581
	OpenFAST	2.55.E+6	0.491	0.806	9.04	7.585

Table 4.5: Comparison between OpenFAST and OpenFOAM for steady and uniform wind simulations

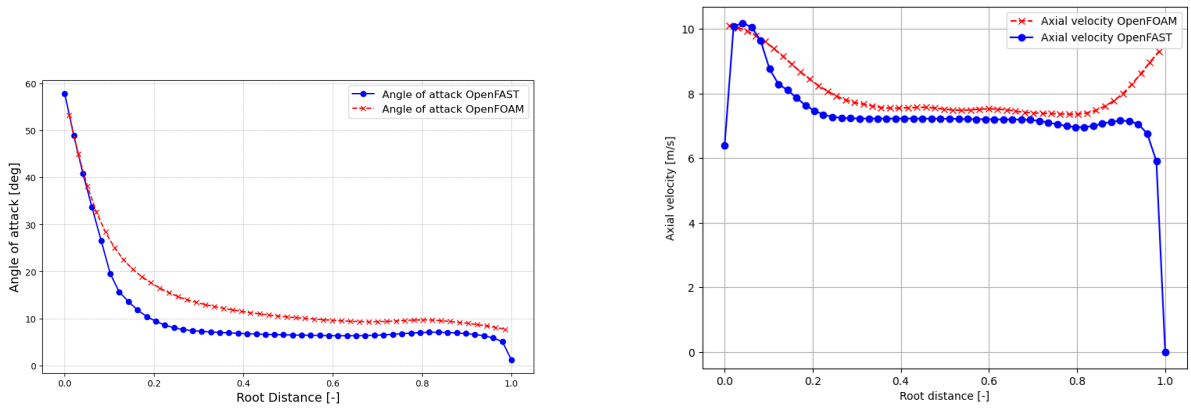

(a) (b)

Figure 4.6: Comparison of angle of attack and axial velocity for the same case study as above, in steady-state conditions with 10.59 m/s uniform wind between OpenFOAM and OpenFAST

4.4.3. Prescribed motions

The movement of the floating turbines also makes the thrust and the power vary over a cycle. To see the effects this has on the mean loads encountered, three simulations have been carried out for a prescribed surge motion of 15m amplitude and different frequencies, as it was done by Ramos-García et al. [83]. This section aims to verify that the current setup matches the literature for prescribed motions, where the aerodynamic considerations and approximations are below their range of validity. No control is implemented in these simulations.

- $f = 0.01419Hz$ for a typical surge frequency
- $f = 0.02441Hz$ for a typical pitch frequency
- $f = 0.05676Hz$ typical storm sea state

A fourth frequency was modeled in the study of Ramos-García et al. [83], f=$0.11352Hz$; however, this simulation was left out due to time constraints. The chosen wind speed is $10.59m/s$, which is just below rated conditions, at a high tip speed ratio, where the discrepancies between the two models are expected to be the most important. The inflow wind is modeled as laminar.

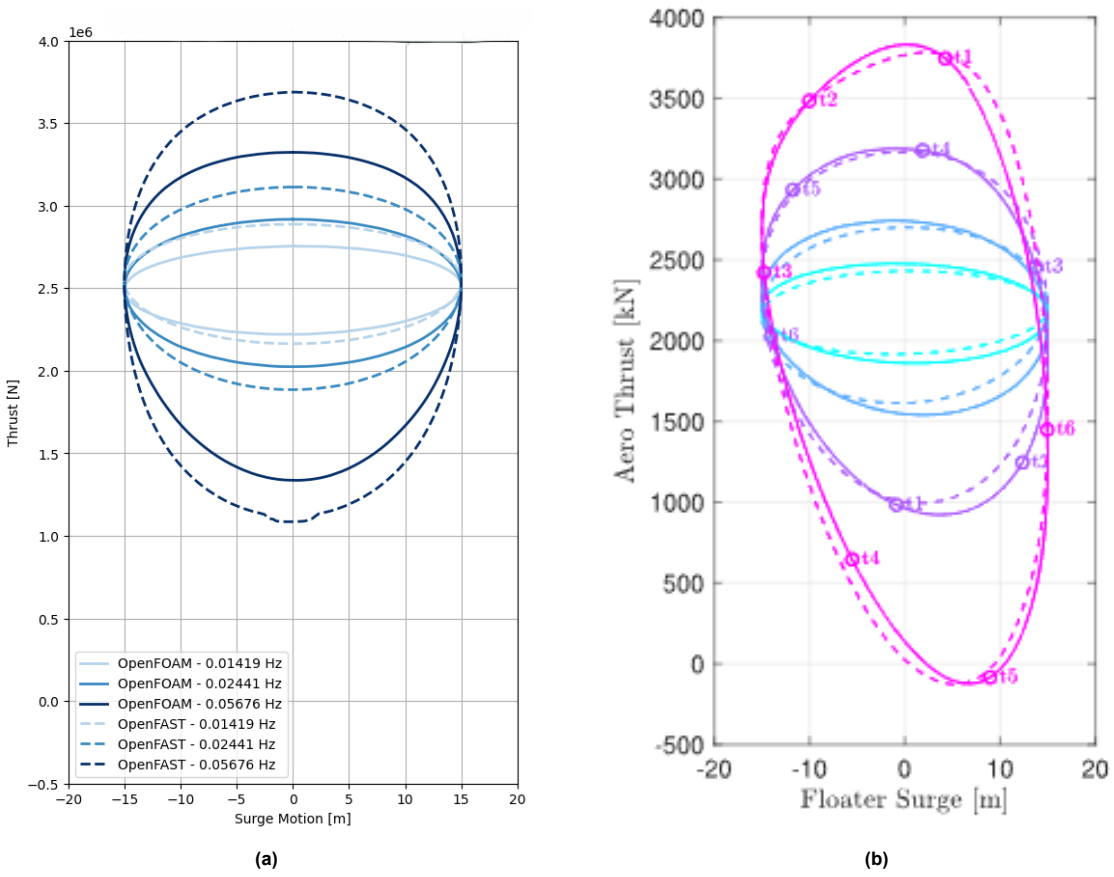

(a) (b)

Figure 4.7: Thrust comparisons during prescribed motion: (a) shows the average thrust over four cycles, while (b) presents a comparison of thrust values from simulations taken from [83].

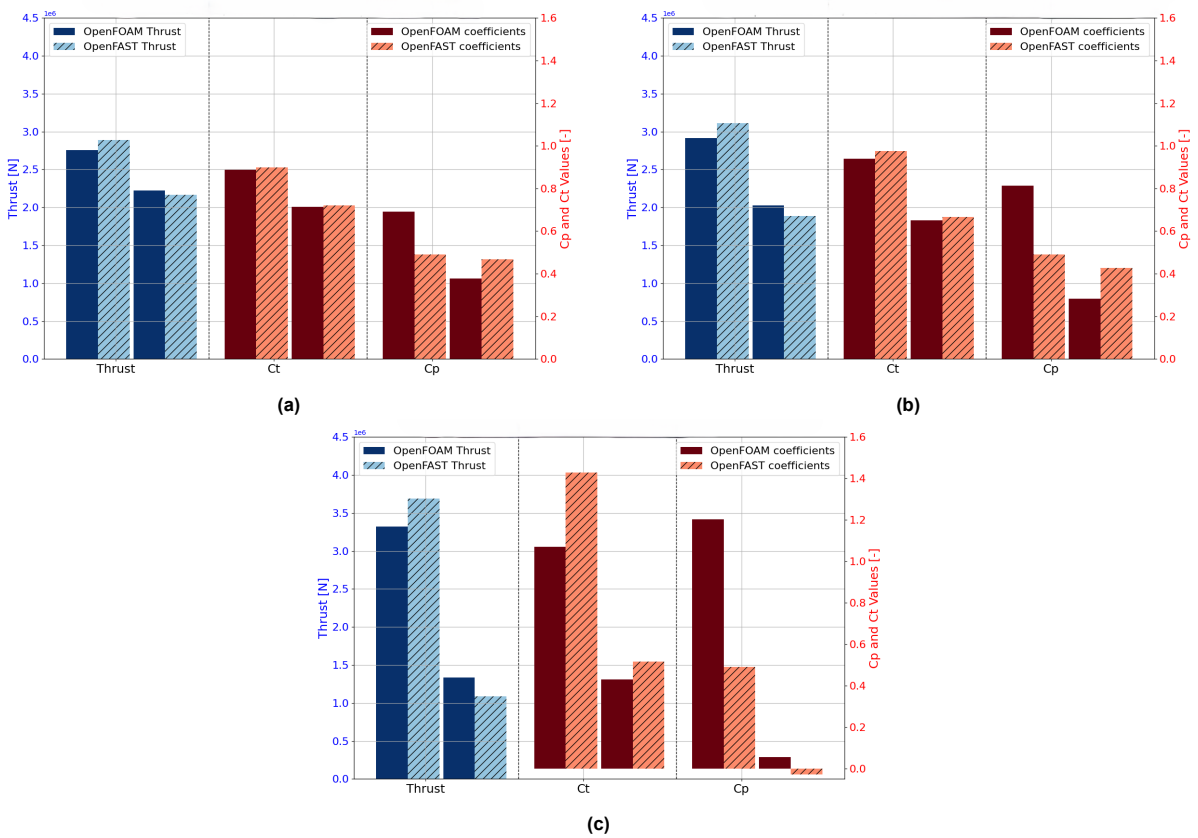

(a) (b)

(c)

Figure 4.8: Comparison of Max/Min Values and Coefficients for Prescribed Motion with frequencies of 0.01419, 0.02441, 0.05676 Hz as shown in a,b, and c, respectively

From Figure 4.8, the following observations can be made:

- **Thrust**: The thrust over a cycle is plotted to facilitate this analysis, comparing OpenFOAM and OpenFAST simulations in Figure 4.7a. All simulations exhibit a similar average thrust value around 2.5 MN. Additionally, OpenFAST consistently overestimates the thrust deviation from the mean compared to OpenFOAM, a trend also observable in Figure 4.8. This aligns with the steady-state simulations, where OpenFAST also recorded higher thrust values than OpenFOAM. The artifact seen in Figure 4.7a in the highest frequency simulation is probably due to an error in the OpenFAST approximations, as such phenomena have not been seen in literature before, even when the thrust becomes negative.
- C_T: The trends for the thrust coefficients mirror those observed for thrust. Notably, for slower movements, such as at a frequency of 0.01419 Hz, the differences in thrust coefficients are less pronounced compared to faster simulations.
- C_P: As previously noted in the steady simulations, the power coefficients exhibit significant discrepancies between the two simulation types. The lack of consideration for near-wake effects in OpenFAST is even more pronounced with the turbine in motion. Interestingly, the amplitude of the power coefficient in OpenFOAM is higher than in OpenFAST. The reason is probably the omission of turbine wake effects in the latter.

In their study, Ramos-García, Sessarego, and Horcas [82] also conducted tests and compared the BEM and LL solvers using MIRAS-BEM and MIRAS-HAWC2, respectively. The comparison with the present simulations revealed some differences in trends, with less mismatch between their mid and higher-fidelity approaches. The mean value of their simulation is different, which is attributed to their inclusion of the shaft tilt and precone angle. Additionally, the path's shape in their simulations was more pear-shaped, whereas the present simulations showed a more elliptical shape. Both models are similar in that they are modeled as rigid bodies with no control and the same prescribed motions. It is possible that the simulations from Ramos-García, Sessarego, and Horcas [82], which have a wind speed above the rated (10.8 m/s), exhibit more unsteady phenomena. A further reason could be that the present simulations do not include any dynamic stall modeling, which could explain the asymmetric shape of the surge-thrust curve. It is unknown if these were modeled by Ramos-García, Sessarego, and Horcas [82].

Looking at the angle of attack at different positions of the blade, several observations can be made based on Figure 4.9 Figure 4.10 and Figure 4.11:

- As the frequency increases, the range of extrema in the angle of attack also widens. This occurs because the floater's velocity rises, leading to more significant variations in the axial inflow.
- OpenFAST consistently underestimates the angle of attack across all frequencies, although the discrepancy diminishes with increasing frequency. This observation aligns with the results from the steady turbine analysis. It is unclear why there is a diminution with the increase in frequency.
- The most considerable amplitude variations are observed closer to the inboard section of the blade. This phenomenon is attributed to the higher ratio of tangential to axial speeds in this region, resulting in more significant changes in the angle of attack.
- Furthermore, OpenFAST appears to overestimate the amplitude range compared to OpenFOAM. This discrepancy likely stems from OpenFAST's lack of modeling for the induction zone, as the rotor interacts with its wake during operation.

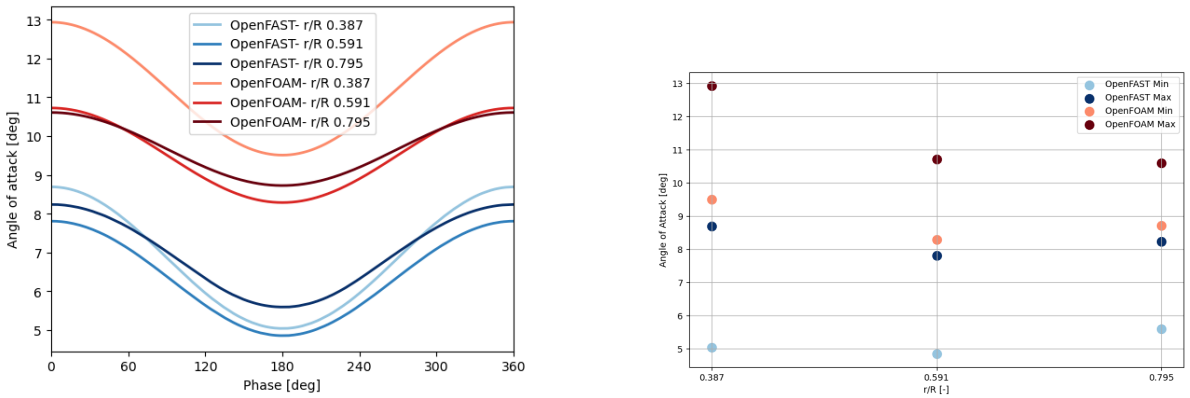

(a) (b)

Figure 4.9: Comparison of the angle of attacks for a prescribed motion at a frequency of $0.0149Hz$. On the left, the amplitudes are compared to the phase of motion, and on the right, the min/max values of the angle of attack are shown.

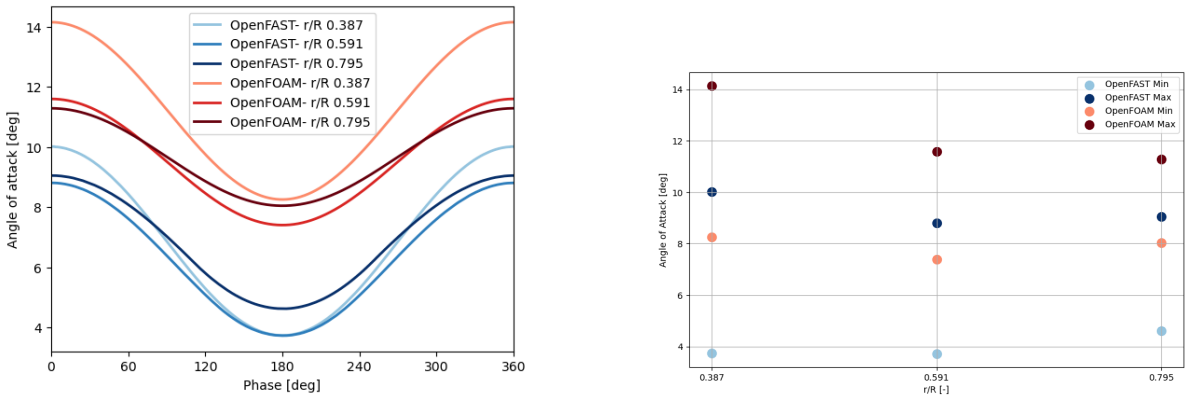

(a) (b)

Figure 4.10: Comparison of the angle of attack for prescribed motion at a frequency of $0.02441Hz$. On the left, the amplitudes are compared to the phase of motion, and on the right, the min/max values of the angle of attack are shown.

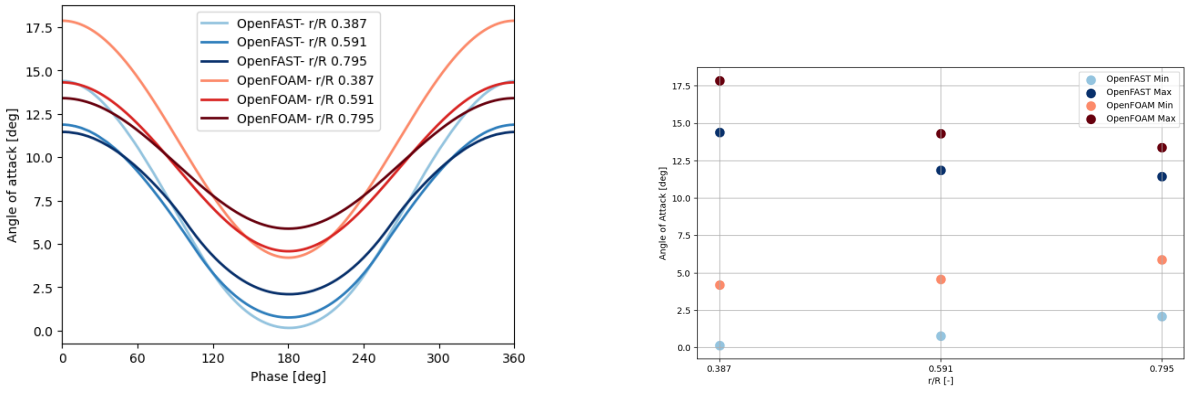

Figure 4.11: Comparison of the angle of attack for prescribed motion at a frequency of $0.05676Hz$. On the left, the amplitudes are compared to the phase of motion, and on the right, the min/max values of the angle of attack are shown.

4.5. Conclusions and recommendations

In this chapter, we have verified the setup of a full-scale 15MW wind turbine in OpenFOAM. To do so, we have built two setups, OpenFOAM and OpenFAST, and compared the turbines in different conditions.

From the steady turbines, we have concluded that OpenFAST slightly overestimates the thrust despite having close thrust coefficients. This has been attributed to the difference in the relative velocities in the two approaches since CFD simulations calculate the flow around the turbine contrary to the BEM solution. However, The power coefficient is significantly different because the blade-near wake is not modeled in OpenFAST. Similar conclusions were already found in the MSc. thesis of C. Dos Santos Pereira Malveiro [9] and Trigaux, Chatelain, and Winckelmans [108].

Regarding prescribed motion, surge motions significantly impact power and thrust. This is coherent with the literature on this topic. Generally speaking, one can say that for a constant amplitude, the higher the frequency, the higher the thrust amplitude within a period. OpenFAST overpredicts the amplitude despite having a very similar average value. The power coefficient is often overestimated by the higher frequency simulation in OpenFOAM, highlighting the impact of rotor wake interactions in the power calculations.

Several key areas are identified for further study to improve the accuracy and fidelity of wind turbine simulations. These include:

- Perform a temporal and spatial convergence study with varying smearing parameters to minimize numerical errors and improve solution stability.
- Investigate the influence of the smearing factor on the performance of the IEA 15MW wind turbine to understand its impact on large turbines better.
- Analyze the effects of blade elasticity under prescribed motions, focusing on aeroelasticity and its influence on rotor behavior. This is important as bigger blades have an increased bending, which leads to increased aeroelastic effects.
- Incorporate nacelle and tower modeling to investigate their influence on rotor loading and compare results across varying fidelity levels of simulation.
- Include wind shear, wind veer, and turbulence effects in the simulations to capture more realistic operating conditions and better predict performance.
- Assess the impact of dynamic stall modeling for different prescribed motion profiles and its consequences for rotor performance. Compare between OpenFAST and OpenFOAM
- Run partially coupled simulations in OpenFAST, prescribing the motion to `turbinesFoam`, and compare the results between OpenFAST and OpenFOAM to evaluate consistency and accuracy.
- Compare the partially coupled simulations with fully coupled simulations, recognizing the complexity involved due to numerous variable parameters, even when using simplified models.

Addressing these areas can refine the simulations further and provide more accurate and comprehensive insights into the performance of floating wind turbines.

5

Conclusion

This chapter concludes the thesis by summarizing and discussing the primary research findings. It begins with a brief overview of the project, followed by an evaluation of the research questions outlined in chapter 1 and a summary of the main results. The chapter concludes with recommendations for future research and some final advice.

5.1. Thesis summary

In this thesis, the framework of Pere Frontera Pericàs [81] that has been continued by Scarlatti [98] has been continued and used to model the IEA 15MW wind turbine coupled with the VolturnUS-S semi-submersible platform. This turbine is larger than the previously modeled 5 MW wind turbine and is not aligned with the current or future market. This thesis aimed to develop an open-source, high-fidelity CFD model for simulating Floating Offshore Wind Turbines (FOWTs). The project's primary focus was to verify and compare the results with mid-fidelity software such as OpenFAST, thus highlighting their differences. Ultimately, we aim to establish a reliable CFD model for future research. The FOWT simulation model was built using OpenFOAM, an open-source C++ toolbox designed for creating customized numerical solvers, particularly for computational fluid dynamics (CFD) problems. Wave generation and absorption were handled using the waves2Foam library, developed by Jacobsen [52]. Additionally, mooring line modeling, which provides extra stiffness to the FOWT, utilized `Moody`, developed by Palm et al. [77]. Finally, the aerodynamic modeling and analysis were done using the `turbinesFoam` package, using actuator line modeling.

Based on the settings from Scarlatti [98], first, the floater was modeled in chapter 3. A spatial convergence study was performed to determine the computationally effective and accurate mesh. Through this process, several vital parameters have been tested to meet the desired accuracy and stability of the simulations, such as the initial equilibrium position, the acceleration-relaxation factor, and the choice of the numerical timestep. The mesh has been verified for motions up to 24m, which the floater reaches in very harsh conditions in case of a focused wave. A slight sensitivity analysis was run to assess the optimal number of cores needed to do a simulation and accelerate the modeling.

Comparisons between OpenFOAM and OpenFAST for surge, heave, and pitch simulations revealed OpenFAST's underestimation of linear and quadratic damping coefficients due to its simplified modeling of viscous effects and empirical drag coefficients. On the other hand, OpenFOAM simulations demonstrated the mooring theory's influence on P-Q analysis, especially for smaller decay tests. It was also found that the equilibrium position of the floater seems to be different depending on the initial mesh, using morphing meshes. Validation strategies were also discussed, suggesting the potential use of experimental data from the Plymouth experiment or the OC7 campaign. Overall, the setup developed using OpenFOAM's `waves2Foam` and `Moody` tools provides a reliable framework for simulating large motions and improving the convergence of decay tests, highlighting CFD's value in enhancing mid-fidelity models like OpenFAST.

In chapter 4, we verified the setup of a full-scale 15MW wind turbine in OpenFOAM by building and

comparing two setups: one in OpenFOAM and another in OpenFAST. For steady-state conditions, we found that OpenFAST slightly overestimates thrust despite similar thrust coefficients, likely due to differences in how relative velocities are calculated—CFD models the flow around the turbine, unlike the BEM approach in OpenFAST. However, the power coefficient shows significant differences, which can be attributed to OpenFAST not modeling the blade-near wake. These findings are consistent with previous studies by C. Dos Santos Pereira Malveiro [9] and Trigaux, Chatelain, and Winckelmans [108].

When considering prescribed motion using the modified `floatingTurbinesFoam` by Pere Frontera Pericàs [81], surge movements were found to have a noticeable effect on both thrust and power, aligning with existing literature. Generally, for a constant amplitude, higher frequencies result in greater thrust amplitude over a cycle. OpenFAST overestimates these fluctuations, though the average thrust remains similar. In high-frequency simulations, the power coefficient is significantly overestimated in OpenFOAM, underlining the importance of rotor wake interactions in power predictions.

Finally, an updated tutorial will be provided to streamline and expedite the installation process of the entire setup, which proved time-consuming during this thesis.

5.2. Answer to the research questions

How do decay tests of the VolturnUS-S floater in OpenFOAM using `waves2foam` and a FEM model compare with mid-fidelity models like OpenFAST for large motions? What differences in damping can be observed?

In this work, a VolturnUS-S floater case is built and verified in OpenFOAM using the `waves2Foam` library and a FEM model and then compared against mid-fidelity model OpenFAST for large motions. The results indicate several critical differences in damping and performance between these models.

First, a spatial convergence study was conducted, which determined the optimal parameters for balancing computational efficiency and accuracy. It was found that OpenFOAM, using a refined mesh and constant time-stepping, provided reliable results for both 15m and 24m decay tests. These tests highlighted the importance of maintaining consistent Courant numbers and longer simulation times to capture more accurate data points for the P-Q analysis, which is essential for evaluating large motions.

The first finding was that OpenFOAM simulations did not behave like OpenFAST simulations and did not have the same equilibrium position. This divergence was attributed to the variances in mesh configurations in OpenFOAM. The P-Q analysis helped identify that the equilibrium positions in the simulations differed by up to 5 cm, which made highly sensitive post-processing like the P-Q analysis diverge.

A key finding was that OpenFAST consistently underestimated linear and quadratic damping coefficients compared to OpenFOAM, a trend consistent with the OC6 study on the DeepCWind floater. This discrepancy is mainly due to the viscous effects in OpenFAST, which are modeled through empirical drag coefficients and simplified theories within HydroDyn, leading to an incomplete representation of nonlinear damping. The heave and pitch tests showed similar trends, reinforcing the conclusion that OpenFOAM's higher fidelity provides a more accurate representation of the hydrodynamic behavior.

Mooring modeling differences between the two approaches were also significant, particularly for smaller decay tests (e.g., 5m decay), where `Moody's` mooring theory played a noticeable role in the P-Q analysis. To ensure consistency, this could be addressed using the same mooring line model, `MoorDyn`, in both OpenFOAM and OpenFAST.

Finally, a sensitivity study was conducted on the number of processors necessary to have a computationally effective hardware setup and run computationally expensive simulations.

How do simulations of the IEA 15MW wind turbine using `turbinesFoam` compare to OpenFAST simulations models for both steady and prescribed harmonic motions?

In this work, a 15MW wind turbine case was built using `turbinesFoam` in OpenFOAM, and it was compared to the mid-fidelity model OpenFAST for both steady and prescribed harmonic motion conditions. The comparison reveals critical differences in how these models handle turbine aerodynamics, thrust, and power predictions.

In steady-state simulations, the thrust predicted by OpenFAST slightly overestimates that of OpenFOAM, even though both approaches yield close thrust coefficients. The primary reason for this difference is how each model calculates relative velocities: OpenFOAM, being a CFD tool, computes the detailed flow around the turbine, while OpenFAST uses a Blade Element Momentum (BEM) model, which does not resolve the flow around the blades in the same way. This leads to differences in thrust predictions, as observed in previous studies.

A more notable difference is observed in the power coefficient (C_p), where OpenFOAM consistently predicts higher values than OpenFAST. This discrepancy can be explained by OpenFAST's inability to model the near-wake effects of the turbine, which are critical for accurate power predictions. In contrast, using an Actuator Line Model (ALM), OpenFOAM better captures these wake interactions, resulting in a more precise power coefficient. Similar findings were observed in prior research by C. Dos Santos Pereira Malveiro [9] and Trigaux, Chatelain, and Winckelmans [108].

For prescribed motion scenarios, surge movements significantly impact thrust and power, aligning with existing literature. As the surge frequency increases, the amplitude of the thrust variation also increases. However, OpenFAST tends to overpredict the thrust amplitude compared to OpenFOAM, although the average thrust values remain similar between the two models.

The power coefficient in OpenFOAM is significantly higher for high-frequency simulations, underscoring the importance of rotor wake interactions in power calculations, which OpenFAST does not fully capture. These wake effects become even more pronounced when the turbine is in motion, further highlighting the limitations of mid-fidelity models like OpenFAST in predicting dynamic behaviors.

In conclusion, while OpenFAST provides a simplified and computationally efficient approach, OpenFOAM, with `turbinesFoam`, offers a more detailed and accurate representation of both steady-state and dynamic wind turbine behaviors, especially when wake effects and rotor-turbine interactions are crucial to the analysis.

5.3. Recommendations for Future Work

Based on the findings and insights from the current study, several recommendations for future work are proposed to enhance the understanding and modeling of floating offshore wind turbines (FOWTs):

- **Model Validation:** Validate the coupled model against experimental data, mainly focusing on the VolturnUS-S floater using the OC7 campaign data.
- **Complex Phenomena Testing:** With the individual tested models, one can build a coupled model using the work from Pere Frontera Pericàs [81] under more complex environmental conditions while maintaining a consistent mooring model to minimize uncertainties in error attribution.
- **Overset Mesh Motion Technique:** Implement the overset mesh motion technique to improve simulation stability and accuracy during more significant amplitude motions. This technique utilizes two overlapping meshes—one for the background and one for the moving body boundary—to capture complex fluid-structure interaction (FSI) phenomena effectively. During this thesis, countless simulations failed, and the morphing mesh technique has been pushed to its limit. It may even be less computationally time-effective than a traditional overset mesh technique.
- **Mooring Modeling Exploration:** Investigate the `Moody` mooring model for large full-scale systems and perform a convergence study to ensure reliability in the system's performance predictions. Use similar mooring techniques that do not vary too much to compare mid-fidelity and high-fidelity fully coupled simulations without having too many uncertainties in attributing the phenomena.
- **Modifications to floatingturbinesFoam:** Modify the `floatingturbinesFoam` library to enable the performance of any prescribed motions without modeling the floater, enhancing its applicability for various operational scenarios. Additionally, assess the impact of aeroelasticity on large wind turbines within the `floatingturbinesFoam` framework, focusing on how blade flexibility influences rotor behavior under prescribed motions.
- **Comprehensive Performance Assessment:** Investigate the influence of the smearing factor on the performance of the IEA 15 MW wind turbine while incorporating nacelle and tower modeling

to evaluate their effects on rotor loading. Additionally, the simulations should include realistic operating conditions such as wind shear, wind veer, and turbulence effects to enhance performance predictions. Finally, the impact of dynamic stall modeling under various prescribed motion profiles will be assessed, and results from OpenFAST and OpenFOAM will be compared to gain a deeper understanding of rotor performance.

- **Coupled Simulation Comparisons:** Conduct partially coupled simulations in OpenFAST by prescribing motions to TurbinesFoam and compare the results with OpenFOAM to evaluate consistency and accuracy. Additionally, compare these partially coupled simulations with fully coupled simulations, acknowledging the complexity introduced by numerous variable parameters, even when using simplified models. Test how coupled the simulation has to be by varying the number of outer correctors within the SIMPLE loop.

References

[1] Christopher Allen et al. *Definition of the UMaine VolturnUS-S Reference Platform Developed for the IEA Wind 15-Megawatt Offshore Reference Wind Turbine*. NREL/TP-5000-76773. National Renewable Energy Lab. (NREL), Golden, CO (United States); Univ. of Maine, Orono, ME (United States), July 1, 2020. DOI: 10.2172/1660012. URL: https://www.osti.gov/biblio/1660012 (visited on 02/29/2024).

[2] Alireza Arabgolarcheh, Sahar Jannesarahmadi, and Ernesto Benini. "Modeling of near wake characteristics in floating offshore wind turbines using an actuator line method". In: *Renewable Energy* 185 (Feb. 1, 2022), pp. 871–887. ISSN: 0960-1481. DOI: 10.1016/j.renene.2021.12.099. URL: https://www.sciencedirect.com/science/article/pii/S0960148121018267 (visited on 08/30/2024).

[3] José Azcona. "INNWIND.EU D4.21: State-of-the-art and implementation of design tools for floating structures". In: *Task 4.2: Verification and validation of design methods for floating structures* WP4: Offshore Foundations and Support Structures (Dec. 30, 2013).

[4] Pete Bachant et al. *turbinesFoam/turbinesFoam: v0.1.1*. Version v0.1.1. Nov. 15, 2019. DOI: 10.5281/zenodo.3542301. URL: https://zenodo.org/records/3542301 (visited on 08/31/2024).

[5] I. Bayati et al. "On the aero-elastic design of the DTU 10MW wind turbine blade for the LIFES50+ wind tunnel scale model". In: *Journal of Physics: Conference Series* 753.2 (Sept. 2016). Publisher: IOP Publishing, p. 022028. ISSN: 1742-6596. DOI: 10.1088/1742-6596/753/2/022028. URL: https://dx.doi.org/10.1088/1742-6596/753/2/022028 (visited on 07/23/2024).

[6] L. Bennun et al. *Mitigating biodiversity impacts associated with solar and wind energy development*. IUCN, 2021. ISBN: 978-2-8317-2104-0. DOI: 10.2305/IUCN.CH.2021.06.en. URL: https://portals.iucn.org/library/node/49617 (visited on 08/30/2024).

[7] Roger Bergua et al. "OC6 project Phase III: validation of the aerodynamic loading on a wind turbine rotor undergoing large motion caused by a floating support structure". In: *Wind Energy Science* 8.4 (Apr. 6, 2023). Publisher: Copernicus GmbH, pp. 465–485. ISSN: 2366-7443. DOI: 10.5194/wes-8-465-2023. URL: https://wes.copernicus.org/articles/8/465/2023/ (visited on 02/01/2024).

[8] Simon Burmester, Guilherme Vaz, and Ould el Moctar. "Towards credible CFD simulations for floating offshore wind turbines". In: *Ocean Engineering* 209 (Aug. 1, 2020), p. 107237. ISSN: 0029-8018. DOI: 10.1016/j.oceaneng.2020.107237. URL: https://www.sciencedirect.com/science/article/pii/S0029801820302870 (visited on 02/23/2024).

[9] C. Dos Santos Pereira Malveiro. *Aerodynamics of a 15-MW and a 5-MW Reference Wind Turbine Using Varying Fidelity Tools*. URL: https://repository.tudelft.nl/file/File_f08dc534-1da8-4b49-8c88-3a0ee7af6a13?preview=1 (visited on 08/27/2024).

[10] Guillén Campaña-Alonso, Esteban Ferrer, and Beatriz Méndez-López. "Wind turbine power extraction under partial wake operations, a CFD study using ALM." In: *Journal of Physics: Conference Series* 2767.9 (June 2024). Publisher: IOP Publishing, p. 092097. ISSN: 1742-6596. DOI: 10.1088/1742-6596/2767/9/092097. URL: https://dx.doi.org/10.1088/1742-6596/2767/9/092097 (visited on 08/31/2024).

[11] Lin Chen, Biswajit Basu, and Søren R. K. Nielsen. "A coupled finite difference mooring dynamics model for floating offshore wind turbine analysis". In: *Ocean Engineering* 162 (Aug. 15, 2018), pp. 304–315. ISSN: 0029-8018. DOI: 10.1016/j.oceaneng.2018.05.001. URL: https://www.sciencedirect.com/science/article/pii/S0029801818307005 (visited on 05/22/2024).

[12] Peng Chen, Jiahao Chen, and Zhiqiang Hu. “Review of Experimental-Numerical Methodologies and Challenges for Floating Offshore Wind Turbines”. In: *Journal of Marine Science and Application* 19.3 (Sept. 1, 2020), pp. 339–361. ISSN: 1993-5048. DOI: 10.1007/s11804-020-00165-z. URL: https://doi.org/10.1007/s11804-020-00165-z (visited on 02/07/2024).

[13] Shuangyin Chen et al. “Life Cycle Assessment and Economic Analysis of Biomass Energy Technology in China: A Brief Review”. In: *Processes* 8.9 (Sept. 2020). Number: 9 Publisher: Multidisciplinary Digital Publishing Institute, p. 1112. ISSN: 2227-9717. DOI: 10.3390/pr8091112. URL: https://www.mdpi.com/2227-9717/8/9/1112 (visited on 05/29/2023).

[14] Ping Cheng, Yang Huang, and Decheng Wan. “A numerical model for fully coupled aero-hydrodynamic analysis of floating offshore wind turbine”. In: *Ocean Engineering* 173 (Feb. 1, 2019), pp. 183–196. ISSN: 0029-8018. DOI: 10.1016/j.oceaneng.2018.12.021. URL: https://www.sciencedirect.com/science/article/pii/S0029801818314124 (visited on 02/07/2024).

[15] Ping Cheng and Decheng Wan. “Fully-Coupled Aero-Hydrodynamic Simulation of Floating Offshore Wind Turbines by Different Simulation Methods”. In: *Volume 11A: Honoring Symposium for Professor Carlos Guedes Soares on Marine Technology and Ocean Engineering*. ASME 2018 37th International Conference on Ocean, Offshore and Arctic Engineering. Madrid, Spain: American Society of Mechanical Engineers, June 17, 2018, V11AT12A045. ISBN: 978-0-7918-5132-6. DOI: 10.1115/OMAE2018-78368. URL: https://asmedigitalcollection.asme.org/OMAE/proceedings/OMAE2018/51326/Madrid,%20Spain/274195 (visited on 02/22/2024).

[16] Ping Cheng, Decheng Wan, and Changhong Hu. “Numerical Simulations of Flows around Floating Offshore Wind Turbine”. In: *Proceedings of the Twenty-eighth (2018) International Ocean and Polar Engineering Conference* International Society of Offshore and Polar Engineers (ISOPE) (June 10, 2018).

[17] Stefano Cioni et al. “On the characteristics of the wake of a wind turbine undergoing large motions caused by a floating structure: an insight based on experiments and multi-fidelity simulations from the OC6 project Phase III”. In: *Wind Energy Science* 8.11 (Nov. 10, 2023). Publisher: Copernicus GmbH, pp. 1659–1691. ISSN: 2366-7443. DOI: 10.5194/wes-8-1659-2023. URL: https://wes.copernicus.org/articles/8/1659/2023/ (visited on 08/21/2024).

[18] Günther Clauss, Eike Lehmann, and Carsten Östergaard. *Offshore Structures*. London: Springer, 1992. ISBN: 978-1-4471-3195-3 978-1-4471-3193-9. DOI: 10.1007/978-1-4471-3193-9. URL: http://link.springer.com/10.1007/978-1-4471-3193-9 (visited on 05/21/2024).

[19] “Climate Change 2022, Mitigation of Climate Change. Summary for Policymakers”. In: ().

[20] Robin Combette. *Large-Eddy Simulation of a Floating Offshore Wind Turbine with imposed motion*. TU Delft, Sept. 2023.

[21] Lorenzo Cottura et al. “Dynamic Modeling of an Offshore Floating Wind Turbine for Application in the Mediterranean Sea”. In: *Energies* 14 (Jan. 5, 2021), p. 248. DOI: 10.3390/en14010248.

[22] Fuyin Cui et al. “Hydrodynamic Response Analysis of the Combined IEA-15-240-RWT and UMaine VolturnUS-S System to Extreme Loading”. In: The 33rd International Ocean and Polar Engineering Conference. OnePetro, June 19, 2023. URL: https://dx.doi.org/ (visited on 02/26/2024).

[23] Griet Decorte, Geert Lombaert, and Jaak Monbaliu. “A first assessment of the interdependency of mesh motion and free surface models in OpenFOAM regarding wave-structure interaction”. In: ().

[24] DNV. *Design of Offshore Wind Turbine Structures*. OFFSHORE STANDARD DNV-OS-J101. 2014.

[25] Jing Dong and Axelle Viré. “Comparative analysis of different criteria for the prediction of vortex ring state of floating offshore wind turbines”. In: *Renewable Energy* 163 (Jan. 1, 2021), pp. 882–909. ISSN: 0960-1481. DOI: 10.1016/j.renene.2020.08.027. URL: https://www.sciencedirect.com/science/article/pii/S0960148120312647 (visited on 01/31/2024).

[26] B. Dose et al. “Fluid-structure coupled computations of the NREL 5 MW wind turbine by means of CFD”. In: *Renewable Energy* 129 (Dec. 1, 2018), pp. 591–605. ISSN: 0960-1481. DOI: 10.1016/j.renene.2018.05.064. URL: https://www.sciencedirect.com/science/article/pii/S0960148118305858 (visited on 02/07/2024).

[27] L. Eça and M. Hoekstra. “A procedure for the estimation of the numerical uncertainty of CFD calculations based on grid refinement studies”. In: *Journal of Computational Physics* 262 (Apr. 1, 2014), pp. 104–130. ISSN: 0021-9991. DOI: 10.1016/j.jcp.2014.01.006. URL: https://www.sciencedirect.com/science/article/pii/S0021999114000278 (visited on 03/01/2024).

[28] *Éolien en mer : 5 propositions pour atteindre 50 GW en 2050 - France Renouvelables*. URL: https://www.france-renouvelables.fr/etudes-et-publications/eolien-en-mer-5-propositions-pour-atteindre-50-gw-en-2050/ (visited on 08/30/2024).

[29] Claes Eskilsson and Johannes Palm. “High-fidelity modelling of moored marine structures: multi-component simulations and fluid-mooring coupling”. In: *Journal of Ocean Engineering and Marine Energy* 8.4 (Nov. 1, 2022), pp. 513–526. ISSN: 2198-6452. DOI: 10.1007/s40722-022-00263-w. URL: https://doi.org/10.1007/s40722-022-00263-w (visited on 05/22/2024).

[30] Claes Eskilsson et al. “Hydrodynamic Simulations of a FOWT Platform (1st FOWT Comparative Study) Using OpenFOAM Coupled to MoodyCore”. In: *Proceedings of the Thirty-third (2023) International Ocean and Polar Engineering Conference*. International Society of Offshore and Polar Engineers (ISOPE). Ottawa, Canada, June 19, 2023.

[31] Yuan Fang et al. “Effect of surge motion on rotor aerodynamics and wake characteristics of a floating horizontal-axis wind turbine”. In: *Energy* 218 (Mar. 1, 2021), p. 119519. ISSN: 0360-5442. DOI: 10.1016/j.energy.2020.119519. URL: https://www.sciencedirect.com/science/article/pii/S0360544220326268 (visited on 09/22/2024).

[32] Alessandro Fontanella et al. “UNAFLOW: a holistic wind tunnel experiment about the aerodynamic response of floating wind turbines under imposed surge motion”. In: *Wind Energy Science* 6.5 (Sept. 9, 2021). Publisher: Copernicus GmbH, pp. 1169–1190. ISSN: 2366-7443. DOI: 10.5194/wes-6-1169-2021. URL: https://wes.copernicus.org/articles/6/1169/2021/ (visited on 02/01/2024).

[33] Matthew Fowler et al. “Wind/Wave Testing of a 1:70-Scale Performance-Matched Model of the IEA Wind 15 MW Reference Wind Turbine with Real-Time ROSCO Control and Floating Feedback”. In: *Machines* 11.9 (Aug. 28, 2023), p. 865. ISSN: 2075-1702. DOI: 10.3390/machines11090865. URL: https://www.mdpi.com/2075-1702/11/9/865 (visited on 04/11/2024).

[34] Evan Gaertner et al. *IEA Wind TCP Task 37: Definition of the IEA 15-Megawatt Offshore Reference Wind Turbine*. NREL/TP-5000-75698. National Renewable Energy Lab. (NREL), Golden, CO (United States), Mar. 2, 2020. DOI: 10.2172/1603478. URL: https://www.osti.gov/biblio/1603478 (visited on 02/29/2024).

[35] Kishan Gajjar. *Effect of structural elasticity on simulation of wind turbines and its verification*. Tu Delft, Sept. 2023.

[36] Global Wind Energy Council (GWEC). *Global Wind Report 2024*. URL: https://gwec.net/wp-content/uploads/2024/05/GWR-2024_digital-version_final-2.pdf (visited on 05/27/2024).

[37] Jiaye Gong et al. “Numerical simulation of the interaction between FOWT and focused wave by a hybrid method”. In: *Thirty-third (2023) International Ocean and Polar Engineering Conference*. International Society of Offshore and Polar Engineers (ISOPE). Vol. International Society of Offshore and Polar Engineers (ISOPE). Ottawa, Canada, June 19, 2023.

[38] Raul Guanche et al. *Integrated FOWT test report*. D5.3. Publisher: Zenodo. Apr. 12, 2023. URL: https://zenodo.org/records/7871090 (visited on 09/14/2024).

[39] Rizwan Haider et al. “Review of Computational Fluid Dynamics in the Design of Floating Offshore Wind Turbines”. In: *Energies* 17.17 (Jan. 2024). Number: 17 Publisher: Multidisciplinary Digital Publishing Institute, p. 4269. ISSN: 1996-1073. DOI: 10.3390/en17174269. URL: https://www.mdpi.com/1996-1073/17/17/4269 (visited on 09/02/2024).

[40] Matthew Hall, Brad Buckham, and Curran Crawford. “Evaluating the importance of mooring line model fidelity in floating offshore wind turbine simulations”. In: *Wind Energy* 17.12 (2014). _eprint: https://onlinelibrary.wiley.com/doi/pdf/10.1002/we.1669, pp. 1835–1853. ISSN: 1099-1824. DOI: 10.1002/we.1669. URL: https://onlinelibrary.wiley.com/doi/abs/10.1002/we.1669 (visited on 05/22/2024).

[41] Matthew Hall and Andrew Goupee. “Validation of a lumped-mass mooring line model with DeepCwind semisubmersible model test data”. In: *Ocean Engineering* 104 (Aug. 1, 2015), pp. 590–603. ISSN: 0029-8018. DOI: 10.1016/j.oceaneng.2015.05.035. URL: https://www.sciencedirect.com/science/article/pii/S0029801815002279 (visited on 05/22/2024).

[42] Matthew Hall and Andrew J. Goupee. “Validation of a hybrid modeling approach to floating wind turbine basin testing”. In: *Wind Energy* 21.6 (2018), pp. 391–408. ISSN: 1099-1824. DOI: 10.1002/we.2168. URL: https://onlinelibrary.wiley.com/doi/abs/10.1002/we.2168 (visited on 07/23/2024).

[43] Mohamed Hassan and C. Guedes Soares. “Dynamic Analysis of a Novel Installation Method of Floating Spar Wind Turbines”. In: *Journal of Marine Science and Engineering* 11.7 (July 2023). Number: 7 Publisher: Multidisciplinary Digital Publishing Institute, p. 1373. ISSN: 2077-1312. DOI: 10.3390/jmse11071373. URL: https://www.mdpi.com/2077-1312/11/7/1373 (visited on 10/02/2024).

[44] John Marius Hegseth and Erin E. Bachynski. “A semi-analytical frequency domain model for efficient design evaluation of spar floating wind turbines”. In: *Marine Structures* 64 (Mar. 1, 2019), pp. 186–210. ISSN: 0951-8339. DOI: 10.1016/j.marstruc.2018.10.015. URL: https://www.sciencedirect.com/science/article/pii/S0951833918303149 (visited on 06/03/2024).

[45] Remment ter Hofstede et al. “Settlement success of European flat oyster (*Ostrea edulis*) on different types of hard substrate to support reef development in offshore wind farms”. In: *Ecological Engineering* 200 (Mar. 1, 2024), p. 107189. ISSN: 0925-8574. DOI: 10.1016/j.ecoleng.2024.107189. URL: https://www.sciencedirect.com/science/article/pii/S0925857424000132 (visited on 08/30/2024).

[46] Anna Holcombe et al. “A comparative study of potential-flow-based numerical models to experimental tests of a semi- submersible floating wind turbine platform”. In: *Proceedings of the Thirty-third (2023) International Ocean and Polar Engineering Conference*. International Society of Offshore and Polar Engineers (ISOPE). Ottawa, Canada, June 19, 2023.

[47] Yang Huang, Ping Cheng, and Decheng Wan. “Numerical Analysis of a Floating Offshore Wind Turbine by Coupled Aero-Hydrodynamic Simulation”. In: *Journal of Marine Science and Application* 18.1 (Mar. 1, 2019), pp. 82–92. ISSN: 1993-5048. DOI: 10.1007/s11804-019-00084-8. URL: https://doi.org/10.1007/s11804-019-00084-8 (visited on 02/22/2024).

[48] IEA. “World Energy Outlook 2023”. In: (). URL: https://www.iea.org/reports/world-energy-outlook-2023.

[49] Intergovernmental Panel On Climate Change (Ipcc). “Climate Change 2022 – Impacts, Adaptation and Vulnerability: Working Group II Contribution to the Sixth Assessment Report of the Intergovernmental Panel on Climate Change”. In: (June 22, 2023). DOI: 10.1017/9781009325844. URL: https://www.cambridge.org/core/product/identifier/9781009325844/type/book (visited on 05/08/2024).

[50] *IRA Year Two: A Clean Future in Clear Focus*. Energy.gov. URL: https://www.energy.gov/lpo/articles/ira-year-two-clean-future-clear-focus (visited on 08/30/2024).

[51] Raad I. Issa J. Oliveira Paulo. “An Improved Piso Algorithm for the Computation of Buoyancy-Driven Flows”. In: *Numerical Heat Transfer, Part B: Fundamentals* 40.6 (Dec. 1, 2001). Publisher: Taylor & Francis _eprint: https://doi.org/10.1080/104077901753306601, pp. 473–493. ISSN: 1040-7790. DOI: 10.1080/104077901753306601. URL: https://doi.org/10.1080/104077901753306601 (visited on 05/23/2024).

[52] Niels Jacobsen. *waves2Foam Manual*. Aug. 17, 2017.

[53] Sudhir Jagdale et al. “A Comparative Numerical Study of Hydrodynamic Response of a Floating Offshore Wind Turbine Semi-submersible Platform by Using QaleFOAM”. In: ().

[54] Changqing Jiang et al. “Validation of a dynamic mooring model coupled with a RANS solver”. In: *Marine Structures* 72 (July 1, 2020), p. 102783. ISSN: 0951-8339. DOI: 10.1016/j.marstruc.2020.102783. URL: https://www.sciencedirect.com/science/article/pii/S0951833920300770 (visited on 05/22/2024).

[55] Jason M. Jonkman et al. “Full-System Linearization for Floating Offshore Wind Turbines in OpenFAST”. In: ASME 2018 1st International Offshore Wind Technical Conference. American Society of Mechanical Engineers Digital Collection, Dec. 13, 2018. DOI: 10.1115/IOWTC2018-1025. URL: https://dx.doi.org/10.1115/IOWTC2018-1025 (visited on 06/03/2024).

[56] Richard Kimball et al. “Wind/Wave Basin Verification of a Performance-Matched Scale-Model Wind Turbine on a Floating Offshore Wind Turbine Platform”. In: ASME 2014 33rd International Conference on Ocean, Offshore and Arctic Engineering. American Society of Mechanical Engineers Digital Collection, Oct. 1, 2014. DOI: 10.1115/OMAE2014-24166. URL: https://dx.doi.org/10.1115/OMAE2014-24166 (visited on 06/03/2024).

[57] Bonjun J. Koo et al. “Model Tests for a Floating Wind Turbine on Three Different Floaters”. In: *Journal of Offshore Mechanics and Arctic Engineering* 136.20907 (Mar. 24, 2014). ISSN: 0892-7219. DOI: 10.1115/1.4024711. URL: https://doi.org/10.1115/1.4024711 (visited on 09/14/2024).

[58] J. G. Leishman and T. S. Beddoes. “A Semi-Empirical Model for Dynamic Stall”. In: *Journal of the American Helicopter Society* 34.3 (July 1, 1989), pp. 3–17. DOI: 10.4050/JAHS.34.3.3.

[59] Gauthier Limpens, Huai Yuan Xu, and Hamid Aït Abderrahim. “Six degrees of freedom modelisation of an object in a fluid with OpenFOAM”. In: (June 12, 2015). URL: https://researchportal.sckcen.be/en/publications/six-degrees-of-freedom-modelisation-of-an-object-in-a-fluid-with- (visited on 08/31/2024).

[60] Yuanchuan Liu and Qing Xiao. “Development of a fully coupled aero-hydro-mooring-elastic tool for floating offshore wind turbines”. In: *Journal of Hydrodynamics* 31.1 (Feb. 2019), pp. 21–33. ISSN: 1001-6058, 1878-0342. DOI: 10.1007/s42241-019-0012-6. URL: http://link.springer.com/10.1007/s42241-019-0012-6 (visited on 02/07/2024).

[61] Yuanchuan Liu et al. “Establishing a fully coupled CFD analysis tool for floating offshore wind turbines”. In: *Renewable Energy* 112 (Nov. 1, 2017), pp. 280–301. ISSN: 0960-1481. DOI: 10.1016/j.renene.2017.04.052. URL: https://www.sciencedirect.com/science/article/pii/S0960148117303609 (visited on 02/07/2024).

[62] *Livret sur les effets de l’éolien en mer sur l’environnement*. France Renouvelables. Feb. 5, 2024. URL: https://www.france-renouvelables.fr/etudes-et-publications/livret-sur-les-effets-de-leolien-en-mer-sur-lenvironnement/ (visited on 08/30/2024).

[63] Richard C. Lupton and Robin S. Langley. “Harmonic linearisation of aerodynamic loads in a frequency-domain model of a floating wind turbine”. In: *Wind Energy* 24.8 (2021). _eprint: https://onlinelibrary.wiley.com/doi/pdf/10.1002/we.2605, pp. 833–856. ISSN: 1099-1824. DOI: 10.1002/we.2605. URL: https://onlinelibrary.wiley.com/doi/abs/10.1002/we.2605 (visited on 06/03/2024).

[64] M. Borg and M. Collu. *A comparison between the dynamics of horizontal and vertical axis offshore floating wind turbines | Philosophical Transactions of the Royal Society A: Mathematical, Physical and Engineering Sciences*. URL: https://royalsocietypublishing.org/doi/10.1098/rsta.2014.0076 (visited on 05/21/2024).

[65] Marti, Luisa and Puertas, Rosa. *Sustainable energy development analysis: Energy Trilemma*. URL: https://www.sciencedirect.com/science/article/pii/S2773032822000074 (visited on 05/08/2024).

[66] M. Masciola et al. “Assessment of the importance of mooring dynamics on the global response of the DeepCwind floating semisubmersible offshore wind turbine”. In: Proceedings of the International Offshore and Polar Engineering Conference. ISSN: 1555-1792. 2013, pp. 359–368. ISBN: 978-1-880653-99-9.

[67] Marco Masciola, Jason Jonkman, and Amy Robertson. “Implementation of a Multisegmented, Quasi-Static Cable Model”. In: ().

[68] Pier Francesco Melani et al. “An insight into the capability of the actuator line method to resolve tip vortices”. In: *Wind Energy Science* 9.3 (Mar. 14, 2024). Publisher: Copernicus GmbH, pp. 601–622. ISSN: 2366-7443. DOI: 10.5194/wes-9-601-2024. URL: https://wes.copernicus.org/articles/9/601/2024/ (visited on 08/26/2024).

[69] Nicole Mendoza et al. “Verification and Validation of Model-Scale Turbine Performance and Control Strategies for the IEA Wind 15 MW Reference Wind Turbine”. In: *Energies* 15.20 (Jan. 2022). Number: 20 Publisher: Multidisciplinary Digital Publishing Institute, p. 7649. ISSN: 1996-1073. DOI: 10.3390/en15207649. URL: https://www.mdpi.com/1996-1073/15/20/7649 (visited on 04/11/2024).

[70] Daniel Micallef and Abdolrahim Rezaeiha. “Floating offshore wind turbine aerodynamics: Trends and future challenges”. In: *Renewable and Sustainable Energy Reviews* 152 (Dec. 1, 2021), p. 111696. ISSN: 1364-0321. DOI: 10.1016/j.rser.2021.111696. URL: https://www.sciencedirect.com/science/article/pii/S1364032121009709 (visited on 08/26/2024).

[71] F. Moukalled, L. Mangani, and M. Darwish. *The Finite Volume Method in Computational Fluid Dynamics: An Advanced Introduction with OpenFOAM® and Matlab*. Vol. 113. Fluid Mechanics and Its Applications. Cham: Springer International Publishing, 2016. ISBN: 978-3-319-16873-9 978-3-319-16874-6. DOI: 10.1007/978-3-319-16874-6. URL: https://link.springer.com/10.1007/978-3-319-16874-6 (visited on 05/23/2024).

[72] Lauri Myllyvirta. *Analysis: Clean energy was top driver of China’s economic growth in 2023*. Carbon Brief. Jan. 25, 2024. URL: https://www.carbonbrief.org/analysis-clean-energy-was-top-driver-of-chinas-economic-growth-in-2023/ (visited on 08/30/2024).

[73] J. N. Newman. *Marine Hydrodynamics*. The MIT Press, Aug. 15, 1977. ISBN: 978-0-262-28061-7. DOI: 10.7551/mitpress/4443.001.0001. URL: https://direct.mit.edu/books/book/2693/Marine-Hydrodynamics (visited on 05/21/2024).

[74] *Notes on Computational Fluid Dynamics: General Principles*. CFD Direct. Section: Notes on CFD: General Principles - 5.21 The PIMPLE algorithm. Apr. 11, 2022. URL: https://doc.cfd.direct/notes/cfd-general-principles/the-pimple-algorithm/ (visited on 05/23/2024).

[75] Marielle de Oliveira et al. “CFD INVESTIGATION OF THE IEA OFFSHORE 15 MW REFERENCE WIND TURBINE PERFORMANCE IN FULL SCALE: A TEMPORAL DISCRETIZATION ANALYSIS”. In: *Proceedings of the ASME 2023 42nd International Conference on Ocean, Offshore and Arctic Engineering OMAE2023* ().

[76] Aldert Otter et al. “A review of modelling techniques for floating offshore wind turbines”. In: *Wind Energy* 25.5 (2022). _eprint: https://onlinelibrary.wiley.com/doi/pdf/10.1002/we.2701, pp. 831–857. ISSN: 1099-1824. DOI: 10.1002/we.2701. URL: https://onlinelibrary.wiley.com/doi/abs/10.1002/we.2701 (visited on 02/08/2024).

[77] Johannes Palm et al. “Coupled mooring analysis for floating wave energy converters using CFD: Formulation and validation”. In: *International Journal of Marine Energy* 16 (Dec. 1, 2016), pp. 83–99. ISSN: 2214-1669. DOI: 10.1016/j.ijome.2016.05.003. URL: https://www.sciencedirect.com/science/article/pii/S2214166916300327 (visited on 04/24/2024).

[78] S.V Patankar and D.B Spalding. “A calculation procedure for heat, mass and momentum transfer in three-dimensional parabolic flows”. In: *International Journal of Heat and Mass Transfer* 15.10 (Oct. 1972), pp. 1787–1806. ISSN: 00179310. DOI: 10.1016/0017-9310(72)90054-3. URL: https://linkinghub.elsevier.com/retrieve/pii/0017931072900543 (visited on 05/23/2024).

[79] Antonio Pegalajar-Jurado, Michael Borg, and Henrik Bredmose. “An efficient frequency-domain model for quick load analysis of floating offshore wind turbines”. In: *Wind Energy Science* 3.2 (Oct. 16, 2018). Publisher: Copernicus GmbH, pp. 693–712. ISSN: 2366-7443. DOI: 10.5194/wes-3-693-2018. URL: https://wes.copernicus.org/articles/3/693/2018/ (visited on 06/03/2024).

[80] Antonio Pegalajar-Jurado et al. “Experimental and numerical study of a 10MW TLP wind turbine in waves and wind”. In: *Journal of Physics: Conference Series* 753.9 (Sept. 2016). Publisher: IOP Publishing, p. 092007. ISSN: 1742-6596. DOI: 10.1088/1742-6596/753/9/092007. URL: https://dx.doi.org/10.1088/1742-6596/753/9/092007 (visited on 07/23/2024).

[81] Pere Frontera Pericàs. *CFD Simulation of a Floating Wind Turbine with OpenFOAM: an FSI approach based on the actuator line and relaxation zone methods*. Dec. 2022.

[82] Néstor Ramos-García, Matias Sessarego, and Sergio González Horcas. “Aero-hydro-servo-elastic coupling of a multi-body finite-element solver and a multi-fidelity vortex method”. In: *Wind Energy* 24.5 (2021). _eprint: https://onlinelibrary.wiley.com/doi/pdf/10.1002/we.2584, pp. 481–501. ISSN: 1099-1824. DOI: 10.1002/we.2584. URL: https://onlinelibrary.wiley.com/doi/abs/10.1002/we.2584 (visited on 02/08/2024).

[83] Néstor Ramos-García et al. “Investigation of the floating IEA Wind 15 MW RWT using vortex methods Part I: Flow regimes and wake recovery”. In: *Wind Energy* 25.3 (2022). _eprint: https://onlinelibrary.wiley.com/doi/pdf/10.1002/we.2682, pp. 468–504. ISSN: 1099-1824. DOI: 10.1002/we.2682. URL: https://onlinelibrary.wiley.com/doi/abs/10.1002/we.2682 (visited on 02/08/2024).

[84] Néstor Ramos-García et al. “Investigation of the floating IEA wind 15-MW RWT using vortex methods Part II: Wake impact on downstream turbines under turbulent inflow”. In: *Wind Energy* 25.8 (2022). _eprint: https://onlinelibrary.wiley.com/doi/pdf/10.1002/we.2738, pp. 1434–1463. ISSN: 1099-1824. DOI: 10.1002/we.2738. URL: https://onlinelibrary.wiley.com/doi/abs/10.1002/we.2738 (visited on 08/21/2024).

[85] R Ramponi, R Amaral, and A Viré. “Investigation of the effect of prescribed coupled motions on the power production of a floating offshore wind turbine”. In: *Journal of Physics: Conference Series* 2626.1 (Oct. 1, 2023), p. 012029. ISSN: 1742-6588, 1742-6596. DOI: 10.1088/1742-6596/2626/1/012029. URL: https://iopscience.iop.org/article/10.1088/1742-6596/2626/1/012029 (visited on 02/26/2024).

[86] *RANS-based turbulence models – CFD-Wiki, the free CFD reference*. URL: https://www.cfd-online.com/Wiki/RANS-based_turbulence_models (visited on 05/23/2024).

[87] E. Ransley et al. *Hydrodynamic response of a floating offshore wind turbine (1st FOWT Comparative Study Dataset)*. Accepted: 2023-01-09T15:53:46Z. Oct. 1, 2022. DOI: 10.24382/5034. URL: https://pearl.plymouth.ac.uk/handle/10026.1/20151 (visited on 04/11/2024).

[88] Yajun Ren, Vengatesan Venugopal, and Wei Shi. “Dynamic analysis of a multi-column TLP floating offshore wind turbine with tendon failure scenarios”. In: *Ocean Engineering* 245 (Feb. 1, 2022), p. 110472. ISSN: 0029-8018. DOI: 10.1016/j.oceaneng.2021.110472. URL: https://www.sciencedirect.com/science/article/pii/S0029801821017534 (visited on 05/22/2024).

[89] Manuel Rentschler et al. “CFD code comparison, verification and validation for decay tests of a FOWT semi-submersible floater”. In: *Journal of Ocean Engineering and Marine Energy* 9.2 (May 1, 2023), pp. 233–254. ISSN: 2198-6452. DOI: 10.1007/s40722-022-00260-z. URL: https://doi.org/10.1007/s40722-022-00260-z (visited on 05/31/2024).

[90] Pierre-Elouan Mikael Réthoré. *Wind Turbine Wake in Atmospheric Turbulence*. Risø-PhD. Roskilde: Risø National Laboratory for Sustainable Energy, Oct. 2009. ISBN: 978-87-550-3785-4.

[91] A. N. Robertson et al. “OC6 Phase I: Investigating the underprediction of low-frequency hydrodynamic loads and responses of a floating wind turbine”. In: *Journal of Physics: Conference Series* 1618.3 (Sept. 2020). Publisher: IOP Publishing, p. 032033. ISSN: 1742-6596. DOI: 10.1088/1742-6596/1618/3/032033. URL: https://dx.doi.org/10.1088/1742-6596/1618/3/032033 (visited on 06/03/2024).

[92] Amy Robertson et al. “Offshore Code Comparison Collaboration Continuation Within IEA Wind Task 30: Phase II Results Regarding a Floating Semisubmersible Wind System”. In: ASME 2014 33rd International Conference on Ocean, Offshore and Arctic Engineering. American Society of Mechanical Engineers Digital Collection, Oct. 1, 2014. DOI: 10.1115/OMAE2014-24040. URL: https://dx.doi.org/10.1115/OMAE2014-24040 (visited on 06/03/2024).

[93] Amy N. Robertson et al. “OC5 Project Phase II: Validation of Global Loads of the DeepCwind Floating Semisubmersible Wind Turbine”. In: *Energy Procedia*. 14th Deep Sea Offshore Wind R&D Conference, EERA DeepWind’2017 137 (Oct. 1, 2017), pp. 38–57. ISSN: 1876-6102. DOI: 10.1016/j.egypro.2017.10.333. URL: https://www.sciencedirect.com/science/article/pii/S1876610217352931 (visited on 06/03/2024).

[94] Wolfgang Rodi. “DNS and LES of some engineering flows”. In: *Fluid Dynamics Research* 38.2 (Feb. 28, 2006). Publisher: IOP Publishing, p. 145. ISSN: 1873-7005. DOI: 10.1016/j.fluiddyn.2004.11.003. URL: https://iopscience.iop.org/article/10.1016/j.fluiddyn.2004.11.003/meta (visited on 05/23/2024).

[95] Romain Pinguet. *Hydrodynamics of semi-submersible floater for offshore wind turbines in highly nonlinear waves using Computational Fluid Dynamics (CFD), and validation of overset meshing technique in a numerical wave tank*.

[96] Ideen Sadrehaghighi. “Dynamic & Adaptive Meshing”. In: *CFD Open Series* (Jan. 1, 2021). URL: https://www.academia.edu/44183574/Dynamic_and_Adaptive_Meshing (visited on 08/31/2024).

[97] Gilberto Santo et al. “Effect of rotor–tower interaction, tilt angle, and yaw misalignment on the aeroelasticity of a large horizontal axis wind turbine with composite blades”. In: *Wind Energy* 23.7 (2020). _eprint: https://onlinelibrary.wiley.com/doi/pdf/10.1002/we.2501, pp. 1578–1595. ISSN: 1099-1824. DOI: 10.1002/we.2501. URL: https://onlinelibrary.wiley.com/doi/abs/10.1002/we.2501 (visited on 09/05/2024).

[98] Luca Scarlatti. *Computational Fluid Dynamics of a Floating Offshore Wind Turbine using OpenFOAM*. Tu Delft, Oct. 2023.

[99] T. Sebastian and M. A. Lackner. “Development of a free vortex wake method code for offshore floating wind turbines”. In: *Renewable Energy* 46 (Oct. 1, 2012), pp. 269–275. ISSN: 0960-1481. DOI: 10.1016/j.renene.2012.03.033. URL: https://www.sciencedirect.com/science/article/pii/S0960148112002315 (visited on 08/30/2024).

[100] *September 2023 » Yale Climate Connections*. Yale Climate Connections. Sept. 29, 2023. URL: http://yaleclimateconnections.org/2023/09/ (visited on 05/27/2024).

[101] Mohd Atif Siddiqui et al. “Comparing the Utility of Coupled Aero-Hydrodynamic Analysis Using a CFD Solver versus a Potential Flow Solver for Floating Offshore Wind Turbines”. In: *Energies* 16.23 (Jan. 2023). Number: 23 Publisher: Multidisciplinary Digital Publishing Institute, p. 7833. ISSN: 1996-1073. DOI: 10.3390/en16237833. URL: https://www.mdpi.com/1996-1073/16/23/7833 (visited on 02/26/2024).

[102] Jens Nørkær Sørensen and Wen Zhong Shen. “Numerical Modeling of Wind Turbine Wakes”. In: *Journal of Fluids Engineering* 124.2 (May 28, 2002), pp. 393–399. ISSN: 0098-2202. DOI: 10.1115/1.1471361. URL: https://doi.org/10.1115/1.1471361 (visited on 08/30/2024).

[103] Nikos Spyropoulos et al. “Investigating the Level of Fidelity of an Actuator Line Model in Predicting Loads and Deflections of Rotating Blades under Uniform Free-Stream Flow”. In: *Applied Sciences* 11.24 (Jan. 2021). Number: 24 Publisher: Multidisciplinary Digital Publishing Institute, p. 12097. ISSN: 2076-3417. DOI: 10.3390/app112412097. URL: https://www.mdpi.com/2076-3417/11/24/12097 (visited on 08/26/2024).

[104] Ronith Stanly et al. “Large-Eddy Simulation of a wind turbine using a Filtered Actuator Line Model”. In: *Journal of Wind Engineering and Industrial Aerodynamics* 222 (Mar. 1, 2022), p. 104868. ISSN: 0167-6105. DOI: 10.1016/j.jweia.2021.104868. URL: https://www.sciencedirect.com/science/article/pii/S016761052100341X (visited on 08/31/2024).

[105] Federico Taruffi, Felipe Novais, and Axelle Viré. “An experimental study on the aerodynamic loads of a floating offshore wind turbine under imposed motions”. In: *Wind Energy Science* 9.2 (Feb. 13, 2024). Publisher: Copernicus GmbH, pp. 343–358. ISSN: 2366-7443. DOI: 10.5194/wes-9-343-2024. URL: https://wes.copernicus.org/articles/9/343/2024/ (visited on 02/22/2024).

[106] *The Green Deal Industrial Plan - European Commission*. URL: https://commission.europa.eu/strategy-and-policy/priorities-2019-2024/european-green-deal/green-deal-industrial-plan_en (visited on 08/30/2024).

[107] Thanh Toan Tran and Dong-Hyun Kim. “A CFD study of coupled aerodynamic-hydrodynamic loads on a semisubmersible floating offshore wind turbine”. In: *Wind Energy* 21.1 (2018). _eprint: https://onlinelibrary.wiley.com/doi/pdf/10.1002/we.2145, pp. 70–85. ISSN: 1099-1824. DOI: 10.1002/we.2145. URL: https://onlinelibrary.wiley.com/doi/abs/10.1002/we.2145 (visited on 02/07/2024).

[108] Francois Trigaux, Philippe Chatelain, and Grégoire Winckelmans. “Investigation of blade flexibility effects on the loads and wake of a 15 MW wind turbine using a flexible actuator line method”. In: *Wind Energy Science* 9.8 (Aug. 22, 2024). Publisher: Copernicus GmbH, pp. 1765–1789. ISSN: 2366-7443. DOI: 10.5194/wes-9-1765-2024. URL: https://wes.copernicus.org/articles/9/1765/2024/ (visited on 08/27/2024).

[109] Francois Trigaux, Philippe Chatelain, and Grégoire Winckelmans. “Investigation of blade flexibility effects on the loads and wake of a 15 MW wind turbine using a flexible actuator line method”. In: *Wind Energy Science* 9.8 (Aug. 22, 2024). Publisher: Copernicus GmbH, pp. 1765–1789. ISSN: 2366-7443. DOI: 10.5194/wes-9-1765-2024. URL: https://wes.copernicus.org/articles/9/1765/2024/ (visited on 08/27/2024).

[110] United Nations Environment Programme. *Emissions Gap Report 2023: Broken Record – Temperatures hit new highs, yet world fails to cut emissions (again)*. United Nations Environment Programme, Nov. 2023. ISBN: 978-92-807-4098-1. DOI: 10.59117/20.500.11822/43922. URL: https://wedocs.unep.org/20.500.11822/43922 (visited on 10/02/2024).

[111] Decheng Wan et al. “Floating Offshore Wind Farm Projects in China: Part I Coupled Aero-Hydro-Elastic Behaviors”. In: The 34th International Ocean and Polar Engineering Conference. OnePetro, June 16, 2024. URL: https://dx.doi.org/ (visited on 08/21/2024).

[112] Kai Wang et al. “Aerodynamic performance analysis of a floating wind turbine with coupled blade rotation and surge motion”. In: *Engineering Applications of Computational Fluid Mechanics* 18.1 (Dec. 31, 2024). Publisher: Taylor & Francis _eprint: https://doi.org/10.1080/19942060.2023.2301524, p. 2301524. ISSN: 1994-2060. DOI: 10.1080/19942060.2023.2301524. URL: https://doi.org/10.1080/19942060.2023.2301524 (visited on 08/30/2024).

[113] L. Wang et al. “Experimental Validation of Models of a Hull-Based Tuned Mass Damper System for a Semisubmersible Floating Offshore Wind Turbine Platform”. In: *Journal of Physics: Conference Series* 2626.1 (Oct. 2023). Publisher: IOP Publishing, p. 012067. ISSN: 1742-6596. DOI: 10.1088/1742-6596/2626/1/012067. URL: https://dx.doi.org/10.1088/1742-6596/2626/1/012067 (visited on 09/14/2024).

[114] Lu Wang et al. “OC6 phase I: Improvements to the OpenFAST predictions of nonlinear, low-frequency responses of a floating offshore wind turbine platform”. In: *Renewable Energy* 187 (Mar. 1, 2022), pp. 282–301. ISSN: 0960-1481. DOI: 10.1016/j.renene.2022.01.053. URL: https://www.sciencedirect.com/science/article/pii/S0960148122000635 (visited on 06/03/2024).

[115] Lu Wang et al. “OC6 Phase Ia: CFD Simulations of the Free-Decay Motion of the DeepCwind Semisubmersible”. In: *Energies* 15.1 (Jan. 2022). Number: 1 Publisher: Multidisciplinary Digital Publishing Institute, p. 389. ISSN: 1996-1073. DOI: 10.3390/en15010389. URL: https://www.mdpi.com/1996-1073/15/1/389 (visited on 07/13/2024).

[116] Lu Wang et al. “OC6 Phase Ib: Validation of the CFD predictions of difference-frequency wave excitation on a FOWT semisubmersible”. In: *Ocean Engineering* 241 (Dec. 1, 2021), p. 110026. ISSN: 0029-8018. DOI: 10.1016/j.oceaneng.2021.110026. URL: https://www.sciencedirect.com/science/article/pii/S0029801821013603 (visited on 09/18/2024).

[117] Qiang Wang, Hu Zhou, and Decheng Wan. “Numerical simulation of wind turbine blade-tower interaction”. In: *Journal of Marine Science and Application* 11.3 (Sept. 1, 2012), pp. 321–327. ISSN: 1993-5048. DOI: 10.1007/s11804-012-1139-9. URL: https://doi.org/10.1007/s11804-012-1139-9 (visited on 09/05/2024).

[118] Wiatros-Motyka, Małgorzata, Fulghum, Nicolas, and Jones, Dave. *Global Electricity review 2024*. EMBER, 2024.

[119] Chih-Hua Keni Wu and Vinh-Tan Nguyen. “Aerodynamic simulations of offshore floating wind turbine in platform-induced pitching motion”. In: *Wind Energy* 20.5 (2017), pp. 835–858. ISSN: 1099-1824. DOI: 10.1002/we.2066. URL: https://onlinelibrary.wiley.com/doi/abs/10.1002/we.2066 (visited on 02/22/2024).

[120] Shun Xu et al. “A Review of High-Fidelity Computational Fluid Dynamics for Floating Offshore Wind Turbines”. In: *Journal of Marine Science and Engineering* 10.10 (Oct. 2022). Number: 10 Publisher: Multidisciplinary Digital Publishing Institute, p. 1357. ISSN: 2077-1312. DOI: 10.3390/jmse10101357. URL: https://www.mdpi.com/2077-1312/10/10/1357 (visited on 02/06/2024).

[121] YiQin Xu and Yulia T. Peet. “Verification and convergence study of a spectral-element numerical methodology for fluid-structure interaction”. In: *Journal of Computational Physics: X* 10 (Mar. 1, 2021), p. 100084. ISSN: 2590-0552. DOI: 10.1016/j.jcpx.2021.100084. URL: https://www.sciencedirect.com/science/article/pii/S2590055221000019 (visited on 02/25/2024).

[122] Yingjie Xue et al. “Numerical Study on the Hydrodynamic Response of Y-Shaped Floating Offshore Wind Turbine Platform”. In: ().

[123] Xiaolei Yang and Fotis Sotiropoulos. “A Review on the Meandering of Wind Turbine Wakes”. In: *Energies* 12.24 (Jan. 2019). Number: 24 Publisher: Multidisciplinary Digital Publishing Institute, p. 4725. ISSN: 1996-1073. DOI: 10.3390/en12244725. URL: https://www.mdpi.com/1996-1073/12/24/4725 (visited on 09/01/2024).

[124] Mao-kun Ye et al. “CFD simulations targeting the performance of the NTNU BT1 wind turbine using overset grids”. In: *JOURNAL OF HYDRODYNAMICS* (Nov. 16, 2023). Num Pages: 9 Place: New York Publisher: Springer Web of Science ID: WOS:001106460800003. ISSN: 1001-6058, 1878-0342. DOI: 10.1007/s42241-023-0065-4. URL: https://www.webofscience.com/api/gateway?GWVersion=2&SrcAuth=DOISource&SrcApp=WOS&KeyAID=10.1007%2Fs42241-023-0065-4&DestApp=DOI&SrcAppSID=EUW1ED0D39XtFszfQHjg3ahvrL0DP&SrcJTitle=JOURNAL+OF+HYDRODYNAMICS&DestDOIRegistrantName=Springer-Verlag (visited on 02/22/2024).

[125] Yin Zhang and Bumsuk Kim. “A Fully Coupled Computational Fluid Dynamics Method for Analysis of Semi-Submersible Floating Offshore Wind Turbines Under Wind-Wave Excitation Conditions Based on OC5 Data”. In: *Applied Sciences* 8.11 (Nov. 2018). Number: 11 Publisher: Multidisciplinary Digital Publishing Institute, p. 2314. ISSN: 2076-3417. DOI: 10.3390/app8112314. URL: https://www.mdpi.com/2076-3417/8/11/2314 (visited on 06/03/2024).

[126] Wenjie Zhong et al. “Comparison study on mooring line models for hydrodynamic performances of floating offshore wind turbines”. In: *Ocean Engineering* 296 (Mar. 15, 2024), p. 117083. ISSN: 0029-8018. DOI: 10.1016/j.oceaneng.2024.117083. URL: https://www.sciencedirect.com/science/article/pii/S0029801824004207 (visited on 05/22/2024).

[127] Yang Zhou et al. “Numerical Modelling of Dynamic Responses of a Floating Offshore Wind Turbine Subject to Focused Waves”. In: *Energies* 12.18 (Jan. 2019). Number: 18 Publisher: Multidisciplinary Digital Publishing Institute, p. 3482. ISSN: 1996-1073. DOI: 10.3390/en12183482. URL: https://www.mdpi.com/1996-1073/12/18/3482 (visited on 02/07/2024).